Terahertz Imaging using a Quantum Dot Detector

by

Stephen Pelling

Department of Physics

Royal Holloway University of London

This thesis is submitted for the degree of

Doctor of Philosophy

August 2011

I, Stephen Pelling confirm that the work presented in this thesis is my own. Where information has been derived from other sources, I confirm that this has been indicated in the thesis.

Signature:.....

Date:.....

Abstract

This thesis covers research into the development and use of Quantum dot based THz detectors for imaging. The area of THz imaging has been of great interest to research in recent years due to its advancements in the security screening and medical screening fields. The aim of this research is to provide a spectral sensitivity to the imaging techniques. This will allow for a greater wealth of applications.

The detector is described in detail by breaking it up into its constituent parts and a brief description of the THz emitters is given. A cryogen free refrigerator was used to take measurements to provide a step towards real world applications by potentially reducing running costs. We study a number of designs of the imager, including different filters in order to improve system performance.

QD-SET and QD-PC detectors were characterised. The QD-PC detector concedes in sensitivity to the QD-SET, but it has reduced fabrication and operation demands. An optical system was constructed and optimised for imaging. It was used to take images of leaves using a variety of sensors and setups, obtaining resolutions of $\sim 1.8\,\mathrm{mm}$. These demonstrated potential for this technology in THz imaging applications.

Acknowledgements

I would like to thank Vladimir Antonov for his guidance and the opportunity to study for my PhD at RHUL, I would also like to thank Spas Spasov and Rais Shaikhaidarov, for their advice and verification on many things. Massimo Venti for building many of my designs when altering the fridge.

I would like to thank my parents for helping me and supporting me my whole life, and thanks to my sister Michelle Pelling for her much needed proof reading skills.

For inspiring me to do Physics I would also like to mention Mr. Hows, who managed to make everything seem easy and exciting to learn.

My friends have also been a great help within the department, helping me answer many questions and picking which picture or graph looks best, to mention a few Richard Marsh, Chris Checkley, Simon Schmidlin and David Pavitt. And finally thanks must go to Aya Shibahara for giving me constant motivation and help throughout my PhD.

Contents

List of Figures

List of Tables

Chapter 1

Introduction

1.1 Motivation

The development of a sensitive Terahertz (THz) single photon detector opens up the possibilities for a vast variety of applications such as deep space observation, health screening, security surveillance and spectral chemical analysis. Terahertz radiation is a relatively unexplored region of the electromagnetic spectrum compared to other regions such as microwave, visible and even infrared. The development of THz components, like generators and detectors, is currently in an active phase. In this current work we concentrate on the study of THz detectors and THz imaging.

The Terahertz (THz) spectrum, sometimes referred to as far-infrared, is situated on the far end of the infrared band, and is sandwiched between this and the microwave band. Its frequency range is often stated as lying between 300 GHz and 3 THz which corresponds to a sub-millimetre wavelength of between 1 mm and 100 μm (see Figure 1.1).

THz is a non-ionising radiation which can penetrate a variety of non-conducting materials such as paper, wood, masonry and plastic. However it is heavily suppressed by metal or water. A combination of these properties, and the fact that

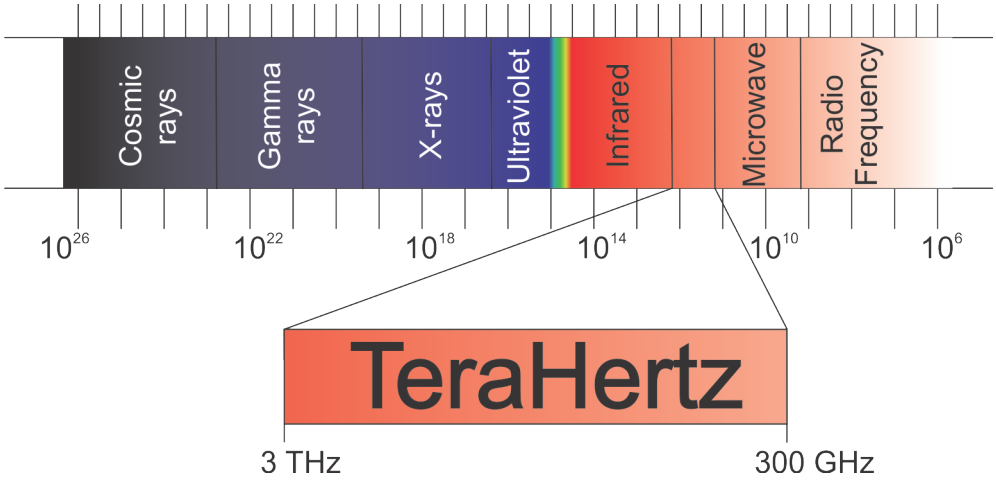

Figure 1.1: Electromagnetic spectrum showing the Terahertz region.

different materials have unique characteristics of THz emmision, enables the use of the THz range for security applications. Another possible application is health screening. Sub-millimetre wavelengths interact with the molecules of the substance under investigation, returning a specific absorption spectrum, which can then be matched to data to identify the substance [5][6].

At certain frequencies, THz photons are able to penetrate several centimetres of skin, therefore, it is soon expected to be used to scan for types of epithelial cancer (skin cancer), and as a safer method for the detection of breast cancer. It is hoped that one day this technique could replace the mammogram. One of the leaders in this field is Xi-Cheng Zhang [7–11], who is currently working in collaboration with doctors at Boston Medical Centre exploring ways to use THz to detect breast cancer. He also is working together with the Australia Biomedical Engineering Centre to study THz imaging of bone marrow cancer samples. Taking breast cancer as an example, the THz scan could image an abnormality in the tissue and using spectrographic techniques determine whether it is cancerous, because cancerous tissue tends to have higher water content than healthy tissue [12].

In security applications, a Terahertz 'camera' can use the ability of non-ionising semi-penetrating scans for the scanning and subsequent detection of

concealed metallic objects such as knives and guns. Furthermore, spectroscopy of materials using Terahertz provides unique signatures for many different substances, which could be used to detect concealed explosives, as well as drugs, as seen in Figure 1.2. It is even believed that this technique could detect bacterial spores similar to anthrax, aiding the detection of biologically harzardous substances [13].

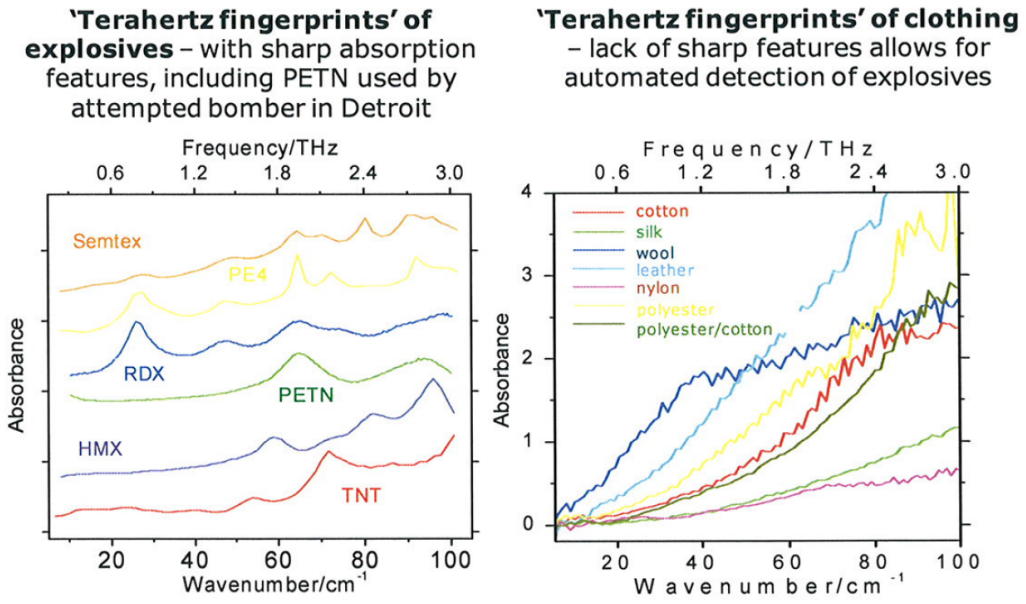

Figure 1.2: THz spectra of explosives and different clothing materials [1].

The Terahertz gap lies between the effective technologies for optical communication, which is centred at infrared, and radio communication. At present, little research has been conducted in this area to see if there is the possibility of bridging this gap, which could potentially give a high quality of infrared communication without the need for direct line of sight, as radiation in the THz gap has the ability to pass through certain materials. Some research on this is taking place at the School of Electrical and Electronic Engineering at the University of Adelaide in Australia [14]. Finally I would like to mention a traditional application, such as deep space observation in the THz range, which is useful for the study of cold dust clouds in the universe.

1.2 Terahertz Detection

The detection and measurement of THz radiation is intrinsically difficult because of the low energy of terahertz photons, ~ 5 meV. The detection of individual photons in these frequencies is a challenging task, unlike with visible and near infrared light, ~ 1 eV, which with the aid of photomultipliers are able to achieve single photon detection. A few issues have to be addressed in order to make single photon detection in the terahertz range possible and useful. A detector should be very sensitive to be able to resolve the absorption of individual photons of small energies ~ 5 meV, and at the same time it should be fast enough to record a large number of such events, $\sim 10^6$ s^{-1}. There are currently several types of detectors under study: different types of bolometers, plasmon based devices and quantum dot based detectors.

1.2.1 The Bolometer

One of the simplest and earliest methods of measuring electromagnetic radiation was the bolometer, which was invented by Samuel Pierpont Langley in 1878 and forms of the bolometer are still in use for a variety of applications today. Langley's bolometer consisted of two platinum strips coated in a carbon residue known as lampblack, which is essentially soot (a dark powdery deposit of unburned fuel residues). It is generally formed experimentally by passing a non-combustible surface, such as glass, through an open flame producing a dark unreflective surface. It was constructed so that the two strips formed a Wheatstone bridge [15]. The whole assembly is then covered and insulated only leaving one strip exposed. Due to the covering of lampblack it is very efficient at absorbing incident radiation and this causes the exposed strip to heat up, thus increasing the resistance, which is detected by the Wheatstone bridge [16].

The achievements of Langley's bolometer were remarkable; it was even reported that, "Langley's bolometer was so sensitive that it could detect thermal radiation from a cow a quarter of a mile away" [17], although this was only true for a small mid-infrared range of frequencies. Variations of Langley's bolometer are still used today in measuring the heat of distant objects, such as in the field of astronomy for measuring the heat of stars [18]. However, it was not until Frank Low developed the germanium bolometer in 1961 that the detection of far infrared wavelengths became of great interest. The invention of Low's bolometer was the next leap in THz and infrared detection since this bolometer had a sensitivity that was hundreds of times greater than its predecessors [19], and was the start of the semiconductor bolometer [20–22].

1.2.1.1 The Semiconductor Bolometer

In 1961 Frank James Low, a solid-state physicist, invented the gallium-doped germanium bolometer. This new detector allowed the extension of observations to much longer wavelengths than previously possible. Low, then accompanied by Carl Gillespie, extended his observations into the far infrared, using a helium-cooled germanium bolometer [23].

The Richards bolometer, which is an In-doped germanium bolometer, has a noise equivalent power (NEP) of 9×10^{-13} W/Hz$^{1/2}$, while the Drew and Sievers bolometer, which contains an In and Sb impurity, has a NEP of $\sim 3 \times 10^{-14}$ W/Hz$^{1/2}$. The NEP is defined as the minimum detectable power per square root bandwidth. The NEP is essentially a measurement of the signal to noise ratio expected in the measurement of a detector, and principally is equivalent to its predicted sensitivity [24]. Improvements on the germanium bolometers may be possible depending on the choice of doping agent [25].

1.2.1.2 The Superconducting Bolometer

The superconducting bolometer was a leap in submillimetre wavelength detection. These detectors need low temperatures for operation determined by the transition temperature of the superconducting material used. The superconducting energy gap, 2Δ, is two or three orders of magnitude lower than in semiconducting materials. Therefore, a flood of electron charge, two to three times larger than in a semiconductor, is created during photon absorption of the same photon energy. This would permit for a greater scope of detectable photons with significantly lower energies, as long as $\hbar\omega \gg 2\Delta$ [26].

The basic superconducting bolometer uses the same principle as Langley's bolometer by being a direct measurement of the change in resistance. The principle is based on having a superconducting wire, or micro bridge, connected to two normal conducting 'heat sinks' over which resistance is measured. While the wire is superconducting, the resistance of the wire is in theory zero but will be measured as extremely small because of the resistance of the connectors. However, when a photon is incident on the wire, it heats it above the critical temperature of the superconducting film. This will cause the superconductivity to be destroyed in the region of the wire, which creates a small area of normal conducting material. This will of course increase the resistivity of the wire and the resistance will be dependent on the number of photons incident upon it; as can be imagined, sensitivity of measurement is an issue [27].

The first type of superconducting bolometer is the voltage-biased mode bolometer, which refers to the way in which the resistance is measured. In this type the wire is biased with a constant voltage and the resistance is calculated using the measured current. Another type is the current-biased mode bolometer. As the name suggests, this is biased with a constant current and the resistance is calculated by measuring the potential difference. The current-biased mode has the advantage that a voltage can be amplified relatively easily. Bolometer single

photon detection systems have been developed based on the first X-ray detector, which used a normal metal film as an absorber and a normal metal-insulator-superconductor (NIS) tunnel junction built by Nahum et al. [28–30]. In this type of detector, when a photon is incident upon the detector it creates a 'hot-spot' on the normal metal, which is dispersed into the whole absorber and the increase in electron temperature is measured by the NIS tunnel junctions.

The extension of this method to the detection of a photon with a longer wavelength, was suggested in the paper by Semenov et al. [26]. This paper discusses the supercurrent-assisted mechanism for hot-spot formation, in which the absorption of a photon with energy $\hbar\omega \gg 2\Delta$ creates, through electron-electron and electron-Debye-phonon interactions, a local non-equilibrium perturbation with a large number of excited hot electrons. This raises the temperature of the average electron above the superconducting critical temperature T_C, which creates a local non-superconducting region of the thermalisation length $2\lambda_T$, see Figure 1.3 a). The size of this hot-spot begins to grow after this initial thermalisation (Figure 1.3 b)) as hot electrons begin to diffuse out of its centre. At this instant, the supercurrent is deflected as it is expelled from the hot-spot volume and is concentrated in the outer region between the hot-spot and the edges of the film (Figure 1.3 c)). If the bias current I_{bias} is sufficient to exceed the critical current in the outer region, the phase slip centres are sprung [31] and a non-superconducting barrier is formed across the entire width 'w' of the device (Figure 1.3 d)), giving rise to a voltage signal, as a result of the collaborative effect of the bias current and the radiation quantum.

After the hot-spot creation the hot electrons need to cool so that the cycle is completed. The cooling process involves the electrons diffusing out of the hot-spot losing energy via electron-phonon scattering. After a time period, depending on both the diffusion rate and the quasiparticle relaxation dynamics [32], the superconducting path is restored along the wire. For the NbN device studied by

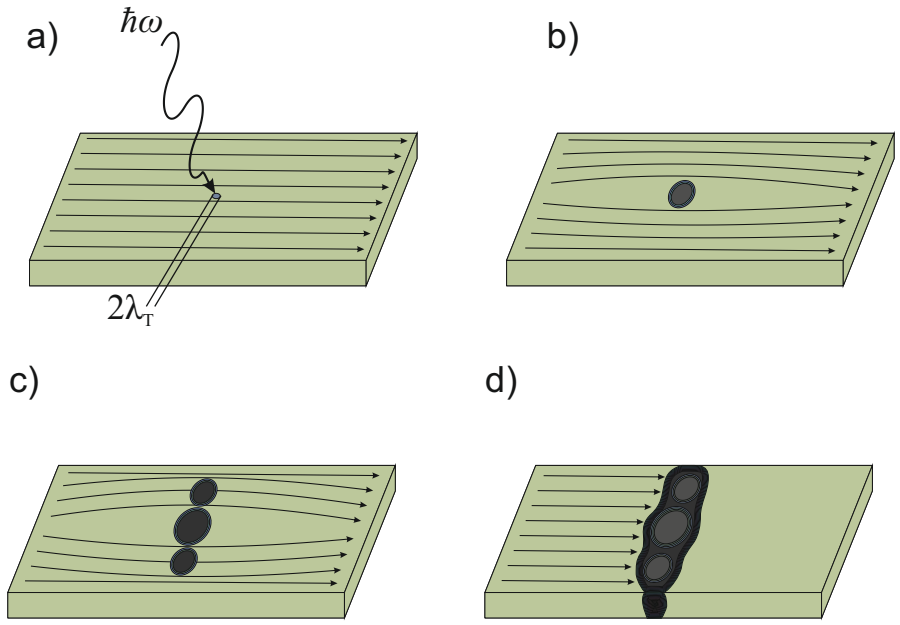

Figure 1.3: Schematics of the supercurrent-assisted hot-spot formation mechanism in an ultrathin and narrow superconducting strip, kept at a temperature far below T_c. The arrows indicate the direction of the supercurrent flow.

Semenov et al. [26], a temporary switching between the superconducting and resistive states, because of this hot-spot creation and relaxation process, was measured with a time scale of ~ 30 ps.

1.2.1.3 The Hot Electron Bolometer

The hot electron bolometer is based on the temperature dependence of the resistance of a superconducting micro bridge close to the transition temperature [33], so that the hot-spot can be created from a low energy photon. The construction of arrays of superconducting bolometers allows an averaging of signals and provides the opportunity for imaging [34]. With the arrival of SQUIDs (Superconducting Quantum Interference Devices) an adequate amplification and detection system for this current signal has become possible [35]. A SQUID is an extremely sensitive magnetometer, which can detect extremely small changes in the current across the micro bridge [36]. A disadvantage of the superconducting bolometer

SQUID system is that, because of its sensitivity, it is difficult to use as it requires significant shielding of external noise [37]. The next step in the development of such a technique, is with the construction of an array of superconducting bolometers using SQUIDs as a read-out method [38].

1.2.2 The Quantum Dot Detector

Although superconducting bolometers have improved significantly since Langley's original bolometer with the ability of single photon detection, a new method was proposed, which unlike the previous bolometers discussed here, was not an extension of Langley's work. The use of quantum dots was suggested as a completely new method in detection of THz radiation, which is explored in this thesis.

A quantum dot (QD) is essentially a region classified with having zero dimensions; this is not to say that it does not have physical dimensions, having typical dimensions in the order of 100-1000 nm. In fact, this means that they are made out of millions of atoms with the equivalent number of electrons. Almost all the electrons are tightly bound to the nuclei of the material, however in most QDs there are typically between one and a few hundred free electrons. The interesting part is that the deBroglie wavelength of these electrons can be comparable to the size of the dot, causing these electrons to occupy discrete quantum energy levels, much like the atomic orbitals in atoms. As a result of this they also display a discrete excitation spectrum. The analogies between QDs and atoms often warrant them to be referred to as artificial atoms [39]. However, for the relatively large size of the QDs required for THz detectors, the spatial quantisation of energy levels is small compared to temperature broadening.

A literature review of the development of this QD based technique is given in Section 2.7 after the reader is introduced to a more detailed explanation of the physics, which is provided in Section 2.5.

Chapter 2

Detector Theory

In this chapter the THz detectors with which we study will be described. First a brief overview of the quantum dot detector is given, followed by a description of its component parts and the relevant theory required for the understanding of their function in the detector. In particular, a detailed explanation of the SET is given in Section 2.6, ending with a review of the development of the QD detector and a brief summary of the operation of the device.

2.1 The QD Detector

The left image of Figure 2.1 shows a schematic for the two types of QD detectors investigated in this thesis. One consists of a QD coupled to a single electron transistor (SET), referred to as the QD-SET detector and the other is a QD coupled to a point contact (PC) and is called the QD-PC detector. Both the SET and PC are capacitively coupled to the QD. They are used to probe the charge excitation of the QD caused by the absorption of THz photons. The absorption of the THz photons occurs through the stimulation of plasma waves. The plasma waves then decay into single electron excitations, which are detected by either the SET or the PC. The advantage of this device is high spectral resolution resulting from resonance excitation of the plasma oscillations in the QD.

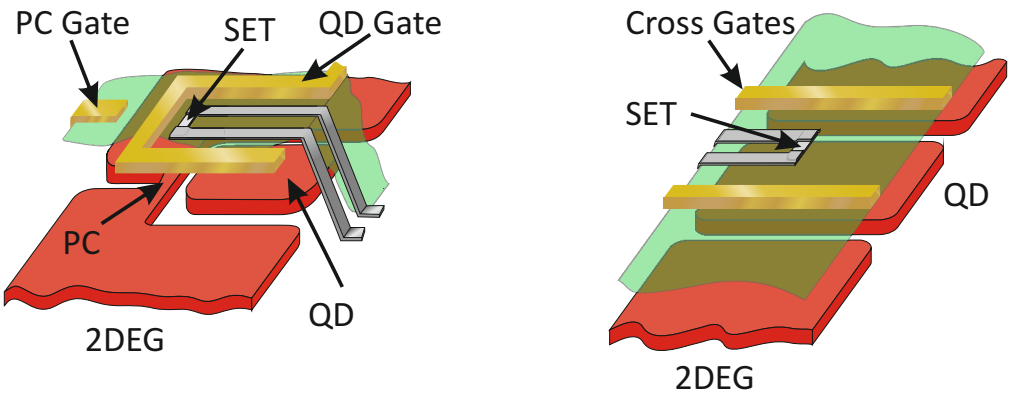

Figure 2.1: Schematic of devices; Left: QD-PC-SET device. Right: Cross gate QD-SET device. The gates are shown in gold, the 2DEG is shown in red.

There are a number of parameters that characterise the device. The primary parameters are the capacitances that couple the different elements in the system (see Figure 2.2) as well as the voltages which are used to bring the device to its operation point. The other important parameters are probabilty of photon absorption, efficiency of conversion of the plasma wave to single particle excitation and broadening of the plasma resonance spectral line.

Two designs of terahertz detectors were fabricated. A simplified circuit of the first design is shown in Figure 2.2 (top). This device can either be QD-SET or QD-PC depending on the read-out element. The QD in these devices is formed by a single QD gate. The design of the second type, a cross gate QD-SET, has two cross gates forming the QD, see Figure 2.2 (bottom). This device is shown schematically in Figure 2.1. This device lacks a point contact for readout but provides greater manipulation of the dot as both gates are adjustable.

In order to understand the operation of these terahertz detectors, the following sections describe the component parts in detail.

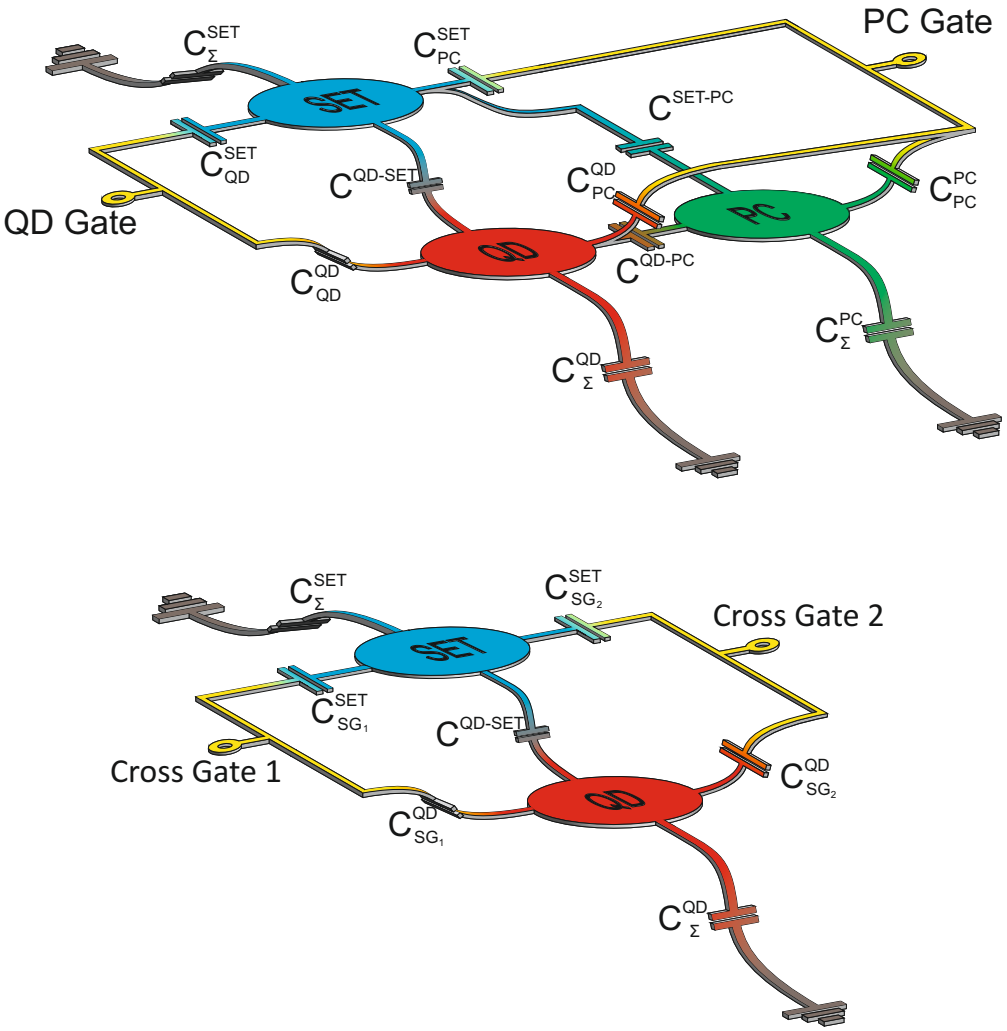

Figure 2.2: Top: Capacitive coupling between the different elements of the device, for the QD-PC-SET device; Bottom: Capacitive coupling between the different elements of the device, for the cross gate QD-SET device.

2.2 Two Dimensional Electron Gas

The two dimensional electron gas (2DEG) is formed at the interface between the two semiconductors GaAs and AlGaAs. As its name suggests, the 2DEG can be considered as a two dimensional conductive sheet of delocalised electrons (an electron gas) in which the electrons have high mobility in the x-y plane but are restricted in the z-direction.

It is fabricated using the process of molecular beam epitaxy (MBE). The basic MBE process consists of 'molecular beams' of semiconductor elements being deposited onto a heated crystalline substrate in order to form thin epitaxial layers. The molecular beams are produced by thermal effusion cells, see Figure 2.3. For growing the wafers used in this thesis, one cell would contain aluminium, one gallium, and the other arsenic.

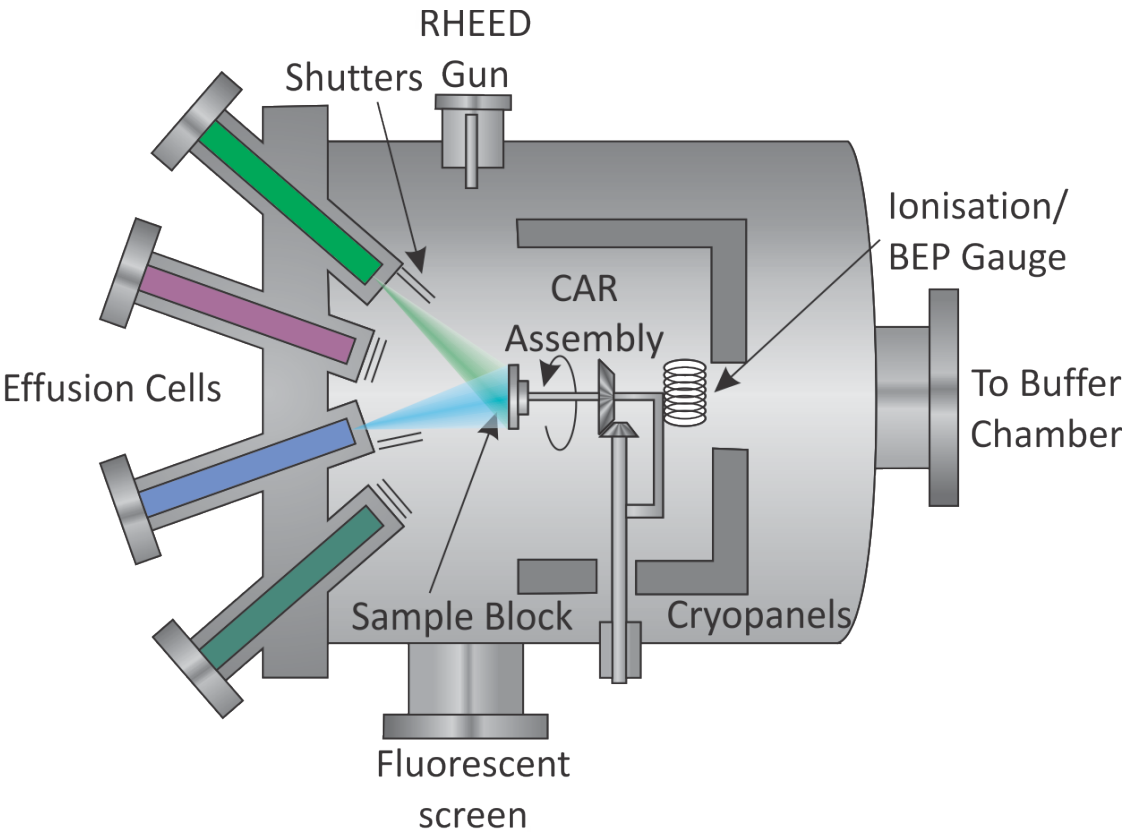

Figure 2.3: Schematic of MBE [2].

To create layers using MBE, a substrate is placed on the sample holder and it is rotated in order to ensure even distribution of the elements across the wafer. The samples in the effusion cells are independently heated so the desired flux is gained from each cell. The independent shutters are opened depending on what layer must be fabricated. The control of these shutters allows for the fabrication of different layers of pure elements. When multiple gates are open, compound layers can be fabricated. This technique allows for the fabrication of extremely well controlled layer thicknesses, which means it has the ability of creating layers only a few atomic layers thick [2].

Parameters of the cubic crystal lattice of the AlGaAs and GaAs crystals are different. As a result there is an inherent lattice mismatch. To reduce the strain one can slightly alter the composition of the AlGaAs layer. One can change the compsition of the AlGaAs layer to $\mathrm{Al}_x\mathrm{Ga}_{1-x}\mathrm{As}$, where x refers to the lattice constant by Vegard's law,

$$a_0(Al_xGa_{1-x}As) = a_0(GaAs) + x[a_0(AlAs) - a_0(GaAs)] \tag{2.1}$$

where a_0 is the material lattice constant in the absence of any strain [40].

As a result of the nature of the band gap of the GaAs layer compared to the band gap of the two AlGaAs layers, a quantum well is produced (see Figure 2.4); a doping agent is formed between the layers and the delocalised electrons then fall into the well.

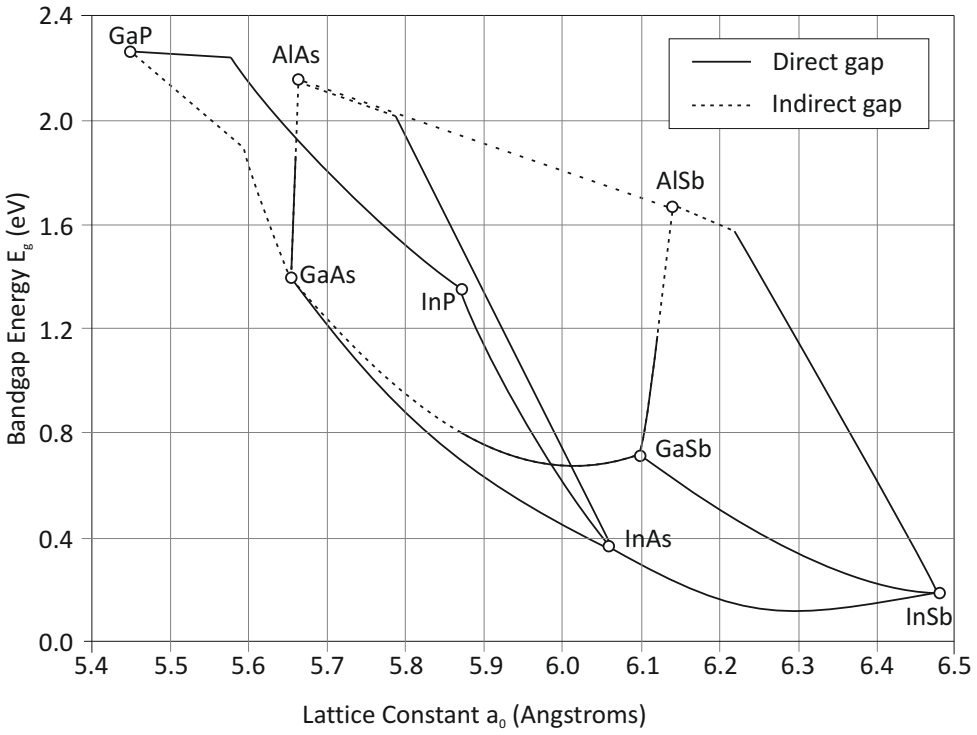

Figure 2.4: Bandgap energy and lattice constant of various III-IV semiconductors at room temperature.

The AlGaAs is doped with Si, which donates electrons. Electrons fall into the GaAs, because this lowers their energy. The resulting positive charge on the Si atoms creates a potential that holds the electrons at the GaAs/AlGaAs interface, creating the 2DEG. Figure 2.5 shows the typical layered structure of the wafers used in this thesis. The formed heterojunction is modulation-doped which means the 2DEG is spatially separated from the ionised donors. This allows high values of electron mobility to be achieved. The repeating structure of GaAs and AlGaAs on which the 2DEG structure is formed is called a superlattice. Its purpose is to bend any threading dislocations coming from the substrate and confine them at the interfaces in the superlattice so that the surface above is dislocation-free. This creates a smooth 2DEG layer.

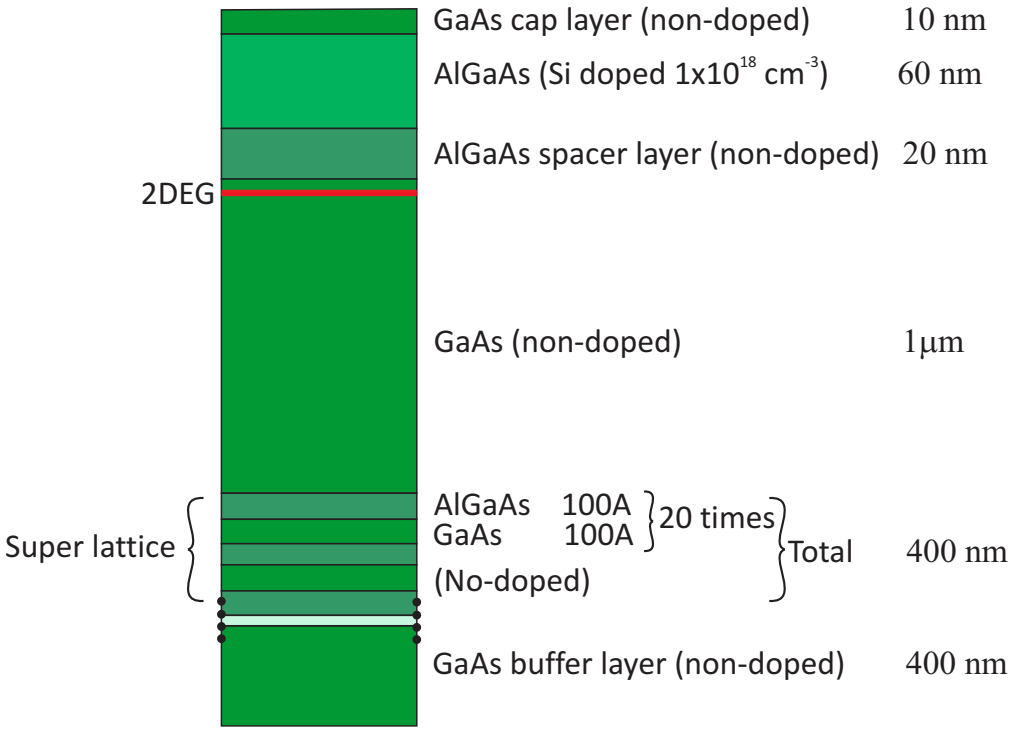

Figure 2.5: Schematic of the GaAs/AlGaAs heterostructure where the two dimensional electron gas is formed.

2.3 Metallic Surface Gates

To understand how the sensor operates, one must explain how the device is controlled. As described, the sensor can be made up of a 2DEG, a quantum dot and an SET. Much of their control is performed by the gates as shown in Figure 2.1. When negatively biased, the gates deplete regions of the 2DEG underneath. The 2DEG can be considered as a thin sheet of electrons within the wafer. This sheet can be shaped and controlled in a number of ways. The first is with the etching of a mesa structure. A mesa pattern isolates the sample region from the rest of the wafer. The mesa patterning is generally done using an acid etch process, cutting away areas of the unwanted wafer to below the 2DEG layer. Further manipulation of the 2DEG is done with the use of electrostatic metallic surface gates.

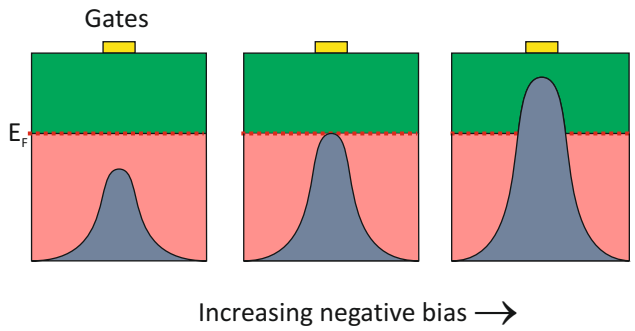

Figure 2.6: Demonstration of pinch-off of the channel. The red colour represents the 2DEG and the flow of electrons. the dark blue colour represents the depleted region caused by the gate (yellow), and the green part represents the rest of the substrate.

The surface gates are fabricated on top of the mesa; our gates were fabricated from gold. The negative bias of the gates depletes the 2DEG underneath the gates and can be thought of as a raising potential barrier. The more negative the bias, the greater the depletion and the higher the barrier formed. As Figure 2.6 depicts, the barrier is considered to cut through the channel until conductance through the channel is prohibited. The stopping of this conductance is known as the pinch-off, a term which will be frequently used throughout this thesis.

Gates can be fabricated in a variety of shapes and sizes. The most basic is that of the cross gate. This is a gate which uniformly crosses the entire mesa and whose depletion would result in a uniform blocking of the current. The next to consider is the split gate, which is a cross gate that contains a gap in the centre. This changes the situation such that at a bias at which the cross gate would have stopped conductance, the split gate would have created a restricted channel through which current can flow through. Figure 2.7 shows how this channel becomes more restricted with increasing negative bias on the cross gate. Eventually this results in the channel being blocked.

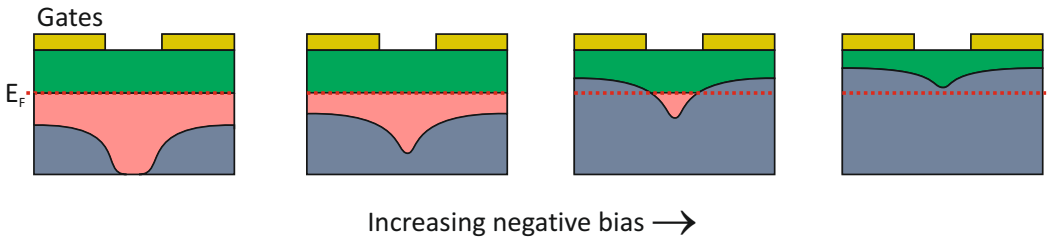

Figure 2.7: Depiction of how an increasing negative bias on surface split gates increases the depletion reigion. The third image shows the split gates forming a small channel before pinching off entirely.

A gate of the shape shown in the left diagram of Figure 2.1, the QD gate, when biased below the pinch-off voltage creates a pool of electrons that are isolated from the rest of the 2DEG, creating the so called quantum dot. As the negative bias is increased, it essentially raises the potential barriers, forming the quantum dot, as well as lifting up the energy of the electrons within the dot. A negative bias that is too high can deplete the dot of electrons entirely. The second gate used in our device is the point contact gate. This, in conjunction with our QD gate acts like a split gate and creates a thin restricted channel between the two gates - this is what is referred to as the point contact (PC).

The potential of the system was simulated using FlexPDE. This was achieved by solving the Poisson equation in the 3D case:

$$\nabla \cdot (k\varepsilon_0 \nabla V) = \rho \tag{2.2}$$

where k is the dieletric constant, $\varepsilon_0 = 8.85 \times 10^{-12}$ F/m, and ρ is the charge density. The FlexPDE simulation can be seen in Figure 2.8.

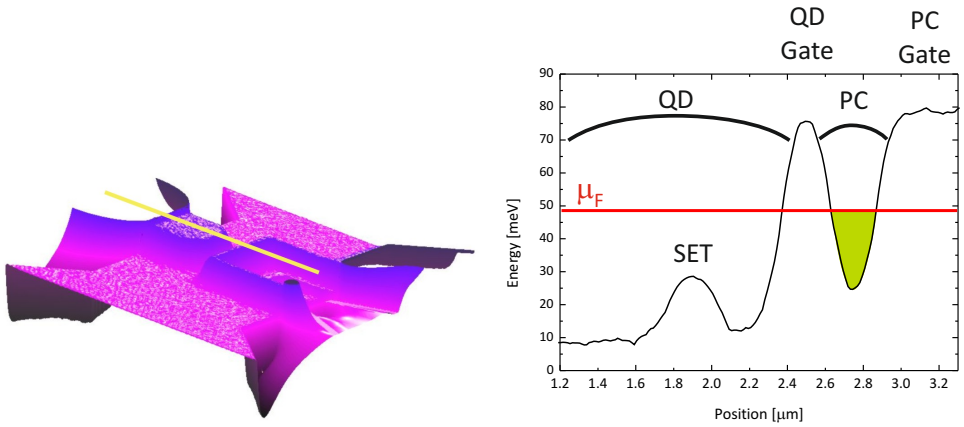

Figure 2.8: Left: Example of potential calculation with the voltage -1 V applied to the QD gate and PC gate. Right: Cross-section of the potential along the yellow line of the left picture. The green area represents the conductance channel of the PC. The channel is filled with electrons up to the Fermi level μ_F. Positions of the QD, PC and corresponding gates are indicated.

2.4 Point Contacts

An alternative method for readout of the QD is a point contact (PC), to detect changes in the charge state of the dot. The point contact in these experiments is simply a narrow conduction channel formed via a metallic gate mounted on the surface of the substrate, which when negatively biased depletes a region underneath, reducing the size of the conduction channel. This narrow conduction channel is strongly coupled to the QD in our system due to close proximity.

PCs have been used for a variety of uses such as the detection of ballistic electrons [41] and by controlling the coupling between two electron systems, it was not until recently that they were used to measure the charge or voltage on an external device much like a field effect transistor [42–44]. From low frequency noise measurements such as these, PC devices have been seen to show enough charge sensitivity to resolve small changes in electric fields such as that caused by the motion of a single electron [45–48]. The observable low frequency resistance fluctuations in PCs can thus arise from changes in the charge state of a QD near the constriction [49].

2.5 Quantum Dots

The name 'Quantum Dot', QD, is used to refer to a relatively small region of space which has been shown to display a variety of physical phenomena unexpected from the classical regime. There are a variety of objects covered by the term QD from molecular systems such as metallic grains, to the most common form as a semiconductor nanostructure, like those studied here. Quantum dots are essentially a generic example of a confined structure containing electrons.

If the size of the confinement is comparable to the de Broglie wavelength of the delocalised electrons then quantum effects can be observed in properties of the electron gas. An example of this would be a two-dimensional electron gas, 2DEG, as it is only considered to exist in two classical dimensions, because motion in the third dimension is restricted by a potential well. Further restrictions in another dimension causes a thin channel of electrons to be formed known as a one-dimensional wire. Restriction in the third dimension would create an essentially zero-dimensional object, the semiconductor QD, a small isolated region of electrons.

The distance between neighbouring energy levels in typical structures with characteristic dimensions in the range of 10-100 nm is approximately a few meV. The quantisation of energy, or the reduction of the dimensionality of the system, is directly reflected in the dependence of the density of states on energy [50] as shown in Figure 2.9. For a three-dimensional bulk material with effective electron mass m*, there is free motion of electrons in all three directions with the energy:

$$E = \frac{\hbar^2}{2m^*}(k_x^2 + k_y^2 + k_z^2) \tag{2.3}$$

where $k_{x,y,z}$ represent the wavevectors in all three directions. Therefore the energy spectrum is continuous and the corresponding density of states (DOS) is that of a bulk system, $D_s(E) \propto E^{1/2}$. However, in a two-dimensional system the electron

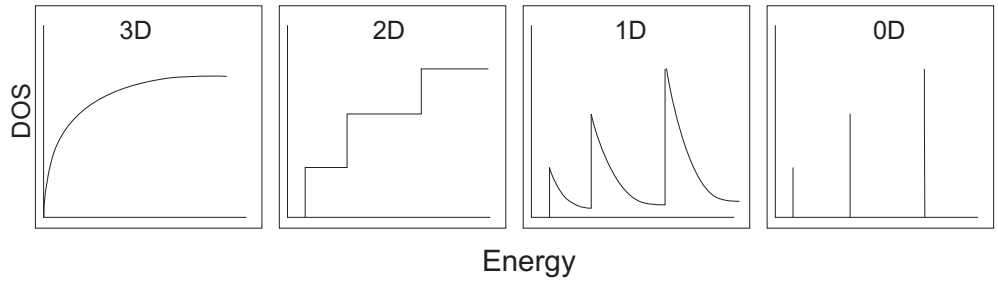

Figure 2.9: Density of states as a function of energy in systems with different numbers of spatial dimensions: 3D, bulk material; 2D, quantum well; 1D, quantum wire; 0D, quantum dot.

motion is restricted in the z-direction giving rise to quantisation into discrete electric subbands. Nonetheless, motion in the xy-plane is still free:

$$E = \frac{\hbar^2}{2m^*}(k_x^2 + k_y^2) + E_z^i \tag{2.4}$$

The 3D-DOS is strongly modified in the z-direction giving quantisation energies producing step-function-like behaviour. Further confinement of another dimension would lead to a one-dimensional system with energy

$$E = \frac{\hbar^2}{2m^*}k_x^2 + E_y^i + E_z^i \tag{2.5}$$

modifying the two-dimensional system by replacing the step-like function with a system of sharp-peaks. Again, if the system is further reduced to a zero-dimensional system the energy can be represented as,

$$E = E_x^i + E_y^i + E_z^i \tag{2.6}$$

This produces a discrete energy spectrum with the DOS being represented as a series of delta-functions [51].

The delocalised electrons within the QD occupy discrete quantum levels, from which you can draw many analogies to atomic orbits in atoms. Analogies such

as the excitation and ionisation energies, which is the amount of energy required to remove or add an electron to the dot, their interactions with light, and current carrying abilities give rise to the popularly used name of 'artificial atom' in reference to QDs introduced by Maksym and Chakraborty [51].

Even within the bracket of semiconductor quantum dots, there are a variety of different types and methods of fabrication. From the chemically formed nanocrystal to the core-shelled structures formed by placing a material with a low band gap into one with a much higher band gap, to even self-assembled quantum dots. The dots in this investigation are lateral quantum dots, which are one of the most abundant types of semiconductor QDs. They are constructed from a two dimensional electron gas, and defined using negatively biased metal surface gates and mesa patterning as described in the previous section. Thus the QD is isolated from the rest of the 2DEG, as shown in Figure 2.10.

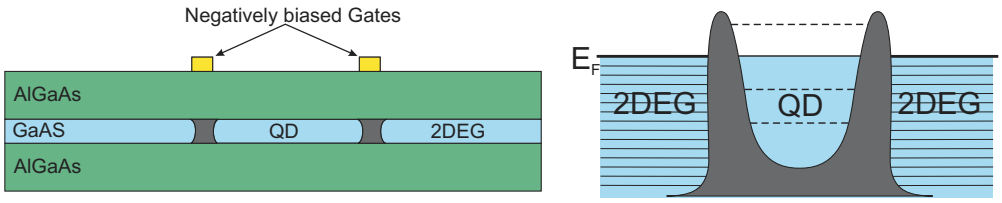

Figure 2.10: Left: Schematic of formation of a quantum dot within a 2DEG using negatively biased gates. The grey represents the depleted region. Right: A corresponding energy level diagram.

2.5.1 Photoexcitation of Quantum Dots

The photoexcitation of a quantum dot relies on the conversion of photon-to-plasmon and plasmon-to-charge. Plasmons are quanta of plasma oscillations excited in the QD upon absorption of the photons. This means that QDs have a resonant frequency of the plasma oscillations, giving a strong dependence on the size of the dot to the frequency of photon it absorbs.

To derive the relation between these, one first must consider the confining potential of the dot. It was first considered, as the simplest model, to have a hard wall potential for the dot, but when comparissons were made between that and values calculated from experiments carried out in magneic fields, it was noted that the value was more than twice the measured value [3, 52]. A more realistic confining potential can be estimated from a simplified model of the QD as seen in Figure 2.11.

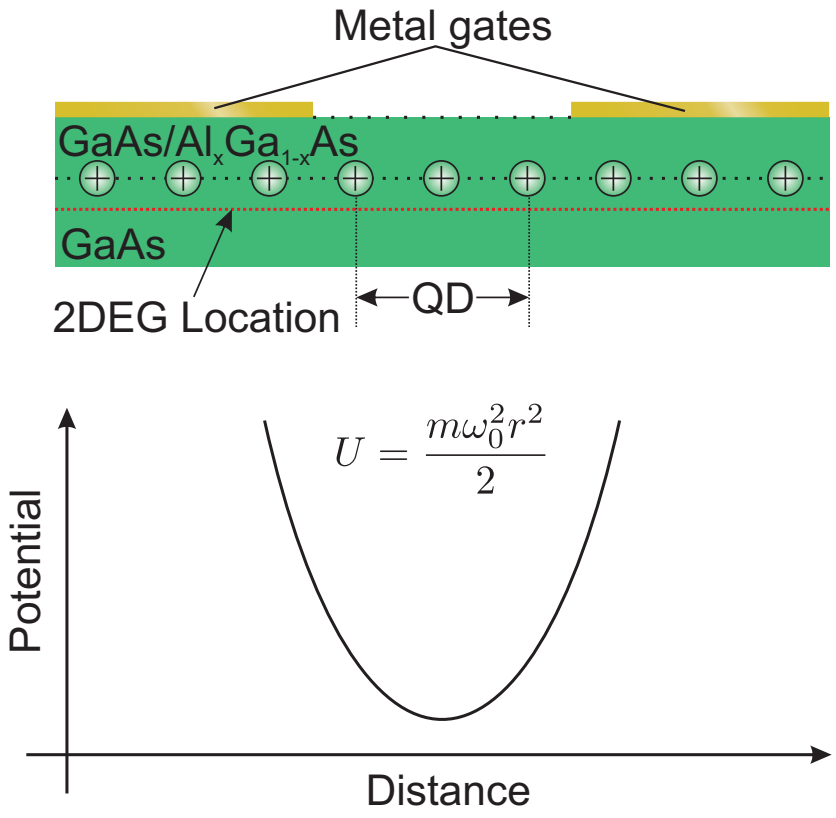

Figure 2.11: Simplified model of heterostructure crystal covered by a metal gate with a hole. Beneath the upper graphic is a depiction of the potential induced by the positive background charge on the plane of the 2DEG.

Here, the new potential is:

$$U = \frac{m\omega_p^2 r^2}{2} \tag{2.7}$$

where ω_p is the plasma frequency, m is the mass of the charge carrier, and r is the

radius from the centre of the dot. In Figure 2.11 we have a 2DEG layer of density n_s (the carrier density), positioned beneath the crystal surface. This layer is neutralised by a remote layer of background positive charges at a depth just above the 2DEG. Metal gates formed on the surface are negatively biased to form an island in the 2DEG (QD). The confinement potential formed by the bare possitive background charge can be found by taking the prolate spheroidal coordinates r, z, φ through $\xi = \sinh u$, $\eta = \cos v$ and $r = R(\cosh u)\sin v$, $z = R(\sinh u)\cos v$ with parameters u and v being $u > 0$, $0 \leq v \leq \pi$. A potential formed by a bounded conducting plane with a circular aperture, situated in a uniform electric field E in a half-space $z < 0$ along the z-axis (perpendicular to the metal plane) is derived in an analytical form as [53]

$$\varphi = -E\frac{z}{\pi}\left(\arctan\frac{1}{\xi} - \frac{1}{\xi}\right) \text{ at } z > 0 \text{ and}$$

$$\varphi = -E\frac{z}{\pi}\left(\pi - \arctan\frac{1}{\xi} + \frac{1}{\xi}\right) \text{ at } z < 0.$$

The coordinates originate at the centre of the aperature with the z-axis perpendicular to the interface. In this case, the electric field $E = -4\pi n_s e/\varepsilon_{GaAs}$ is induced by a positively charged sheet below the surface as seen in Figure 2.11 and the effect of the GaAs-vacuum interface is taken into account by assuming an additional electric field $E' = 4\pi n'_s e/\varepsilon_{GaAs}$ induced by a mirror charge with a sheet density $n'_s = (\varepsilon - 1)/(\varepsilon + 1)n_s$, ε_0 is the permittivity of free space, and ε_{GaAs} is the permitivity of GaAs. A first order approximation of the parabolic potential is taken as $U = e\varphi$ this gives

$$U = \frac{4}{(1+\beta^2)^2}\frac{e^2 n_s}{R\varepsilon_{eff}}\frac{r^2}{2} + U_0 \tag{2.8}$$

where $\beta = h/R$, with h being the depth of the 2DEG and R being the radius of the dot, $\varepsilon_{eff} = \varepsilon_0(\varepsilon_{GaAs} + 1)/2$. U_0 is a constant and thus does not affect

the plasma oscillation frequency. Now combining Equations 2.7 and 2.8 a plasma oscillation of the dot has the frequency:

$$\omega_p^2 = \frac{4}{(1+\beta^2)^2}\frac{e^2 n_s}{R\varepsilon_{eff} m^*} \tag{2.9}$$

where the effective mass in GaAs $m^* = 0.069\, m_e$. ω_p is the angular frequency, $\omega = 2\pi f$. Taking the average radius of our dots to be $R = 0.75$ μm and a typical depth to be $h = 100$ nm, a typical resonance frequency for the dot will be $f \approx 1.2$ THz [54]. The plasma oscillations then decay via single particle-electron-hole excitations [55]. It is these excitations which we detect. Figure 2.12 is a simulation showing the dependence of the plasma resonance frequency on the size of the quantum dot.

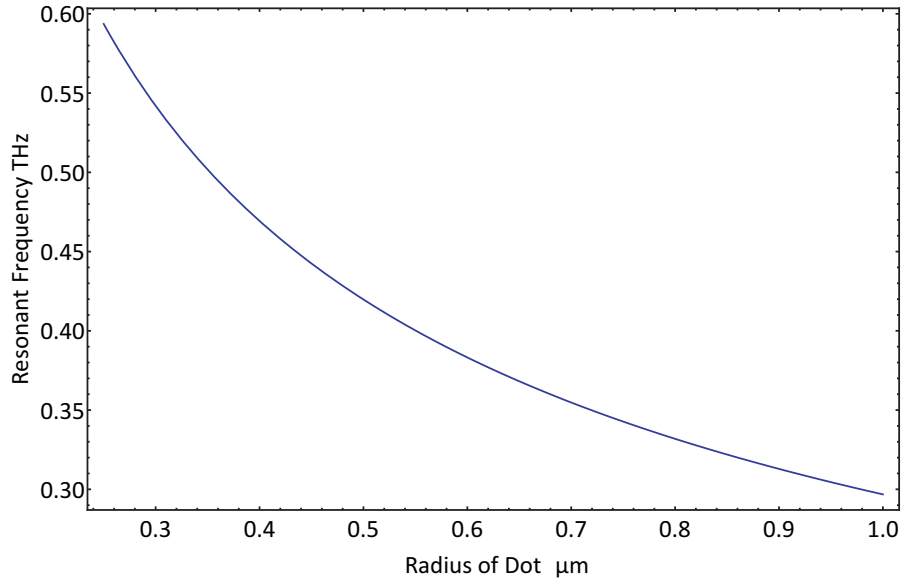

Figure 2.12: The dependence of the resonance plasma frequency of a quantum dot on the size of the dot.

Plasma oscillations also have some dependence on the mobility of the substrate as the higher the mobility the narrower the spectral response. Typicaly our samples have a mobility of $\mu = 3 \times 10^5$ cm^2/Vs.

2.6 Single Electron Transistors

The single electron transistor (SET) is an essential part of the QD-SET terahertz detector. Similar to the conventional field-effect transistor (FET) it forms an electrical pathway controlled by a gate electrode.

SETs are based on the phenomenon of quantum tunnelling. This is observed when two metallic electrodes are separated by an insulating barrier. Figure 2.13 shows the structure of a simple SET. It consists of two leads, the source and the drain, which are connected via two tunnel junctions forming a metallic island. Capacitively coupled to this island is a third electrode, the gate, which is used to control the electrical potential of the island. In this way, the current through the SET can be controlled/influenced.

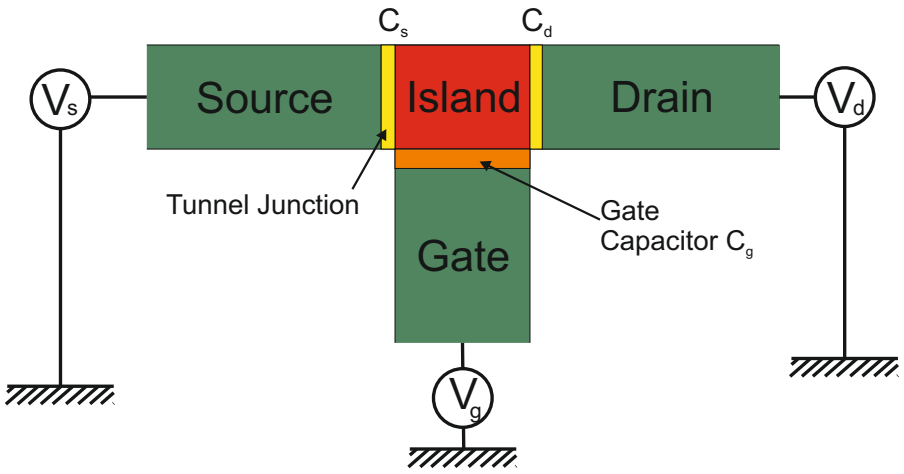

Figure 2.13: Schematic of SET, showing voltages across the SET, V_s and V_d, and the gate voltage V_g .

At low source-drain bias voltages, suppression of current flow is caused by the process of Coulomb blockade. The Coulomb blockade is dependent on the charge state of the island and therefore can be modulated by the gate voltage. Varying the gate voltage causes what are known as Coulomb blockade oscillations (CBO). They are oscillations in current and are a result of one electron being added to the island.

This chapter will explain the key concepts of SETs as well as the additional features brought about by superconducting single electron transistors (SSETs), which will be needed throughout the rest of this thesis.

To understand the SET we begin by explaining the component parts that make up the device, and build these up to the final SET. This chapter was compiled using a number of sources to which the reader is referred [56–64].

2.6.1 The Tunnel Junction

The SETs used in this thesis are an $Al/Al_2O_3/Al$ type, formed via a shadow evaporation process. This process involves two evaporations at different angles. After the first evaporation has occurred, oxygen is allowed into the sample area causing an oxide layer to form on the evaporated aluminium. The oxygen is then evacuated and the second evaporation occurs. The different angles result in an overlap of the metals. It is the overlapping of these metals with the oxide layer in between which we consider to be our tunnel junction, see Figure 2.14. The tunnel junctions (referred to as NIN junctions for normal metals) that construct an SET are arguably the most fundamental component. In the classical regime of electrodynamics, no current can flow through the insulating barrier, as the kinetic energy of the electron on one side of the barrier is less than the barrier potential. However, if viewed from a quantum perspective then there is a non-zero probability that an electron at the Fermi energy can tunnel through the barrier into a lower energy state on the other side. This occurs because if the insulator is sufficiently thin, the wave-functions of electrons of one metal extend into the other metal such that the probability of tunnelling occurring becomes significant. A finite resistance across the junction confirms this effect.

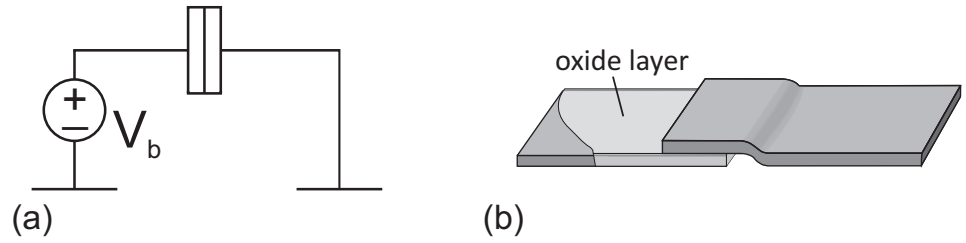

Figure 2.14: (a) Circuit diagram of a single tunnel junction. (b) Schematic of a typical construction of a tunnel junction showing the sandwiching of an oxide layer between two metals.

If the barrier is made sufficiently resistive, then at low bias voltages there is no current flow through the junction. If the bias voltage is slowly increased, the electron gains just enough energy to tunnel through the barrier. One can characterise the junction with a capacitance C_j, this can be approximated to be $C_j \sim \frac{\varepsilon A}{d}$, akin to a parallel plate capacitor, where ε is the permittivity of the dielectric material, A is the area of the junction overlap and d is the insulator thickness. For a tunnel junction of capacitance C_j, the charging energy E_c, needed for a single electron to overcome the Coulomb repulsion and tunnel through is given by:

$$E_c = \frac{e^2}{2C_j} \tag{2.10}$$

If the bias voltage V, is increased on one side of the junction, tunnelling will occur if $eV > E_c$.

In a system with low capacitance the charging energy is high and built up voltage can be excessive enough to prevent an electron from tunnelling. For a voltage-biased junction a charge $+Q$ and $-Q$ is stored on either side of the barrier and for current to flow, the case $Q > e/2$ must be satisfied. This is demonstrated if one investigates the charging energy as a function of the charge Q. In units of e this forms a parabola, and one can consider an electron moving up this parabola as the source current is increased until Q reaches a value of $e/2$ at which point the

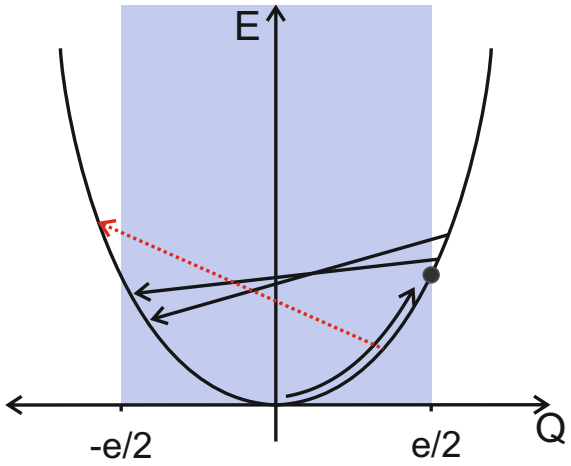

Figure 2.15: Parabola of the charging energy as a function of the charge Q . The straight black arrows show energetically favourable tunnelling events, while the red arrow depicts a tunnelling event that cannot occur.

electron can tunnel to a lower energy state, as shown in Figure 2.15. As electrons can only tunnel to lower energy states, at low voltage bias current is suppressed causing a Coulomb blockade.

The blockade region is seen as a plateau about zero bias voltage in the I-V curve, for $|V| < V_c = e/2C_j$ (see Figure 2.16). V_c can be referred to as the critical voltage, analogous to the critical current in Josephson junctions. No current flows below this voltage. As this critical voltage is exceeded, current begins to flow and the slope of the I-V curve becomes like that of a conventional resistor (see Figure 2.16).

In order for a Coulomb blockade to be set up, the tunnel junction must have a minimum quantum resistance R_q, derived from the uncertainty relation, where E_C must exceed the uncertainty in energy of a single electron. The lifetime of an excess electron can be estimated as $\tau = R_T C_j$, this is analogus to the time constant for charging a capacitance C_j through tunnel resistance R_T, and the energy gap associated with a single electron is $\triangle E \ll E_C$. This gives an uncertainty relation of [65],

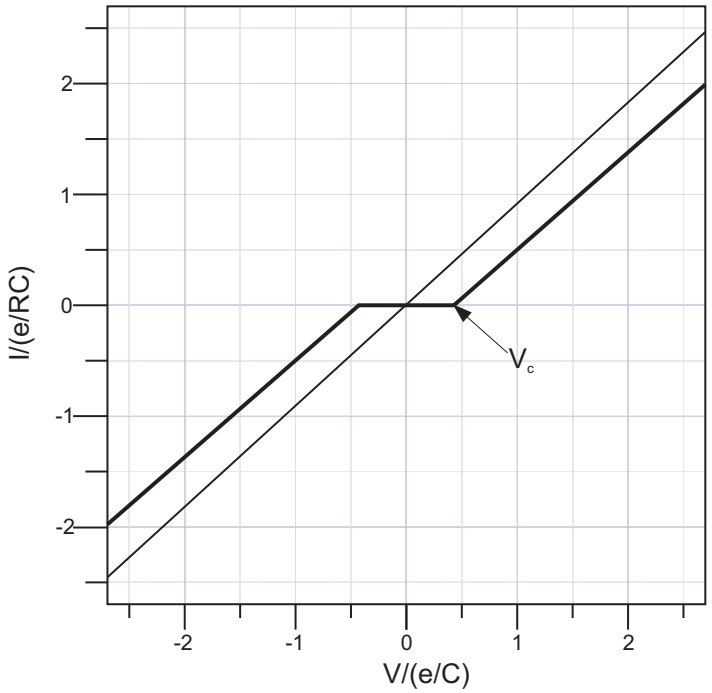

Figure 2.16: An idealised I-V curve for a single tunnel junction, voltage biased at T = 0 K.

$$\triangle E \approx \frac{h}{\tau} = \frac{h}{R_T C_j} \ll \frac{e^2}{2C_j} \tag{2.11}$$

Equivalently,

$$R_q \ll R_T, \qquad R_q = \frac{h}{e^2} \simeq 25.8\,\mathrm{k}\Omega \tag{2.12}$$

2.6.2 Single Electron Box

The simplest circuit which demonstrates single electron charging behaviour is the single electron box, which consists of a tunnel junction in series with a capacitor. This creates a conducting island. The schematic of this can be seen in Figure 2.17(a).

The fabrication of such a device is relatively simple; one of the arrangements is that of a small metallic grain (the island) embedded within an oxide, as in Figure 2.17(b). Here the top oxide layer is thin enough for electrons to tunnel

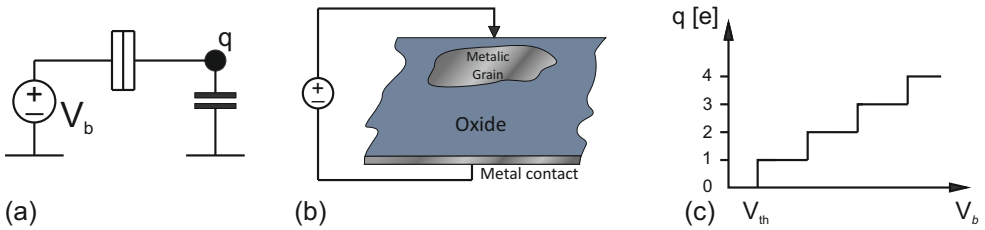

Figure 2.17: (a) Simplified circuit diagram of a single electron box. (b) Depiction of an example of a single electron box. (c) The rise in charge, q, in units of e as a function of the bias voltage, showing quantised single electron charging.

through and the coupling to the bottom conductive layer can be thought of as the capacitor. Figure 2.17(c) shows the build up of charge in quantised units of e on the island as the bias voltage is increased. The energy for an electron to tunnel onto the island is affected by the potential difference across it. This results in a charging energy of

$$E_{ch}(n) = \frac{(ne - Q_g)^2}{2C_\Sigma}, \tag{2.13}$$

where $Q_g = C_g V_b$ and C_Σ is the sum of capacitances for the tunnel junction and the capacitance between the island and ground. C_g is the gate capacitance, V_b is the bias voltage and n is the number of electrons on the island. For electrons to tunnel this charging energy must be overcome for each electron in a series of discrete steps. Figure 2.17(c) shows the 'Coulomb staircase'. This is the relation between the charge on the island and the bias voltage. This can also be demonstrated with energy level diagrams (see Figure 2.18). These diagrams depict the electrochemical potential of the source on the left, and the energy levels on the other side of the barrier show the difference in charging energy between the filling states of the island. This is given by Equation 2.14.

$$E_{ch}(n+1) - E_{ch}(n) = (n + \frac{1}{2} - \frac{Q_g}{e})\frac{e^2}{C_\Sigma} \tag{2.14}$$

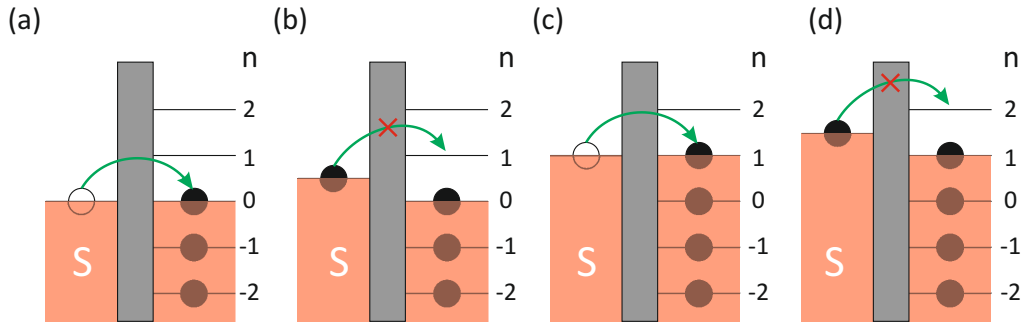

Figure 2.18: Energy diagram for a single electron box. Electron transport is only allowed when the source and drain potentials are matched.

2.6.3 The Double Tunnel Junction

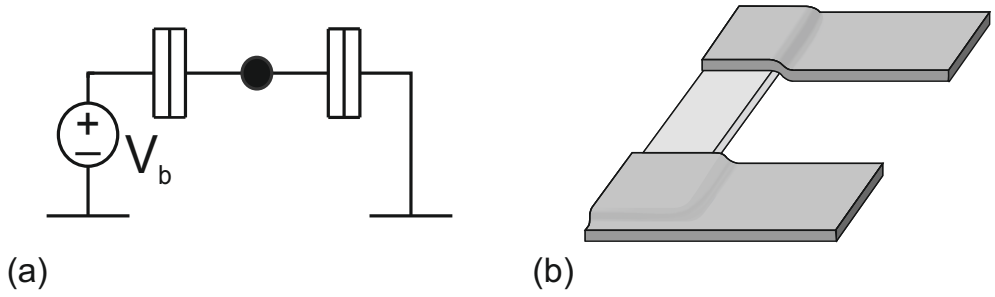

Figure 2.19: (a) Circuit diagram of a double tunnel junction. The dot in the centre represents an island which can be charged like the single electron box. (b) Schematic of a typical construction of a double tunnel junction showing a metallic island coated in an oxide layer, and connected via two metallic leads.

Now we consider two tunnel junctions in series as an extension to the single electron box, depicted in Figure 2.19. Here an island is formed between the two junctions. A discrete charge is present on the island if both junctions have a high enough resistance $R > R_q$. As for the single electron box, the charging energy of a double tunnel junction is given by Equation 2.13, only this time $C_\Sigma = C_s + C_d$ and $Q_g = C_s V_s + C_d V_d + Q_0$ where Q_0 represents the intrinsic charge offset on the island. The energy level diagrams for the double tunnel junction are also extended, with the closing of the island and the inclusion of the electrochemical potential on the drain. Figure 2.20 shows the flow of current through a double

tunnel junction for four particular combinations of bias voltages (V_{sd}) and charges on the island (Q_g). The first two are with $V_{sd} \sim 0$ for two values of Q_g. For $V_{sd} \sim 0$ and $Q_g = 0$ (a) it is energetically feasible for electrons to tunnel from the source into the $n = 0$ state and out into the drain causing current to flow. For the next situation, where $Q_g = 0.5e$ (b), current is restricted as although an electron can tunnel into the $n = 0$ state on the island, it is unable to tunnel out into the drain. The situation for $Q_g = 0$ and $Q_g = 0.5e$ when $V_{sd} = \frac{e}{C_\Sigma}$ are shown in (c) and (d) respectively. For both cases of Q_g, current may flow via electrons tunnelling into the $n = 0$ state and out into the drain, but for $Q_g = 0$ there is also the possibility of $n = -1$ tunnelling to occur, increasing current flow.

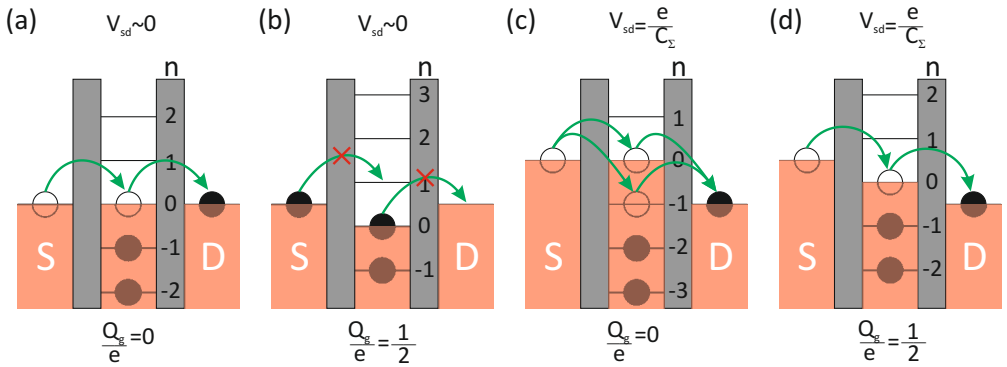

Figure 2.20: Energy diagram for a double tunnel junction showing allowed transitions through the double tunnel junction, for varying source drain potential and gate charge.

2.6.4 The Single Electron Transistor

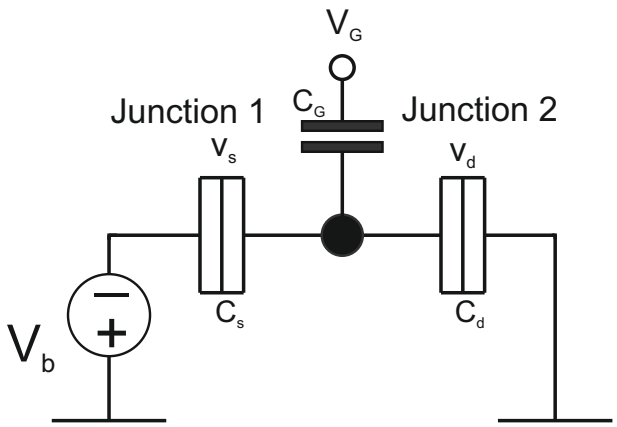

Figure 2.21: Circuit diagram of a single electron transistor.

The final piece of this construction is the addition of a gate electrode, which is capacitively coupled to the island. Similar to the previous two cases the charging energy is an important parameter of the SET. As covered in the two previous sections the tunnel junctions of the SET can be modelled by capacitors as depicted in Figure 2.21. At zero bias voltage, there is no current flow through the SET. The device is in the Coulomb blockade regime. The electron must first overcome the Coulomb energy, or charging energy (Equation 2.13), given again below:

$$E_c = \frac{(ne - Q_g)^2}{2C_\Sigma},$$

where C_Σ is the total capacitance between the SET and the surroundings ($C_\Sigma = C_s + C_d + C_g + C_{env}$) and $Q_g = C_s V_s + C_d V_d + C_g V_g + Q_0$ (see Figure 2.13). This allows Q_g to be adjusted by altering V_g. This adjustment enables the bias voltage below which Coulomb blockade occurs to be changed. If the bias voltage across the source and drain terminals of the SET is large, $V_s > e/2C_\Sigma$ and $V_d > e/2C_\Sigma$, current will flow through the SET with no charge quantisation. When a small bias voltage across the SET source and drain terminals is applied, which is less than the charging energy, current is blocked. Now as the gate voltage is steadily

increased, we move up the parabola as described in Section 2.6.1 and no electron flow occurs until the gate capacitor is charged with exactly $\pm e/2$. At this point, the electron energy state for the $Q = e/2$ state becomes degenerate with that for the $-e/2$ state and electrons can tunnel one by one through the SET. The charge on the island must always be a multiple of the electron charge. Thus charge can fluctuate between the two states separated by $|e|$ and current can flow. When increasing the gate voltage further, the Coulomb blockade is set up again as it is energetically unfavourable for the charge on the island to change by e so that the current through the SET is suppressed.

2.6.5 Coulomb Oscillations

As a result of the charging energy causing single electron tunnelling, the current through an SET varies periodically with gate voltage, in contrast to the threshold behaviour of an FET. The period of oscillation is given by $\triangle V_g = e/C_g$. The gate voltage can be adjusted so that the SET turns "on" and "off" again every time a single electron is added to it. This is why it makes the most sensitive electrometer - it is extremely sensitive to the variation of the potential.

Conditions For Observing Coulomb Blockade Oscillations

In order to observe Coulomb blockade oscillations (CBOs) three conditions must be met. The first is that the thermal energy of the electrons must be significantly smaller than the charging energy, $E \sim E_c/10$, so that thermal fluctuations cannot overcome the charging energy and cause random charge oscillations:

$$k_b T < \frac{E_c}{10} \tag{2.15}$$

To satisfy this condition the sample must be cooled down, typically to $T < 1\,\mathrm{K}$. The second is that the wavefunctions of the electrons should be localised on one side of the tunnelling barrier, so that charge can be quantised on the island. It can be shown that this translates to having a minimum resistance (R_q) for the

tunnelling barrier as described in Section 2.6.1. R_q was derived in Equation 2.12.

$$R_T > R_q = h/e^2 = 25.81\,\mathrm{k}\Omega \tag{2.16}$$

This follows from the requirement that the energy uncertainty of the electron is less than the charging energy. The final third condition is that the bias voltage should be less than the charging energy, otherwise the flow of electrons across the junctions will be continous:

$$eV_b < E_c \tag{2.17}$$

2.6.6 Transport through an SET

The transport of electrons through a normal SET can be seen in Figure 2.22. Here, the tunnelling of electrons through the first junction onto the island affects the transmission probability of tunnelling out of the second junction off the island. This is called space correlation. The potential of the island is determined by capacitive voltage division and is given by:

$$\varphi = \frac{C_s}{C_\Sigma}V_s + \frac{C_d}{C_\Sigma}V_d + \frac{(ne)^2}{2C_\Sigma} \tag{2.18}$$

In the figure it can be seen that an electron tunnelling to the lower potential of the island causes the electric potential to rise by $2E_c$. The island potential now exceeds the electrochemical potential μ_F of the drain and so the electron now has the ability to tunnel out to the drain electrode. The potential of the island returns to the initial value.

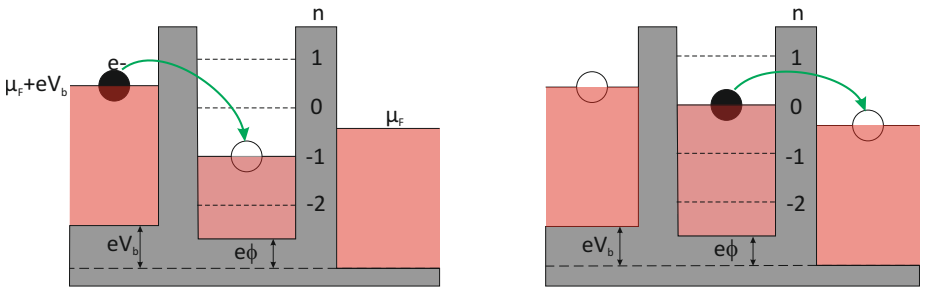

Figure 2.22: Transport of electrons through an SET.

Again, as this second tunnelling event has lowered the island potential, another electron can flow onto it from the source electrode. Thus a current flows through the SET. The condition of tunnelling can be changed by the gate electrode. This can be demonstrated in a stability diagram, showing the conductance across an SET whilst both gate voltage and bias voltage are varied. This maps out stability diamonds of regions where the SET is in Coulomb blockade.

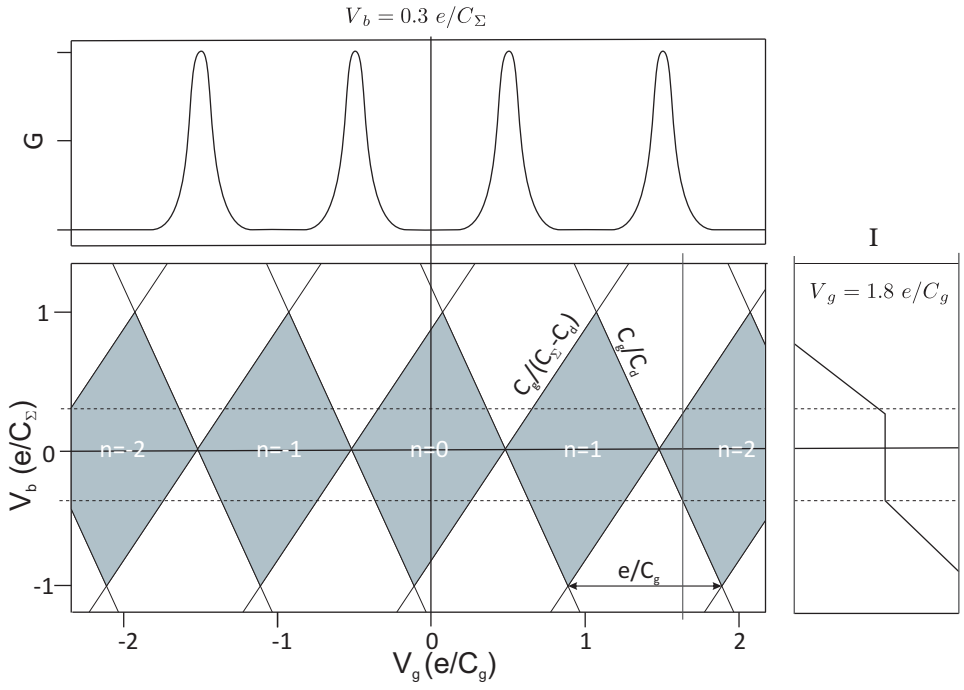

Figure 2.23: Diamond stability diagram for a single electron transistor showing I-V characteristics and Coulomb oscillations. The grey regions represent regions with zero conductance.

2.6.7 Superconducting Tunnel Junctions

It is possible to extend the SET functionality with the introduction of superconducting materials in their construction. As mentioned the SETs used in these experiments are constructed from aluminium, which becomes superconducting below its critical temperature of 1.2 K. For experiments carried out below 1 K the SET is in its superconducting state for its operation. To begin to describe the new features of a superconducting SET (SSET) I will once again start from the fundamentals in the form of an SIS junction. This is often referred to as a Josephson junction and it is this that now replaces the normal tunnel junctions in a normal SET. The Josephson effect was first predicted and discovered in 1962 by Brian Josephson, whilst as a postgrad at the University of Cambridge. It was there he proposed that between two superconductors separated by a thin insulating or non-superconducting barrier, there can be the transport of Cooper pairs via tunnelling. There are in fact two main mechanisms for tunnelling through an SIS junction, either dispersive quasiparticle tunnelling or resonant Cooper pair tunnelling.

Dispersive quasiparticle tunnelling dominates the tunnelling when a bias voltage of higher than $2\triangle$ is present. $2\triangle$ is the minimum energy required to break a Cooper pair into its constituent quasiparticles. A quasiparticle is the term given to an electron which is affected by external forces or interactions. This has no effect on the charge or the fact the electron is a fermion but it does affect the effective mass of the electron. The quasiparticle in this case can be considered a Bogoliubov quasiparticle. In this instance the quasiparticle can be considered to tunnel as a conventional electron. Cooper pair tunnelling can exist if the source and drain potentials are aligned as depicted in Figure 2.24.

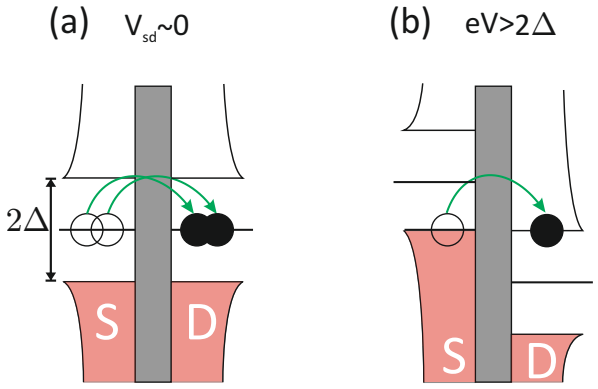

Figure 2.24: Energy diagram of tunnelling through a single SIS junction.

2.6.8 Superconducting SET

The SSETs investigated in this thesis comprise two of these Josephson junctions, forming an island, much like the double tunnel junctions described in Section 2.6.3. The electron-phonon interaction which causes electrons of opposing spin and momentum to be bound into Cooper pairs, with tunnelling charge $2e$, modifies the charging energy needed to overcome the Coulomb blockade, as well as the minimum resistance required R_q, for the observation of Coulomb oscillations. The quantum resistance is now:

$$R_q = h/4e^2 = 6.432\,\mathrm{k}\Omega \tag{2.19}$$

On top of the $2E_c$ required for normal state electron tunnelling through the junction, the superconducting junction also imposes another energy scale with the superconducting gap energy, $\triangle$. For single electron tunnelling through each junction, an extra 2Δ is needed to split the Cooper pair into quasiparticles. This increases the Coulomb blockade energy for the SSET by 4Δ. Bulk aluminium has a gap energy of approximately 250 μeV, so the energy can be increased by as much as 1 meV. This prohibits single electron tunnelling in a superconducting SET at low bias voltages. Single electron tunnelling can occur in the region

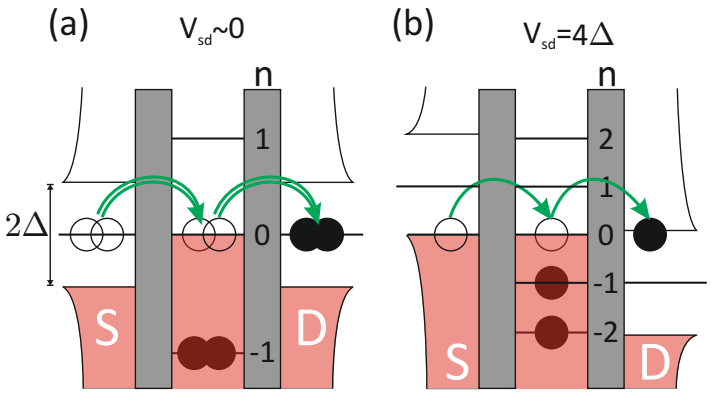

Figure 2.25: Energy diagram of tunnelling through a double superconducting tunnel junction.

$4\triangle \leq eV_{sd} \leq 4\triangle + 2E_c$. However there are processes that allow current flow at lower bias voltages, the first of which involves the tunnelling of a Cooper pair onto the island through a resonant process, as seen in Figure 2.25.

With zero bias no net current flows as tunnelling of Cooper pairs are equally likely from either lead, in the form of supercurrent tunnelling. As the bias is increased it becomes favourable to tunnel from one lead (source) to the island and then from the island to the next lead (drain). Under this regime the energy level separation on the island is $2e/C_\Sigma$. This has the effect of doubling the period of the CBOs to $2e$ when the gate voltage is varied. As the bias voltage is increased we move out of resonance and this Cooper pair current is suppressed causing what is known as the Cooper pair peak (CP peak). There are a number of resonances which occur on an SSET. These can be considered to follow:

$$m\kappa_i V(Q_0) = 2mE_c \left[(-1)^{i-1}\left(\frac{Q_0}{e} - n\right) + \frac{m}{2}\right] + q\triangle \tag{2.20}$$

where $\kappa_i = 1-(C_1+C_g/2)/C_\Sigma$ is the fraction of the applied bias voltage appearing across junction i, m is the number of electrons transferred, q is the number quasiparticles created, and n is the initial charge state of the island. Using this equation and the possible values for m, q, n creates the diamond stability diagram for the SSET shown in Figure 2.29. Setting $m = 2$ and $q = 0$ shows the regime

in which Cooper pair tunnelling is resonant. When placed into the equation for the first junction $i = 1$ gives a positive slope, and for the second junction $i = 2$ gives a negative slope. At the intersection between these two lines is the place in which a Cooper pair resonance exists on both junctions, this is the position of the $3e$ peak, otherwise referred to as the DJQP (double Josephson quasiparticle peak). This peak is a result of a Cooper pair tunnelling into the island followed by a single electron tunnelling out to the drain (called a J-e process), then another electron tunnelling in from the source into the island to form a Cooper pair which then tunnels out. This peak occurs at $eV_{sd} = 2E_c$. For this processes to occur a condition of $E_c > 2\triangle/3$ must be met. A pictoral description of this process is shown in Figure 2.26.

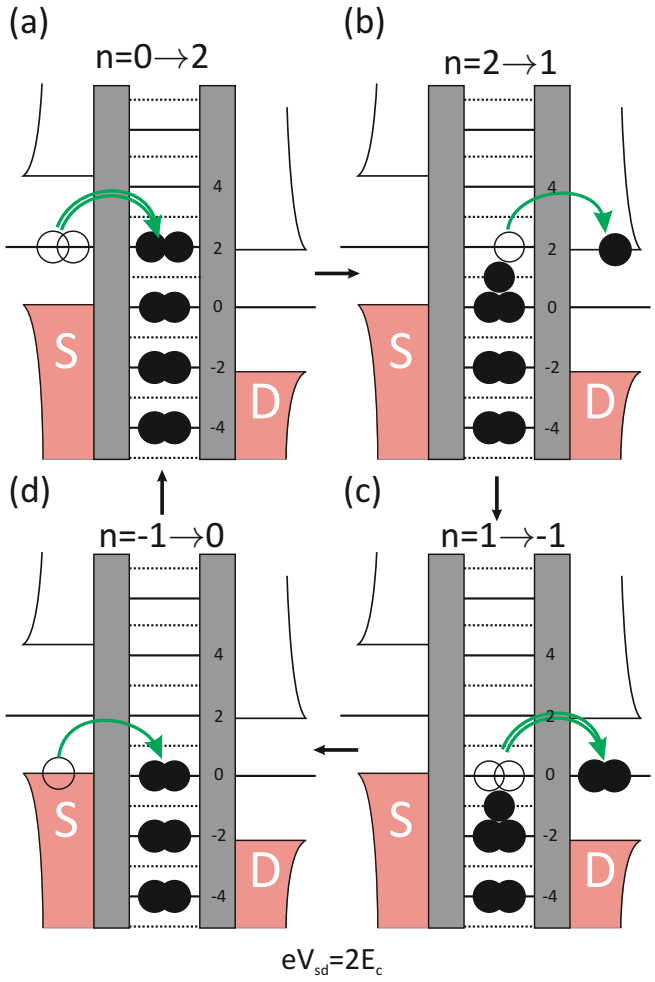

Figure 2.26: Energy diagram of the $3e$ peak (DJQP) cycle.

If we follow these lines of resonance, we enter a region where there is enough energy for the Josephson quasiparticle peak cycle (JQP) to be energetically favourable. For this, the energy must be between the limits $(2\triangle + E_c) \leq eV_{sd} \leq (2\triangle + 3E_C)$. In this region a Cooper pair tunnels in followed by an electron leaving as before, but this time it is then followed by an additional electron. This occurs if the levels are on resonance, as the cycle can only occur if all stages of the transition are energetically viable. At the higher end of the energy threshold the $n = 0$ level is above the gap causing an electron to tunnel out sending the level from $n = 0 \rightarrow -1$. This then suppresses the tunnelling of Cooper pairs to the island as the source is no longer on resonance with the island, see Figure 2.27.

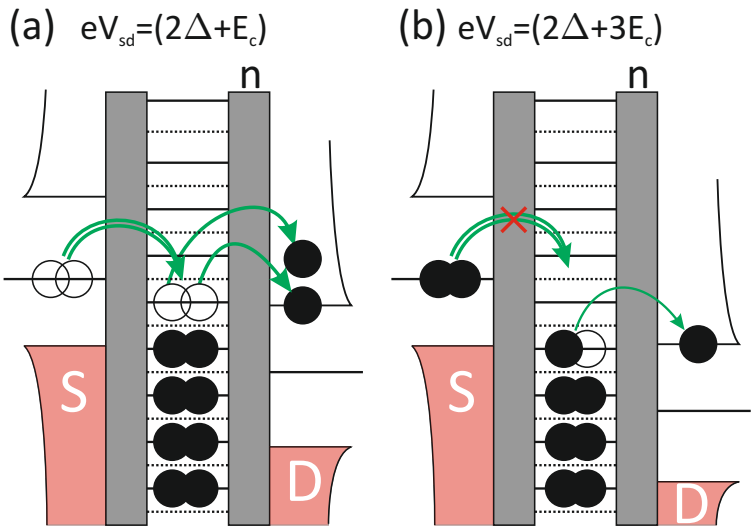

Figure 2.27: Energy diagram for the Josephson quasiparticle peak.

Another mechanism of tunnelling is via the process of Andreev reflection. For these to be observable the condition $E_c < \triangle$ must be met. If this condition is reversed the quasiparticle tunnelling thresholds are lower than the Andreev reflection thresholds, less energy is required to break a Cooper pair than to add an extra electron to the island, therefore observations will be hard to see due to a large background of quasiparticle tunnelling. If this condition is met then such features as the AQP current ridge, the AA peak, the 3e-A and 3e-AA peaks may

be observed, if the charging energy lies in the range $2\triangle/3 < E_c < \triangle$, as required for the 3e peak.

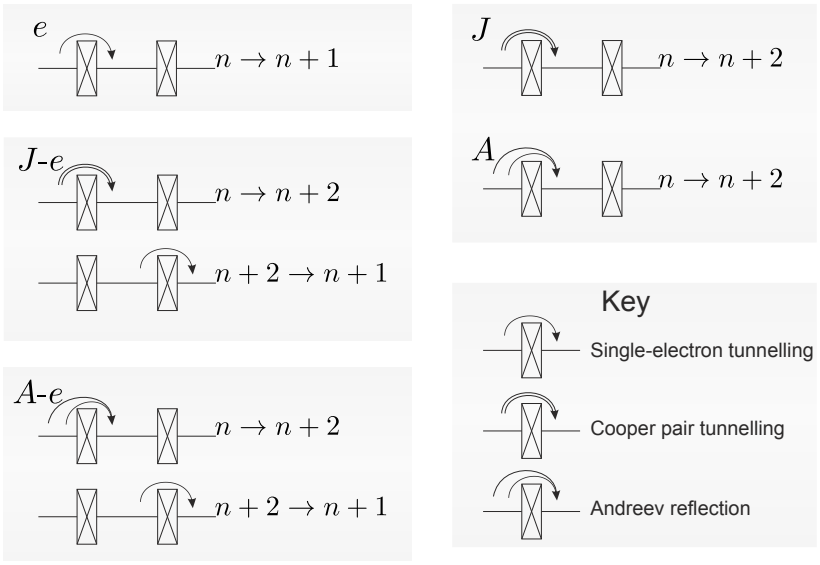

Figure 2.28: Depiction of tunnelling transition key components, these are the basic parts which make up the main tunnelling cycles and can be used as a reference for Table 2.1.

All these features are best described by breaking up the process into component parts as shown in Figure 2.28. The simplest transition is a single electron tunnelling, e. An event in which a Cooper pair tunnels in and an electron tunnels out is known as the J-e transition. Andreev reflections are where two electrons tunnel to form a Cooper pair or the opposite, A. The A-e transition is where two electrons tunnel to form a Cooper pair and one electron then escapes. These components can be put together to describe the features as shown in Table 2.1. A depiction of where the different peaks and ridges lie can be seen in the stability diagram, Figure 2.29.

Feature	Cycle
JQP	J-e, e
3e	J-e, J-e
AQP	A-e, e
3e-A	J-e, A-e
3e-AA	A-e, A-e
AA	A, A

Table 2.1: Possible tunnelling transitions for a superconducting SET.

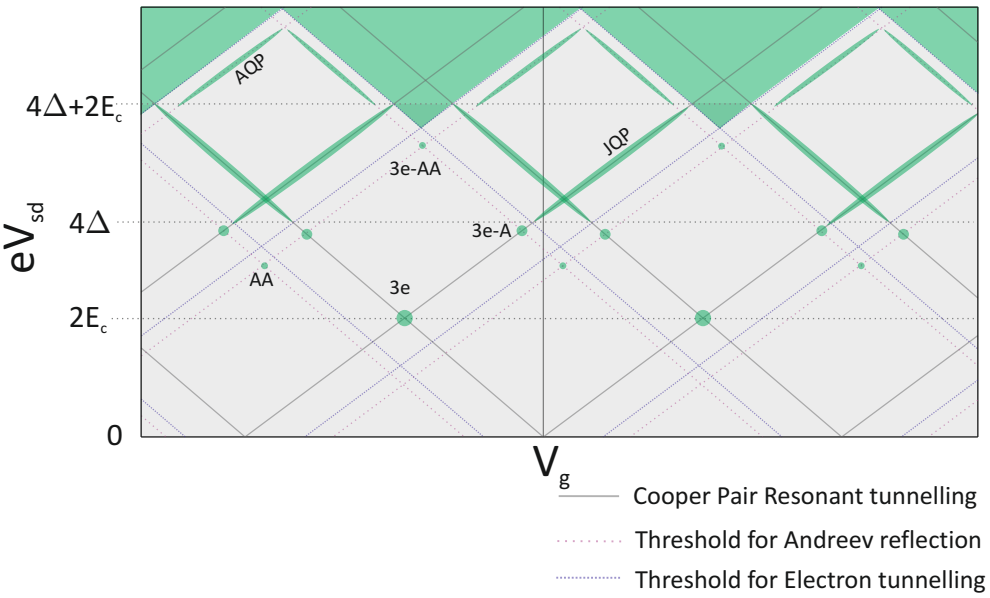

Figure 2.29: Diamond stability diagram for a superconducting single electron transistor showing positions of various conductance peaks. The grey region represents zero conductance while the green represents conductance.

2.7 Review of the Quantum Dot Detector

In this section, we now turn to a review of the development of quantum dot based terahertz detectors, bringing us to the detectors that are currently being used in this research.

2.7.1 Single Quantum Dot Detector

The first significant development of a QD THz detector came when a single quantum dot was placed in a high magnetic field. The single photon detection was achieved in the wavelength range 175-210 µm (6.0-7.1 meV) [3].

The device consisted of a relatively large semiconductor QD, approximately 700 nm, defined in a GaAs/$Al_xGa_{1-x}As$ heterostructure crystal with lithographically placed metallic split gates (see Figure 2.30). When a negative bias is applied to the gates a quantum dot is formed within the 2 dimensional electron gas (2DEG). The quantum dot has a weak coupling through tunnel barriers to the 2DEG electron reservoirs.

The device is placed in a high magnetic field, perpendicular to the direction of the plane of the 2DEG. The electron trajectories were confined to a set of concentric circles around the field lines with the cyclotron frequency $\omega_c = \frac{eB}{m^\star}$, where $m^\star$ is the effective mass. The contribution to the energy from the in-plane motion then becomes quantised in units of the cyclotron energy;

$$E = E_i + \left(N + \frac{1}{2}\right)\hbar\omega_c \tag{2.21}$$

This defines the formation of the Landau levels (LL). As the magnetic field is increased the LL separation increases [66]. The field is chosen so that the lowest orbital Landau level, LL1, is filled whilst the first excited landau level, LL2, is occupied with a small number of electrons.

At the Fermi level, LL1 and LL2 form compressible metallic regions, where the electrons are delocalised and free to move, which correspond respectively, to

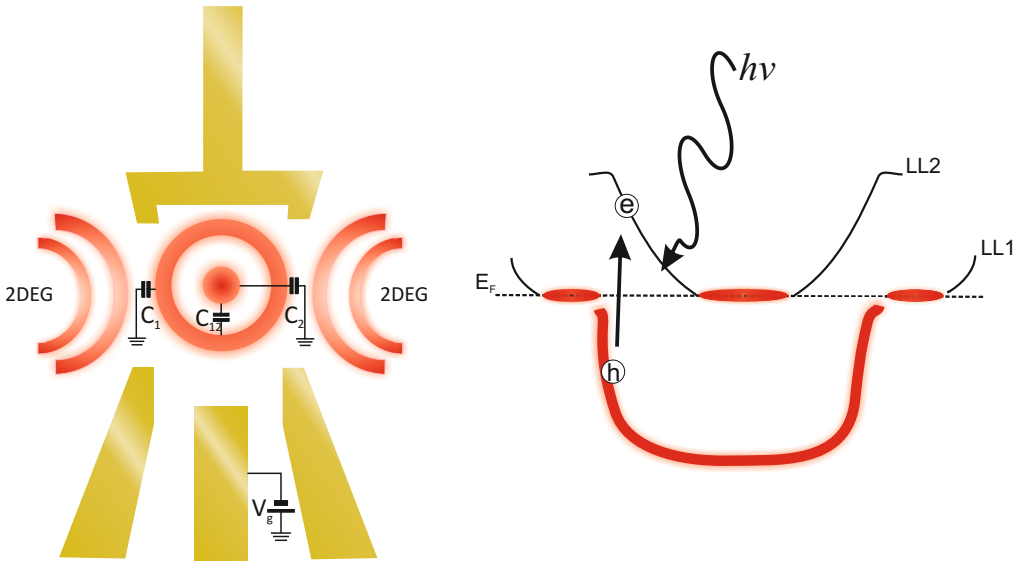

Figure 2.30: a) Diagram of the QD. The red regions indicate metallic inner core and outer ring regions formed by the lowest two Landau levels (LLs). b) Energy spectra of the LLs in the QD. When an electron–hole pair is excited within the QD by absorption of a far-infrared (FIR) photon, the excited electron (hole) rapidly falls (climbs up) to the inner core (outer ring) of the QD to polarise the QD [3].

an "outer ring" and "inner core" of the QD. The tunnelling probability between these two metallic regions is strongly suppressed by the incompressible insulating strip of static electrons that separates them. When the electrochemical potential of the outer ring, μ_1, lines up with that of the reservoirs, conductance resonance takes place because electrons can tunnel between the reservoirs and the outer ring. Although the inner core does not directly contribute to the transport, its charge strongly affects the transport by acting, in effect, like a third gate having an electrostatic coupling to the outer ring.

When a THz photon is absorbed by the QD via cyclotron resonance, an electron in an LL1 state within the insulating layer gains the energy required to move to LL2. The electron then dissipates part of the energy to the lattice and relaxes to the Fermi level into the inner core of the dot. This causes the core to be negatively charged by $-e$, causing the electrochemical potential in the vicinity of the conducting ring to change by,

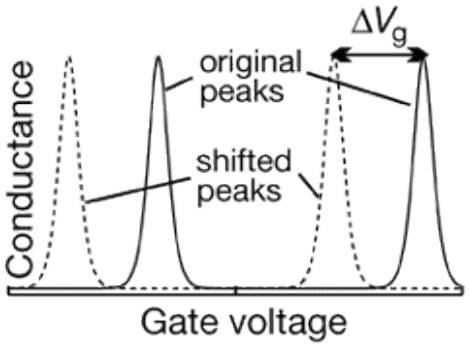

Figure 2.31: Diagram of Coulomb conduction peaks as a function of the control gate voltage V_g. The solid line represents the peaks under no illumination, and the dotted line represents a shift in the peaks because of an incident photon event on the QD [3].

$$-\triangle\mu_1 = -eC_2/(C_2C_1 + C_{12}C_1 + C_2C_{12}) \tag{2.22}$$

where C_1 and C_2 are the capacitances formed between the dot and the reservoirs for the source and drain respectively, while C_{12} is the capacitance between the inner core and outer ring. This internal electrical polarisation causes the conductance resonance peaks to shift by $-\triangle V_g \propto -\triangle\mu_1$, see Figure 2.31. As a result, conductance through the QD changes dramatically.

This, together with the fact that the excited electron in the inner core has an extremely long lifetime owing to suppression of tunnelling, makes single far-infrarared photon detection feasible. The number of photons can be counted by measuring the jumps in the tunnel conductance through the QD (see Figure 2.32).

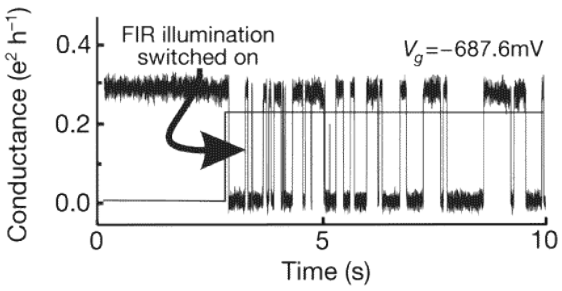

Figure 2.32: Conductance vs. time showing jumps when THz photons are absorbed by the QD [3].

In the experiments carried out by S. Komiyama et al.[3], the QD was placed in a high magnetic field, $B = 3.67$ T, where only LL1 and LL2 were occupied. The QD was calibrated, by plotting the positions of the conductance peaks as a function of the control gate voltage V_g and magnetic field B with no incident THz illumination, see Figure 2.33. As the magnetic field is raised for a given trace, electrons are transferred sequentially from the inner core to the outside ring. This is because, when the magnetic field increases, it allows more electrons to be held within each Landau level, causing the filling factor to decrease. The filling factor is the number of states per unit area in each Landau level which are equal to those originally within the range of one cyclotron energy in the 2D density of states (DOS), i.e. eB/h per LL. This is also the number of flux quanta threading a unit area, which is no coincidence since the number of different electron wave functions that can be created in each LL is equal to the number of flux quanta. When particles are put into these states, the filling factor ν is equal to the number of Landau levels filled. The quantum limit is reached when only one LL is occupied.

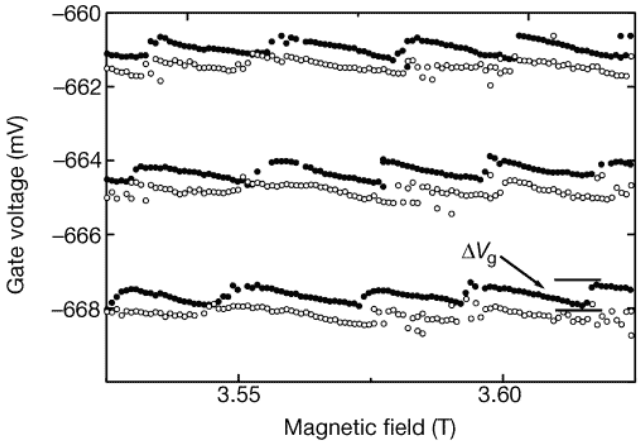

Figure 2.33: Position of the Coulomb conductance peaks in the plane of V_g vs. B. The black circles indicate a trace without incident radiation and the white circles represent a trace with incident radiation [3].

For every electron that leaves the inner core, it is positively charged by $+e$ causing μ_1 to increase by $+\triangle\mu_1$. This is the exact opposite process expected when a THz photon is absorbed during cyclotron resonance. In a plot of the position of the Coulomb conductance peaks in the plane of V_g versus B, clear jumps in the position of the peaks can be observed, $\Delta V_g = +0.6$mV for each trace [3].

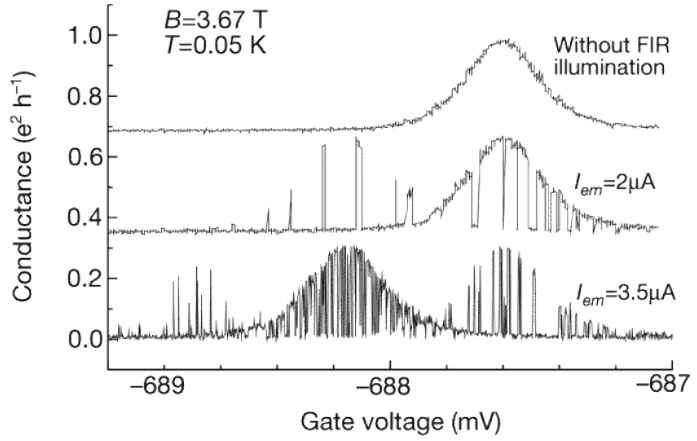

Figure 2.34: Graph showing shifts in a conductance peak under FIR illumination [3].

Figure 2.34 shows the results that focus on an individual conductance peak at $T = 0.05$ K and $B = 3.67$ T. The upper plot on the graph shows the conduction peak without any THz illumination. When a weak illumination is present, in this case I_{em} =2 µA, the trace shows that some peaks in a region shift towards the negative direction, while the original conductance peak shows regions where it is occasionally switched off. When the intensity is increased to $I_{em} = 3.5$ µA, the original conductance peak nearly vanishes apart from a few spikes. Additionally, there is a dense region of spikes in the same region as these few peaks that show up under the weak illumination. The dense region shows a distinct envelope of another resonance line centred at the expected shifted region of $\Delta V_g = +0.6$ mV. This trace also reveals further peaks at a further shifted position. Studies of this QD system, therefore reveals that the position of the first peak is independent of the THz intensity, and, integrated over time, the original peak completely disappears in conjunction with the arrival of the shifted peak. This indicates that the new conductance peak is a result of the excitation of one electron changing the chemical potential of the QD, as originally believed. The second shifted peak can now be explained as the double excitation of the QD.

The effective noise equivalent power estimated for this detector is calculated by considering the dark switching rate, which is the excitation of electrons to the higher energy level due to noise within the system, such as thermal fluctuations. The quantum efficiency of the device, is of the order of 1%. The detector is believed to have a $NEP \approx 10^{-22}$ W/Hz$^{1/2}$, which exceeds the best values of conventional detectors by a factor of 10^4 .

2.7.2 Double Dot

Another variation of this type of detector arose with the development of the lateral double quantum dot detector. Demonstrated by S. Komiyama et al. (2000) [3] this system was achieved by fabricating the two dots using a GaAs/$Al_xGa_{1-x}As$ heterostructure, which again allowed for the control of the

2DEG through negative biasing of fabricated electrostatic gates on the surface. Again, the emission of radiation at the cyclotron frequency from a high mobility 2DEG Hall bar was used as a monochromatic tunable source. The detector consisted of the two dots situated side by side, depicted in Figure 2.35. The first dot $D1$ is connected to the source and drain when the bias of the gates are below the pinch-off voltage. The electrochemical potentials of $D1$ and $D2$ are controlled respectively by the plunger, $G1$, and the pair gate, $G2$. The two dots are kept separate by the potential barrier $B12$, controlled by gate $G12$, and is set to allow tunnelling of excited electrons between the two dots. The other pair of split gates, $G3$, controlling the other side of $D2$ is biased strongly so that tunnelling from the dot is completely suppressed. The split gate $G2$ spans approximately 0.2 mm in length, acting as a planar dipole antenna that couples incident photons to $D2$.

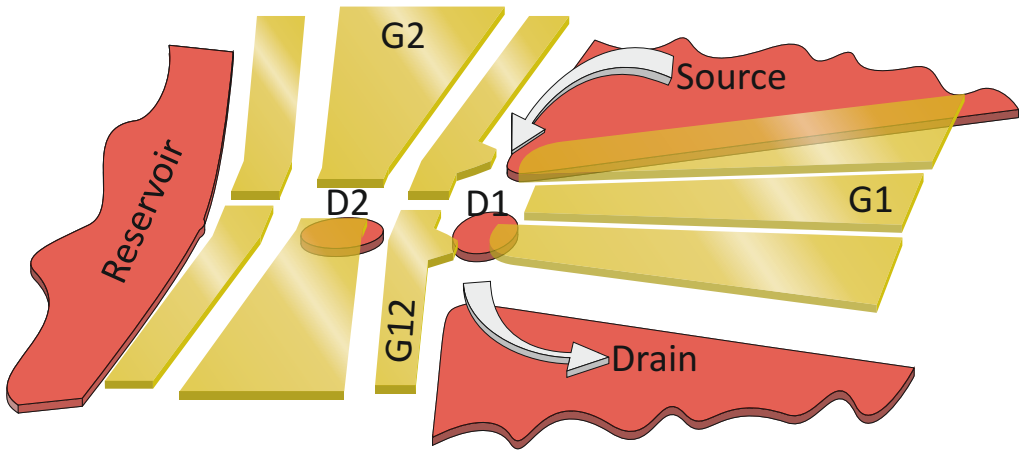

Figure 2.35: Schematic of double quantum dot detector. The red layers indicate the 2DEG, while the gold layers indicate gates on the surface.

$D1$ was constructed so it could be used to perform a similar function to the single electron transistor described in detail in Section 2.6. This means that there is a finite current transmitted from the source to the drain through $D1$ when the chemical potential, μ_1, lines up with the Fermi level of the leads, E_F. Therefore when the potential is scanned by changing the gate-bias voltage, V_{G1}, and applied

to the plunger $G1$, the conductance shows an oscillation which peaks each time $\mu_1 = E_F$. The period of oscillation ΔV depends on the capacitance between the gate and the QD.

$$\triangle V = \frac{e}{C_g} \tag{2.23}$$

where C_g is the electrostatic capacitance between $D1$ and the gate.

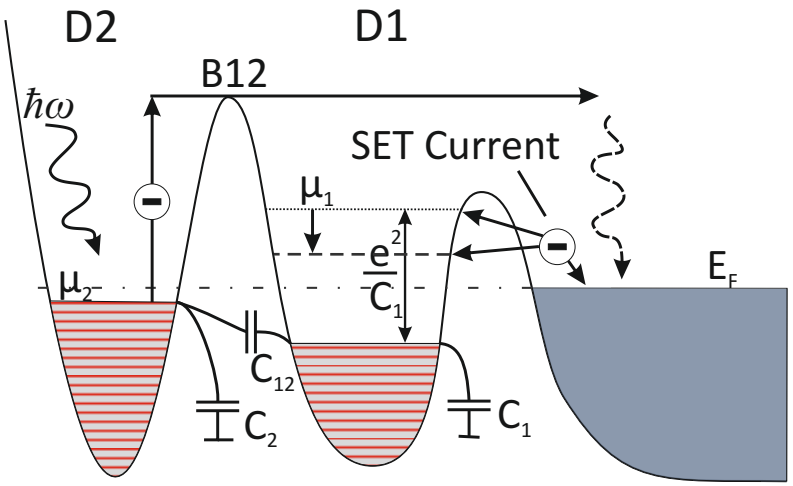

Figure 2.36: Schematic representing the excitation on the dot.

When a photon of enough energy is absorbed by $D2$, by the mechanism of Kohn-mode plasma resonance, an excited electron jumps over the potential barrier, $B12$ into $D1$ and further to the reservoir (see Figure 2.36). $D2$ becomes polarised and this changes the electrochemical potential of $D1$. As a result, the tunnelling rate of electrons through $D1$ changes, which is recorded. There is also a possibility of the excited electron tunnelling back and returning to $D2$ from $D1$ before it has gone to one of the leads, but the tunnelling probability between $D1$ and $D2$ is much smaller than that between $D1$ and the leads. The potential barrier $B12$ is set at such a level that only excited electrons can tunnel, preventing the return of the cold electron back to $D2$. The inherent ionisation of $D2$ causes μ_1 to decrease by:

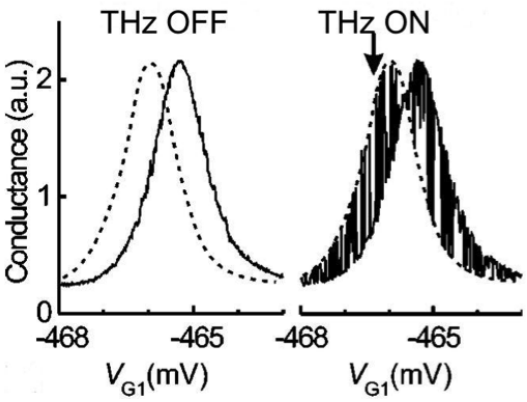

Figure 2.37: A conductance peak obtained without illumination (left-hand side panel) and under illumination (right-hand side panel) of $f \approx 500$ GHz and $P_{em} = 40$ µW. Dashed and solid lines represent states with $N_2 - 1$ and N_2 electrons, respectively, between which the dark switching takes place as $V_{G2} = V_0$ is approached.

$$\Delta\mu_1 \approx \frac{e^2 C_{12}}{C_1 C_2} \tag{2.24}$$

where C_{12} is the electrostatic capacitances between $D2$ and $D1$, and C_2 is the capacitance between D2 and the environment. The experiments performed by Komiyama et al. showed the change in the conductance peak position, which shifts towards the negative direction of V_g by some value of $\Delta\mu$.

There is a finite lifetime of the ionised state τ_L as a result of the probability of the cold electron returning to $D2$ by tunnelling. In this scheme, photon counting is achievable due to the lifetime τ_L being made longer than the instrumental time constant. In the present detection scheme, in which excited electrons escape through $D1$, the gate $G12$ that creates the barrier $B12$ requires fine adjustments, which make the operation of the sensor very unstable. Also, to build such a detector, a high quality GaAs/AlGaAs heterostructure crystal is required.

Under radiation, switching of conductance is observed, as can be seen in Figure 2.37. This can be attributed to the ionisation of $D2$. Fixing the bias voltage at one of the peaks would cause a clear switching in conductance when radiation is applied and removed. This can be considered the photoresponse of the sample.

In this type of detector there is great flexibility in the design of the devices. The size of $D1$, which operates as the SET electrometer, largely determines the operation temperature, while the size of $D2$ determines the wavelength of detected photons. The NEP estimated from this device was, $NEP \approx 10^{-21}$ W/Hz$^{1/2}$. However, the NEP is reportedly slightly higher than the previous system, because of the limitations imposed by the residual dark switching of the SET. With refinements of the design it should at least match the NEP of the previous detector. Despite the easy fabrication of this device needing only metal gates, the operation of this device requires fine adjustment of the gates. This would provide great difficulty in large systems with many detectors.

These detectors have progressed to where they are today from research and development on Langley's bolometer, together with advancements based on the current technologies at the time. The quantum dot detectors are a completely new approach to THz detection and although they are in their relatively early days, they have proven to provide the sensitivity and temporal resolution required for THz detection. The devices themselves have already had many evolutions in their design. The need for a magnetic field has been addressed, which was a requirement of the first detector with the use of a second dot.

2.7.3 QD-SET Sensor

To reduce the need for fine adjustment of the operation points of the gates, like in the double dot system, a metallic SET was incorporated directly on top of the quantum dot [67]. This design provides a strong capacitive coupling of the QD to the readout element and ensures robust operation. The devices used in this thesis were shown schematically in Figure 2.1. Due to the sensitivity of SETs (Section 2.6), they are a very responsive detection method for a change in potential on the QD, made even more sensitive with a close coupling such as ours. If the QD gate and the SET are biased correctly, a small change in the electrochemical potential of the dot is enough to cause an electron to tunnel.

2.7.4 QD-PC Sensor

A further development, which is also investigated in this thesis, was the replacement of the SET with the point contact. The fabrication of the point contact is much simpler than that of the SET, which makes QD-PC devices suitable for integration in large arrays. As described in Section 2.4, point contacts are also a sensitive detection method. Although unlike SETs they are not able to detect fractional charge, they should provide enough sensitivity for single photon detection. Its operation as a detector works by biasing the device to the point of pinch-off. The absorbtion of a photon by the QD should be enough to shift the point of pinch-off. The way this can be read out is via a lock-in technique where the source of radiation is chopped at a reference frequency, and the conductance through the mesa is measured. The two signals with the source on and off are compared, giving the photoresponse.

To get a spectral response one has to use plasma excitation of the QD. The quantum dot creates an amplification of the spectal response as seen in Section 2.5.1. The size of the dot is related to the resonant plasma frequency and therefore the frequency of radiation at which the dot will resonate. The resonance excitation of the QD can be read out either by the PC of the QD-PC detector, or by the SET of the QD-SET detector.

Chapter 4 provides a detailed account of the experiments performed using both the SET and PC based QD devices. The following chapter describes the experimental setup including its characterisation and modification.

Chapter 3

Experimental Setup and Characterisation

In this chapter we discuss and characterise the various types of terahertz radiation emitters that were investigated and used within this research. This is followed by a description of the experimental setup used for the detection of terahertz radiation using the QD sensors described in the previous chapter. Notable is the use of a cryogen free refrigerator, the first to be commissioned in this department. Its initial testing and efforts to reduce electrical noise in the system are documented.

3.1 Terahertz Emitters

In order to test our terahertz sensors, several sources of terahertz radiation were used. Specifically, these were a blackbody emitter, an IMPATT diode, a Gunn diode with multipliers and a backwave oscillator. Eventually, our aim is to perform passive terahertz imaging, without the need for an external source. However, in order to reliably test the terahertz detectors, a known source was required. A Fourier transmission spectroscopy system was also created and used to characterise a number of the sources used. Tests were also performed using a Josephson junction emitter.

3.1.1 Josephson Junction Emitter

Recent advances in compact solid state THz sources have been brought about by the demonstration of a coherent continuous wave THz radiation of sizeable power that can be extracted from intrinsic Josephson junctions in layered high temperature superconductors $Bi_2Sr_2CaCu_2O_{8+\delta}$ (BSCCO). Similarities in its operation may be drawn to that of the laser cavity — the excitation of an electromagnetic cavity resonance inside the sample generates a macroscopic coherent state in which a large number of junctions are synchronised to oscillate in phase. The emission power has also been found to be proportional to the square of the number of junctions. Work carried out by L. Ozyuzer et al. [4], have found powers of 0.5 mW at frequencies up to 0.85 THz.

Josephson junctions (JJs) naturally convert dc voltage into high frequency electromagnetic radiation following the relation $f = (2e/h)V$. Therefore a voltage of around 1 mV gives radiation of approximately 0.5 THz. Emission of radiation from a single junction is very weak; this brings about the need for a number of Josephson junctions to be emitting in phase at the same frequency to provide a useful source. The layered superconductor BSCCO naturally contains a stack of Josephson junctions. This comprises superconducting CuO_2 layers that are coupled through the intrinsic Josephson effect [68]. The way in which a large power was achieved was to synchronise the phase across the junctions by means of a standing electromagnetic wave that is formed by multiple reflections in the cavity formed by the side surfaces of the crystal. Figure 3.1 shows the I-V characteristics along with the radiation power as measured via a bolometer, which was taken whilst the bias voltage for the emitter was swept firstly up and then slowly down. Peaks in the radiation power can be clearly seen and correspond to peaks in the I-V characteristic.

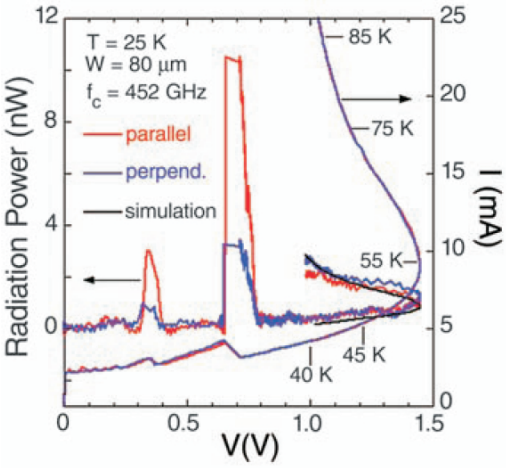

Figure 3.1: I-V characteristics and radiation power. The set up consisted of a 0.452 THz cut-off filter, which had parallel and perpendicular settings. Unpolarised thermal radiation can be seen at higher bias, a simulation of the thermal radiation is shown as a black solid line. Polarised Josephson emission can be seen to occur at 0.71 V and 0.37 V [4].

3.1.2 HTS stacked Josephson Junctions

From these recent advancements an investigation of the radiation emitted by intrinsic Josephson junctions of a high temperature superconductor (HTS) was performed. An emitter developed at Loughborough University which also uses the HTS, $Bi_2Sr_2CaCu_2O_{8+\delta}$, was studied and the radiation emitted was assessed using a QD-PC detector. This sample consists of a number of stacked Josephson junctions, the number of junctions in the stack is:

$$N = \frac{d}{s} = \frac{0.72\,\mu\text{m}}{1.56\,n\text{m}} = 460 \tag{3.1}$$

where s is the distance between layers and d the height of the stack. The area in the ab-plane of the stack (see Figure 3.2):

$$A = (16.5 \times 12.4)\,\mu\text{m}^2 = 240.6\,\mu\text{m}^2 \tag{3.2}$$

the critical current density:

$$J_c(0\ \mathrm{K}) \approx 1000\,\mathrm{A/cm^2} \tag{3.3}$$

The sample is attached to the wave guide and the emitted light is fed down to the detector. The junction is biased to voltage V, see Figure 3.2. According to the Josephson relation, the junction should produce radiation with frequency,

$$f = \frac{2eV}{h} \tag{3.4}$$

to make the jump to a state where it begins to emit light. There is a specific working point at which there will be a particular electromagnetic cavity resonance inside the stack generating a macroscopic coherence state, so that a large number of junctions are synchronised to oscillate in phase. To get to this region the bias voltage for the HTS must first be swept up to a high bias, in this case 1.8 V then slowly swept back. It is during this back sweep where the junctions should emit.

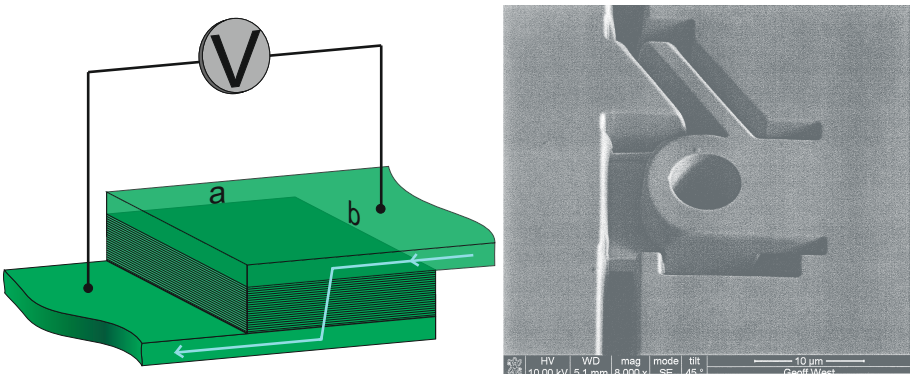

Figure 3.2: Left: Josephson junction emitter, depicting the path of current passing across the stacked tunnel junctions. Right: An SEM image of the JJ emitter.

The QD-PC device which was set up at the end of the light pipe had both gates biased to what is assumed to be a sensitive region and as the HTS bias is decreased, the current and voltage across the HTS junctions is measured along with the corresponding photoresponse with respect to the HTS voltage. This can be seen in Figure 3.3. No clear photoresponse can be seen as there are no peaks in the photoresponse level. This could be for a number of reasons, either

the junctions were not synchronising therefore any radiation emitted would be almost nonimal to our detector, or the HTS did not manage to emit any radiation. Another possibility is that our detector could not be tuned to the most responsive region. Without another known source being added to the system, it was not possible to adjust the quantum dot and PC gates to the most responsive bias. Consequently, the JJ emitters were not used to characterise the QD detectors.

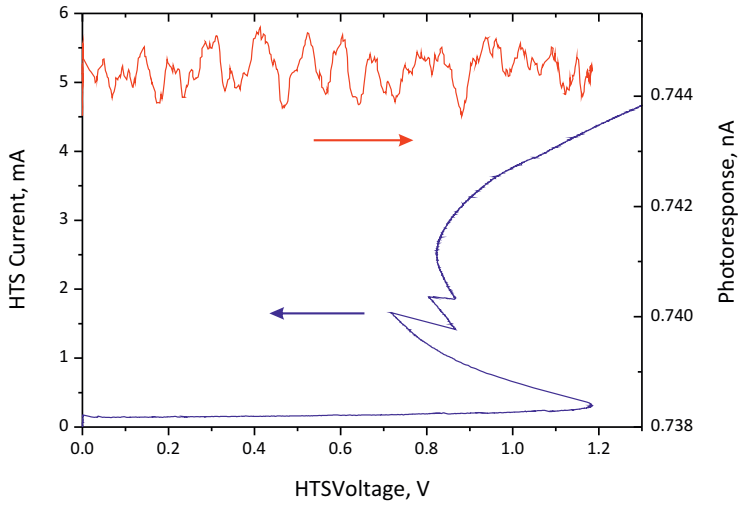

Figure 3.3: I-V characteristics and photoresponse of the HTS emitter.

3.1.3 IMPATT Diode, Gunn Diode and BWO

The three predominant terahertz sources used in the experiments described in this thesis are the IMPATT (IMPact ionisation Avalanche Transit Time) diode, Gunn Diode and BWO (Backward Wave Oscillator).

The IMPATT diode consists of a reverse biased avalanching p-n junction. The diode used here has a stated photon emission frequency of approximately 100 GHz and a typical power range of between 50 - 200 mW. A Gunn diode is unlike other semiconductor diodes in that it does not use a p-n junction but is instead fabricated from a single piece of n-type semiconductor, where the thickness of the central active region is one of the main determining factors of the emitted frequency. The Gunn diode used in this thesis was used together with a frequency

doubler, giving an output range of between 165-195 GHz [69]. The BWO is a device consisting of an electron beam that interacts with a slow-wave structure that is accelerated via anodes and cathodes. It has a uniform magnetic field along the axes which holds the electrons in a parallel beam. The greatest characteristic of a BWO is its electrical tunability over a wide range of frequencies, achieved by adjusting the velocity of the electrons via the operating voltage. The measured frequency-voltage dependence of our BWO is, $f = 0.0734V + 299.5$, as taken from Figure 3.4. The frequency of the output was measured using a home built Fourier transmission spectroscopy system, which is described in the following section.

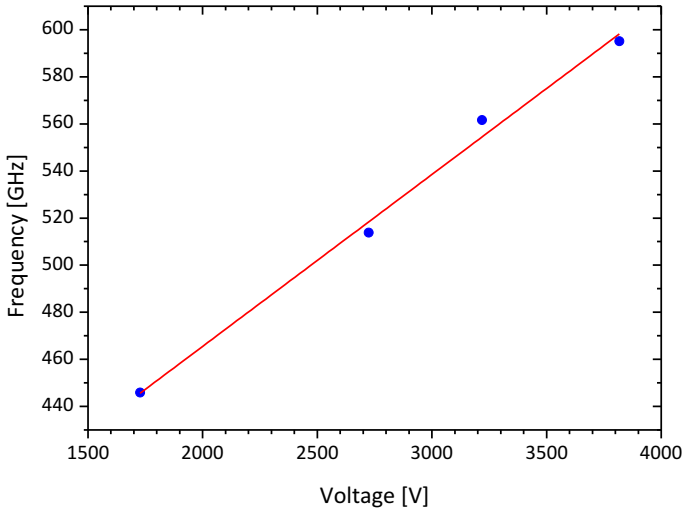

Figure 3.4: Frequency dependence in relation to voltage applied to the BWO as measured using the Fourier transmission spectroscopy system.

3.1.4 Fourier Transmission Spectroscopy System (FTS)

Traditionally, spectrometers were of the dispersive type [70]. In a dispersive spectrometer, the individual frequencies of energy (wavenumbers) emitted from the infrared source are detected sequentially. This is achieved by the use of either a prism or grating [71]. In an FTS spectrometer, all the wavenumbers of light are observed at the same time. FTS is a non-destructive method of analysis, which requires no external calibration. It is more sensitive than dispersive methods as it can detect frequencies over a wider wavelength range and at much higher

resolutions [70].

The FTS system, consists of a few key components, see Figure 3.5. These are: a source of radiation, a beam splitter and two mirrors, one is fixed in place and the other has a freedom of linear movement. The beam splitter, which is set at 45 degrees to both mirrors, allows half the beam to be transmitted through it and half to be reflected. One of the beams reflects off the fixed mirror, and the other beam reflects off the moveable mirror. Thus, 50% of the radiation from the light source is transmitted to the moveable mirror and 50% of the radiation is reflected to the fixed mirror [72, 73].

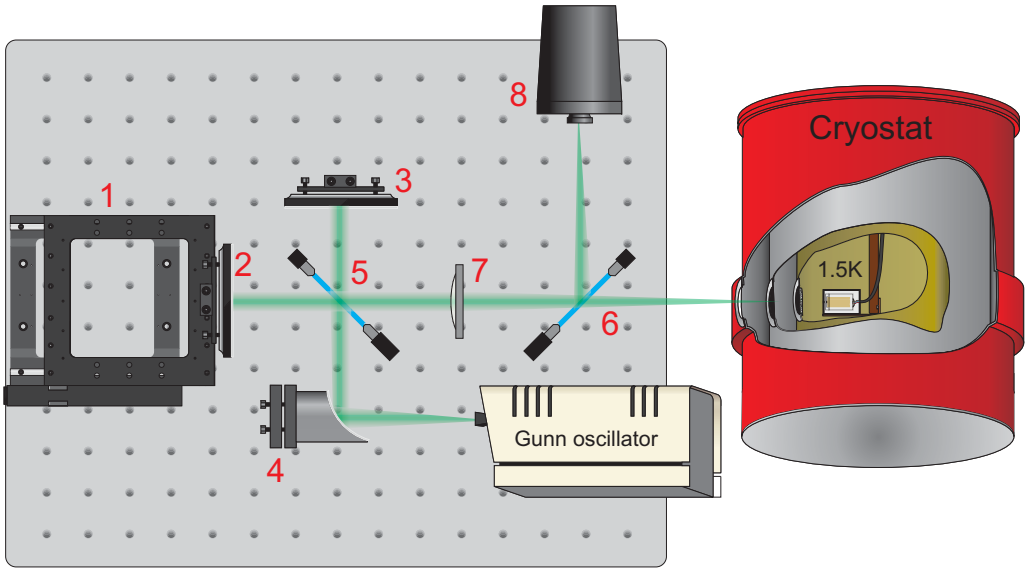

Figure 3.5: FTS system and its integration with the fridge and Gunn oscillator. (1) Movable stage, (2) Mirror mounted to movable stage, (3) Fixed mirror, (4) Concave mirror, (5&6) Mylar beam Splitters, (7) Focussing lens, (8) Pyrodetector.

The radiation beam from both mirrors is then reflected back to the beam splitter where they recombine. Once again half of the radiation is reflected and half is transmitted, so that half of the radiation is sent out as an output signal. The two beams, one of which travels a fixed length, and the other which has a variable length, 'interferes' with one another. The resulting signal is called an

interferogram. To interpret the interferogram signal one has to perform Fourier transformation of the recorded signal.

If we consider a wave with a single frequency its two beams of radiation will emanate from the same source, however these beams will travel over different paths due to the position of the moveable mirror. The field at the detector will be determined by the optical path difference (OPD), denoted by $\triangle x = x_2 - x_1$. The phase difference is given by:

$$\triangle\phi = \frac{2\pi}{\lambda}\triangle x = k\triangle x \tag{3.5}$$

where k is the wavenumber. For constructive interference the condition that must be met is:

$$\triangle\phi = 2m\pi, \quad m = 0, \pm1, \pm2, \pm3, ... \tag{3.6}$$

The condition for destructive interference is:

$$\triangle\phi = \pm(2m+1)\pi, \quad m = 0, 1, 2, 3, ... \tag{3.7}$$

We assembled the FTS system, as shown in Figure 3.5, and measured spectra of the different sources described in Section 3.1.3. The measured frequency and relative powers of each source can clearly be seen in Figure 3.6.

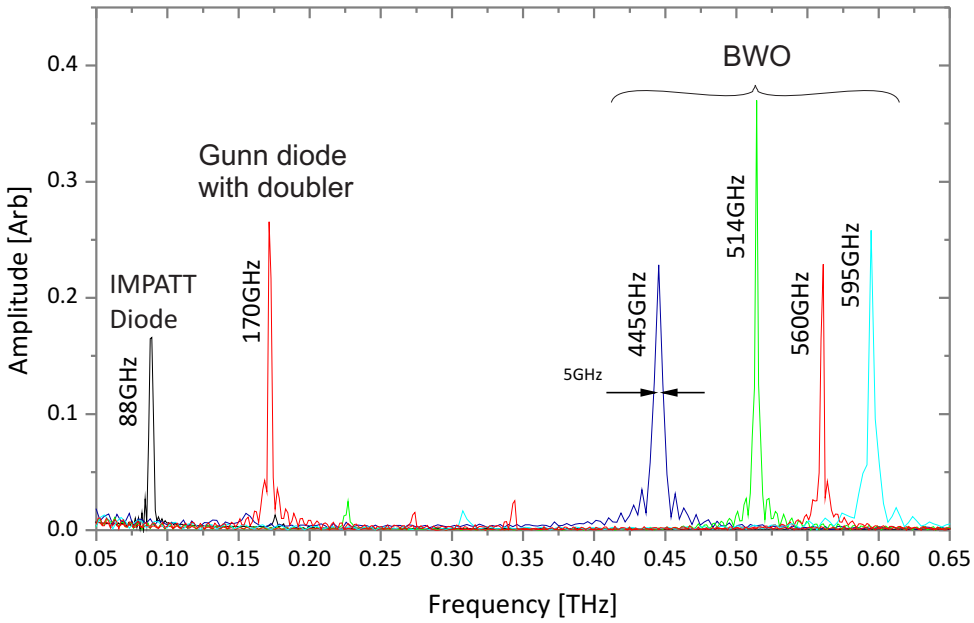

Figure 3.6: Spectroscopy of different sources measured using the FTS system showing their measured frequencies and relative powers. The BWO is useful for its tunability over a wide range.

3.2 The Cryogen Free Refrigerator (VeriCold)

For the experiments in this thesis we used a three stage cryogen free pulse tube refrigerator [74] (see Figure 3.7). The first two pulse tube stages achieve temperatures of approximately 70 K and 4 K, and the final stage with demagnetisation can achieve temperatures down to approximately 300 mK. The refrigerator was modified to include optical windows allowing the transmission of THz radiation into the fridge whilst filtering out other frequencies from the room temperature environment.

The choice to use a cryogen free refrigerator was to allow for a wider variety of applications due to the easy implementation of systems that do not require a consistent supply of cryogenic liquids. This would be an improvement on existing traditional systems that require cooling via a cryogenic Dewar, which require constant refills of liquid helium for its operation. These cryogenic systems bring

about impracticalities such as higher costs, maintenance and safety issues for uses in real world environments, for example in airport security scanning. Furthermore, due to the nature of the cryogen free refrigerator, the installation of optical windows for our experiments was relatively simple.

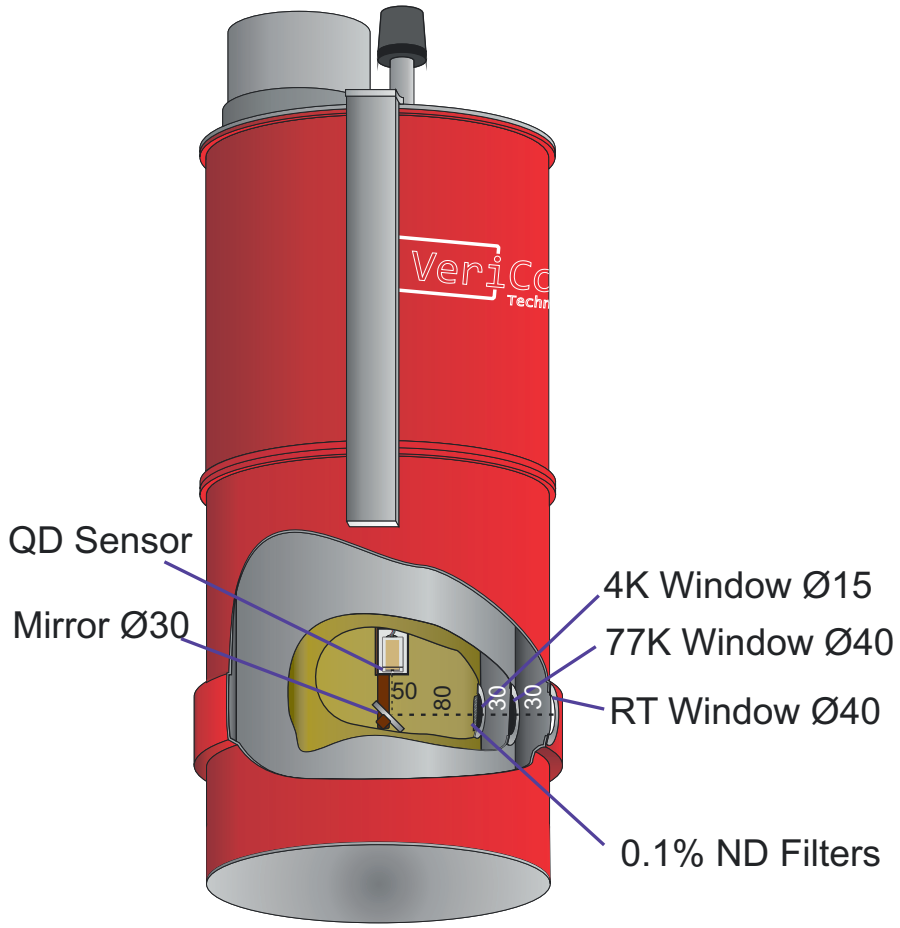

Figure 3.7: Schematic of VeriCold fridge with screens. Red layer is the outside screen at room temperature, silver layer is the 77 K screen, gold layer is the 4 K screen. The optical windows are also shown with dimensions in mm.

The basic cooling stages of the fridge can be described as follows. When the fridge is started, the first two stages of the fridge (77 K stage and 4 K stage) are cooled to their base temperatures of ~ 70 K and ~ 3 K respectively. This initial refrigeration is performed by a pulse tube cooler, which relies on the cooling that occurs as helium exchange gas expands. The sample stage is cooled further by adiabatic demagnetisation refrigeration (ADR). The sample stage is suspended

above the 4 K stage with teflon wires. Thermal contact between these stages is controlled via an electronically operated heat switch (see Figure 3.8). The sample stage is thermally coupled to the GGG crystal ($Gd_3Ga_5O_{12}$). To cool the sample stage by ADR, the current in the ADR magnet (which is heat sunk at 4 K) is slowly increased. The current is ramped slowly so as not to quench the magnet. This aligns the magnetic moments within the crystal causing its temperature to rise. This heat is removed from the crystal via a closed heat switch to the 4 K stage. When the current reaches its maximum of 36 A and the sample stage and 4 K stage are both at their base temperatures, the heat switch is opened, isolating the sample stage from the rest of the system. The magnetic field can now be ramped down resulting in adiabatic cooling of the crystal and thus the sample stage.

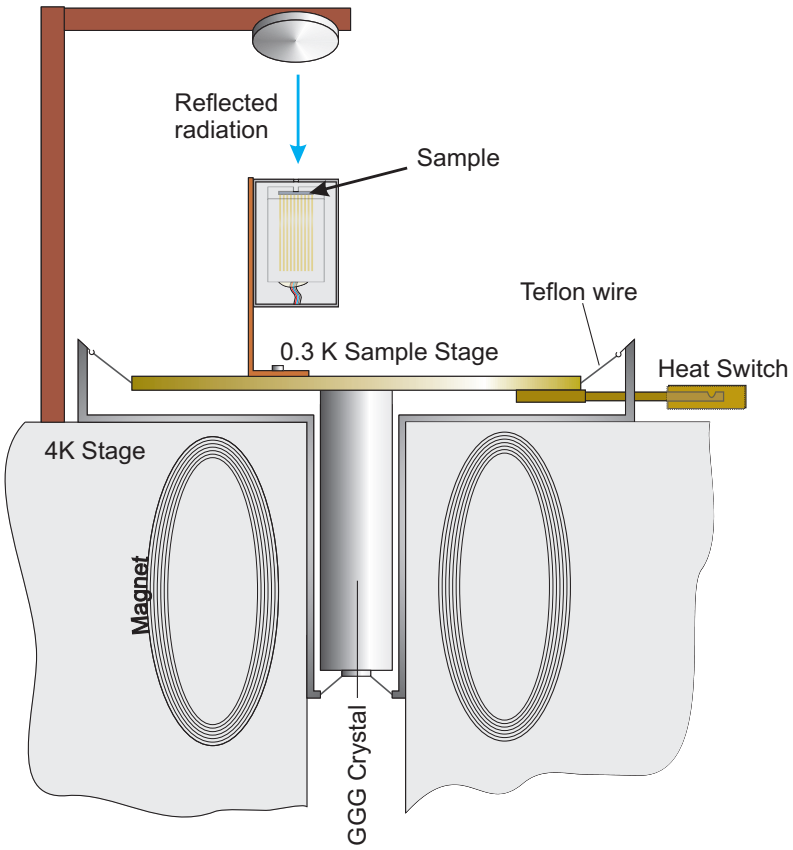

Figure 3.8: Schematic of the demagnetisation stage demonstrating thermal isolation from the 4 K stage. The electronic heat switch gate allows a controllable thermal connection between the 0.3 K and 4 K stages.

3.2.1 Performance of the VeriCold fridge with Optical Windows

The fridge consists of three thermal screens isolating the 0.3 K stage from room temperature: the room temperature screen, the 77 K screen and the 4 K screen, see Figure 3.7. There are windows designed at each layer, which allow external THz radiation to be delivered into the sample area while other frequencies are filtered out. Figure 3.9 is a photograph of the external window. However, these windows have a potential to affect the cooling performance of the fridge. Twenty eight experimental and three service lines were connected to the sample stage, which bring further unwanted heat to the stage. We perform experiments on the cooling down parameters of the fridge by installing one by one, the windows supplied by IMEP-LAHC [75]. Two sets of windows were supplied for the 77 K and 4 K screens. Figure 3.9 shows the supplied THz transmission characteristics of each set of windows. The room temperature window, constructed from Teflon, was preinstalled in the room temperature shell. Windows for the 77 K stage are made of black polyethylene on a Si wafer and adhered via General Electric 7031 varnish.

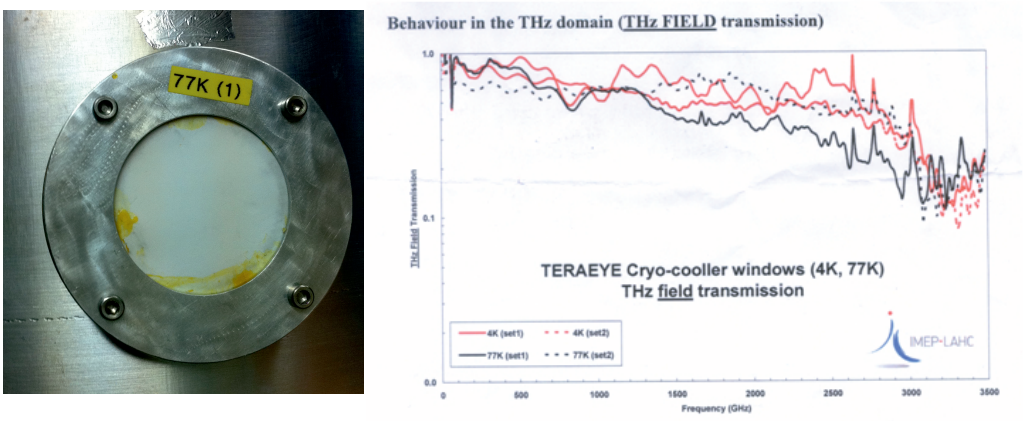

Figure 3.9: The supplied THz transmission spectrum of both sets of windows. The 4 K window data is shown in red and the 77 K is shown in black.

The temperature of the fridge can be monitored with three resistance thermometers thermally heat sunk to each stage. For a comparitive test, the cooling power of the cryopumps only, from room temperature to 4 K was measured. Initially, the cooling power was measured with blanking plates mounted instead of the windows on each stage. Following this, the cooling power was remeasured using the window combinations given in Table 3.1 to see the effect of the windows. The base temperature of the 4 K stage was reached in approximately 24 hours from room temperature for these tests, as can be seen in Figure 3.10.

Run	77 K window	4 K window
1	Blank	Blank
2	Set 1	Blank
3	Set 2	Blank
4	Set 2	Set 1

Table 3.1: Combinations of windows used for testing the cooling performance of the fridge.

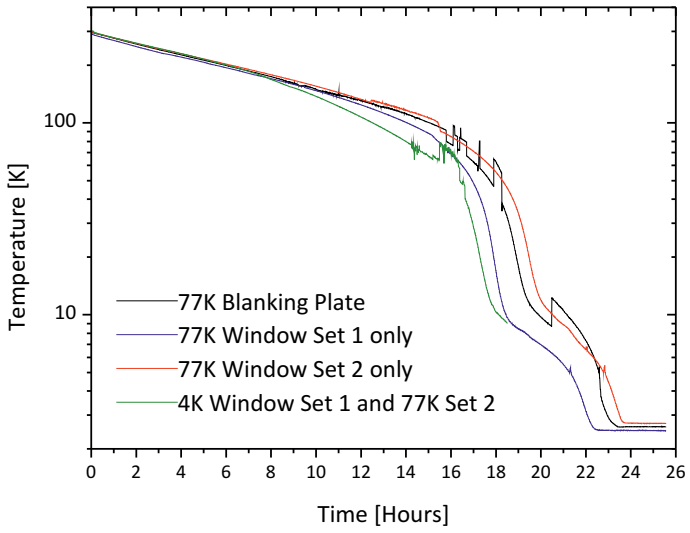

Figure 3.10: The cooldown cycle with different window combinations: with the blanking plates on (black), at the 77 K stage: Set 1 (blue) and Set 2 (red), and with the 4 K window also in place (green).

There appears to be a variation of ±1 hour in cool down time between the different setups, however the base temperature was not affected. It can also be

seen in Figure 3.10 that there are jumps in the 4 K thermometer when cooled with 77 K windows "Set 1" & "Set 2". This is most likely the result of an inconsistent thermal contact between the 4 K stage and the sample stage during cool down due to differential thermal contraction.

The holding time of the sample stage was also measured. This is a measure of how long the sample stage can remain below 1 K after cooling to 300 mK through ADR and is shown in Figure 3.11. With blanking plates mounted, the holding time is much greater than 100 hours. When a window to the 4 K stage was added, the holding time decreased to $\sim$ 30 hours. However this holding time was still much longer than the time required to perform the experiments proposed for this setup.

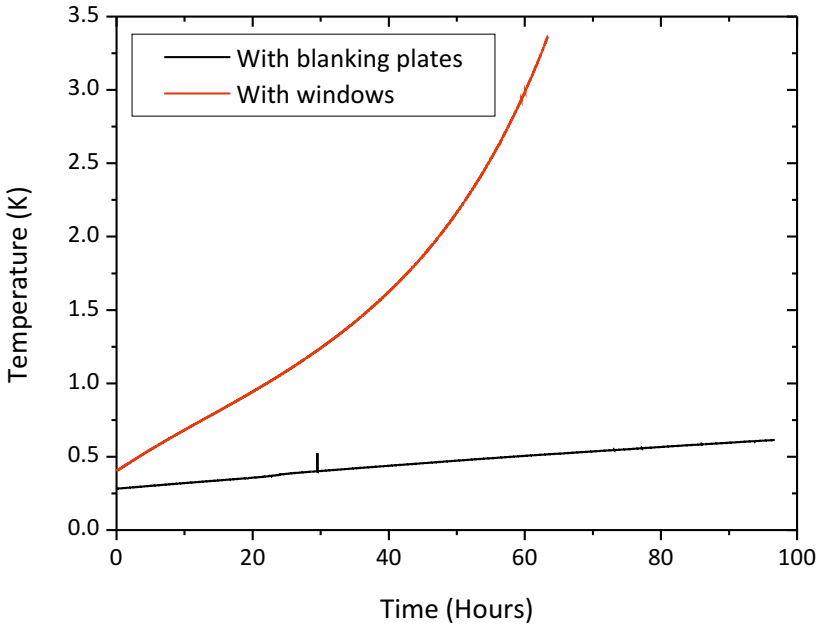

Figure 3.11: The effect of holding time of the fridge with 77 K and 4 K windows. The black line is with the blanking plates installed instead of the windows, the red line is with the two windows installed.

3.3 Schematics of Experimental Setup

Figure 3.12 shows the electronic instrumental setup used throughout this thesis, to take measurements of the sample. The optical bench used for imaging as described in Section 5.3 has been omitted for clarity. Table 3.2 is an explanation of each of the instruments shown.

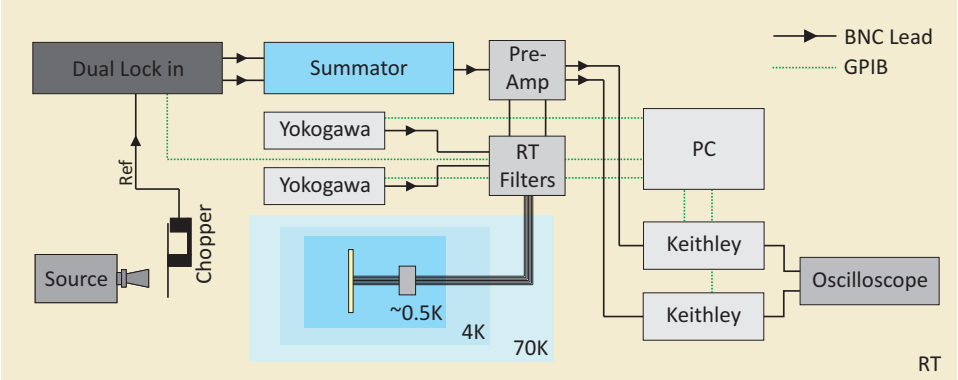

Figure 3.12: Experimental set up showing the electronic instruments used. The optical bench has been omitted for clarity.

Device	Description
Summator	Combines two inputs, in this case it adds together an AC and DC source both provided by the dual lock-in.
Yokogowa PS	The Yokogowa power supplies provide the voltage biases for the gates. These can either be manually controlled or controlled via GPIB inputs using Labview.
Yokogowa FG	The Yokogowa frequency generator can provide a variety of signals and in this instance is used as the source for the emitter. A typical signal would be a square wave signal with an offset bias of half the amplitude, providing a top hat pulse sequence with tunable frequency.
Keithley Multimeter	Used to measure the output signals such as V and I from the lock-in.
Oscilloscope	Provides real time monotoring of the signal.
Pre-Amp	Provides amplification of the signal.
Dual lock-in	A lock-in amplifier can reduce a large amount of frequency dependent noise on a signal, such as flicker noise. However, it is therefore unable to reduce frequency independent noise, such as white noise on a signal from such things as thermal impedance, by comparing the input signal to a reference channel. The lock-in provides an AC bias current which is sent to the summator.
RT filters	The room temperature filters used are standard π-filters placed on every line for filtering AC signals.

Table 3.2: Explanation of instruments shown in the schematic of Figure 3.12.

3.4 Noise Reduction

The reduction of noise in a system is fundamental in any experimental setup. Due to the sensitivity of SETs they are greatly affected by noise. Conversely, this provides a great tool for detecting noise in the system. Figure 3.13 shows the I-V characteristics of a typical measured SET. It differs from the ideal I-V of SETs (see Figure 2.16) as it shows a smoothing of the curve at the ends of the plateaus, and as all scans were performed below the superconducting transition temperature for aluminium, some greater features should be seen as described in Section 2.6.8. This smoothing could be caused by the noise in the measurement system, including vibrations of the cryo-free refrigerator. We rule out noise resulting from the mechanical vibration of the cryo-free refrigerator as Figure 3.13 shows a negligible difference in the two I-Vs measured with the compressor on and off.

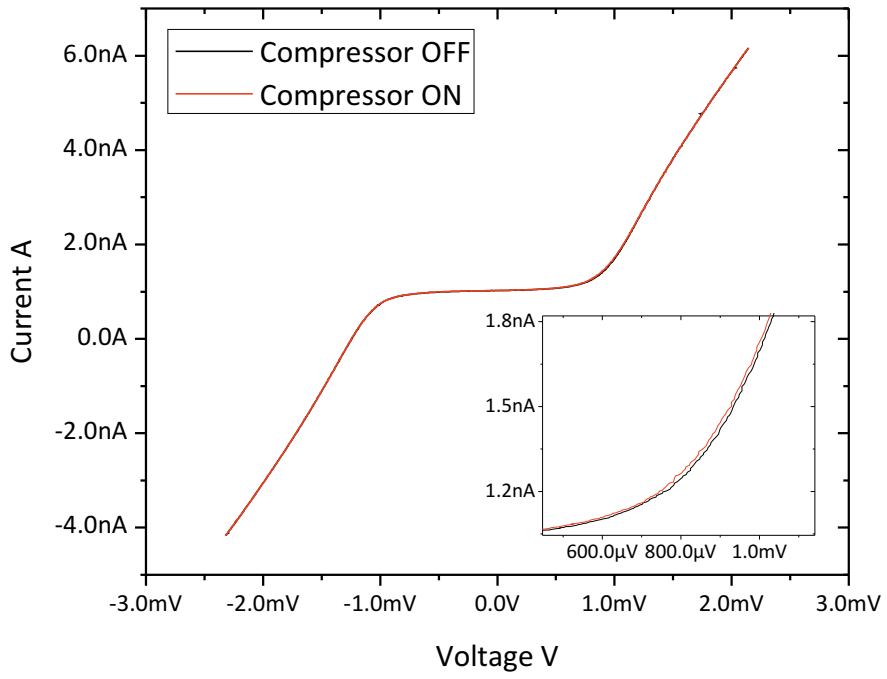

Figure 3.13: I-V characteristic of the aluminum SET. The I-V characteristic is not sensitive to mechanical vibration of the cryo-free refrigerator. Insert shows a close-up showing negligible difference between the two data sets.

The next likely source of noise is the high frequency electromagnetic noise coming from the leads, which extends to room temperature. For the I-V curve in Figure 3.13 there were only RC filters connected to each of the signal lines at room temperature. Two types of low temperature filters were investigated in order to suppress this noise.

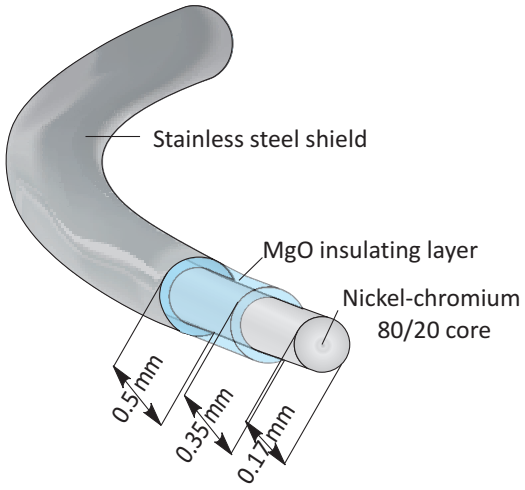

Figure 3.14: Schematic of Thermocoax filter showing the stainless steel shielding, insulating MgO layer and NiCr core.

The Thermocoax filter is a 30 cm long Thermocoax cable of 0.5 mm diameter (see Figure 3.14). These were installed on each of the signal lines and thermally coupled to the 4 K stage.

Figure 3.16 shows a distinct improvement in the I-V measured with the installation of the Thermocoax wires. The measured I-V curve sharpens and almost starts to develop Josephson quasiparticle peaks (JQPs), which were not observed when unfiltered lines were used (see inset in Figure 3.16).

The second type of filters tested were metal powder filters coupled to π-filters [76], as shown in Figure 3.15. The general principle of metal powder filters is the noise attenuation due to dissipation of high frequency currents induced in the metal grains. Due to the powder having such a large surface area, there is significant damping occurring from the skin effect. There are many ways to build metal powder filters. The simplest method is to place the wire in a box of

loose metal powder. This method can be difficult to realise as it can cause gas contamination of the cryo system, as the large surface area of the powder can absorb a large amount of gas, and would result in substantial degassing. Another approach is to mix the powder with an epoxy such as Stycast 1266, which was the method adopted here. This can be used to create a much more rigid structure, without the risk of gas contamination in the system. A disadvantage of this method is a slight reduction in attenuation.

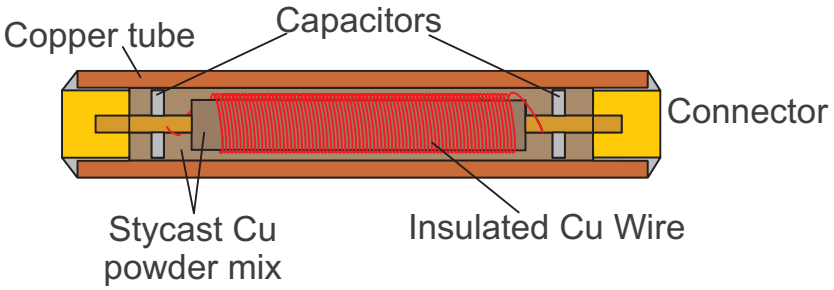

Figure 3.15: Schematic of Cu powder filter.

Figure 3.16, shows a comparison of all filtering methods used. As seen the best filtering effect was achieved by using Cu powder filters. Also the appearance of, either the $3e$ peak or Josephson quasiparticle peak, can be seen in the IV curve measured with Cu powder filters. These features are the result of the superconducting effects coming into play at these temperatures (see Section 2.6.8).

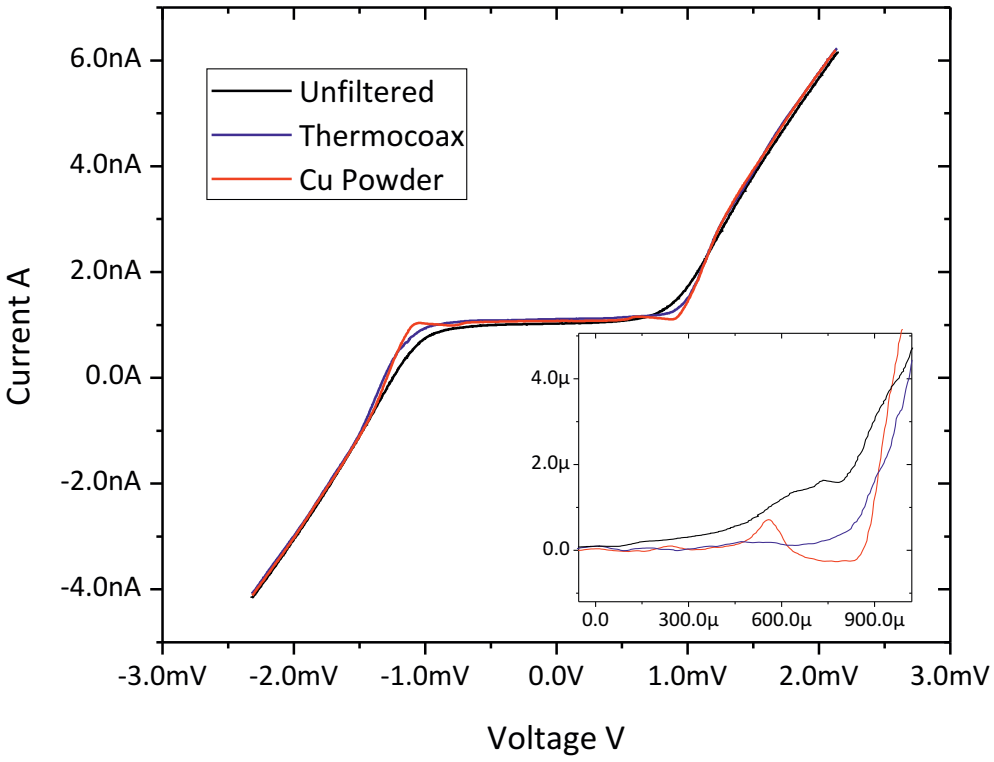

Figure 3.16: Comparison of SET I-V characteristics between unfiltered, Thermocoax and Cu powder filters. Inset shows a close-up of the differential of the region of interest, showing a distinct improvement with the Cu powder filters and the appearance of new features.

Chapter 4

Results

This chapter is an account of the measurements performed using the two types of QD based terahertz sensors: the QD-SET and the QD-PC. Later in Figure 4.1 it is shown that we have devices with both QD-SET and QD-PC sensors fabricated next to each other. This allows a direct comparison of the readout method as the same QD is probed by either the SET or PC. Both types of sensors are first characterised before measurements in the dark and under illumination are compared. The emitter power dependence of the QD-PC photoresponse is discussed. Finally, a first attempt at detecting terahertz radiation using an array of QD-PC sensors is documented.

4.1 QD-SET

I start with the experiments with the QD-SET devices. Here, the charge state of the QD is probed by a superconducting aluminium SET.

4.1.1 Initial sample testing

The layout of an experimental sample (T40) is shown in Figure 4.1. There are five devices on each sample: four QD-PC devices, one QD-SET device with a cross gate, and four QD-SET devices with QD type gates. When operating with the experimental sample, precautions should be taken to avoid damage to the

devices through electrical discharge.

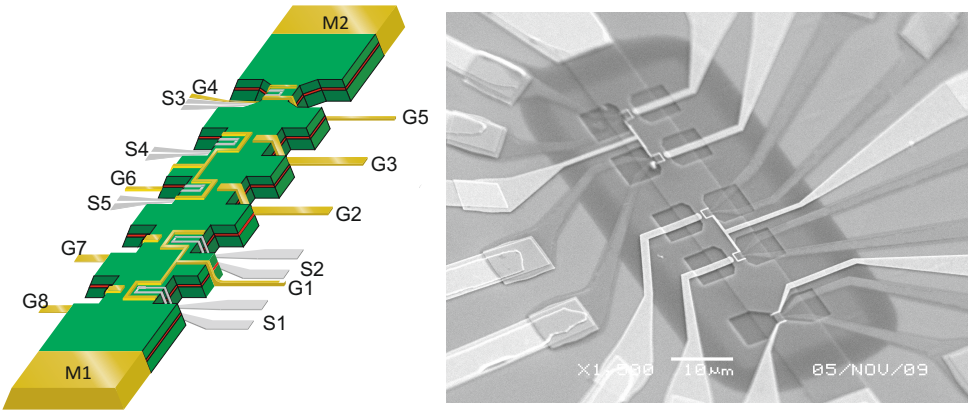

Figure 4.1: Left: Schematic of sample T40 with the contacts to each device labelled. From front to back, the devices are: four QD-SET devices, where the QD is formed by biasing G1 and G6 (S1, S2, S4, S5) and a device where the QD is formed by biasing two cross gates, G4 and G5 (S3). This design also allows the study of QD-PC detectors, where PCs are formed by the combination of gates G1-G8, G1-G7, G6-G2, G6-G3. Right: SEM picture of the sample.

Once a sample is loaded into the fridge and cooled, it must first be checked for its operation. One of the simplest tests for this is a resistance check. Typically SETs should have a resistance of a few hundred kΩ, and so a clear sign of a broken SET is an infinite resistance. These tests are performed at different temperatures whilst cooling. Table 4.1 shows the resistance measurements taken of Sample T40 (the 5 SETs and the mesa) during a cooldown.

T40	Temp	S1	S2	S3	S4	S5	mesa
Resistance [$k\Omega$]	3 K	∞	205	∞	∞	155	4.3
	0.4 K	∞	226	∞	∞	178	4.98
	0.36 K	∞	232	∞	∞	338	4.58

Table 4.1: Table of resistances of the five SETs and through the mesa, taken for sample T40 during cooldown.

It can be seen that only two SETs, S2 and S5, survived installation and cooling. Both these SETs are a part of a QD-SET gate device. Unfortunately the only cross gate device, S3 was unusable as it had an infinite resistance. This can occur for a number of reasons. One possibility is a lifting of the wire bonds during the

cooldown procedure as a result of differential thermal contraction. This was improved by using double wire bonds on connections. Another possible fault could occur during the fabrication of the SETs. The fabrication process and techniques have vastly improved throughout this work as an increased number of successful SETs have been measured during initial room temperature measurements as well as there being a noticeable improvement in quality upon visual inspection. Believed to be the most common fault is electrostatic discharge as this can be enough to blow an SET. Earthing of the cryogen free fridge and individuals during the loading procedure has improved the number of successful SETs.

4.1.2 Characterisation of the QD-SET sensor

We start with the characterisation of the SET. The stability diagram of the SETs was measured by taking Coulomb blockade oscillations at different dc biases at T=0.38 K. This creates a feature rich intensity map referred to as a diamond graph, which is shown in Figure 4.2 for SET 2.

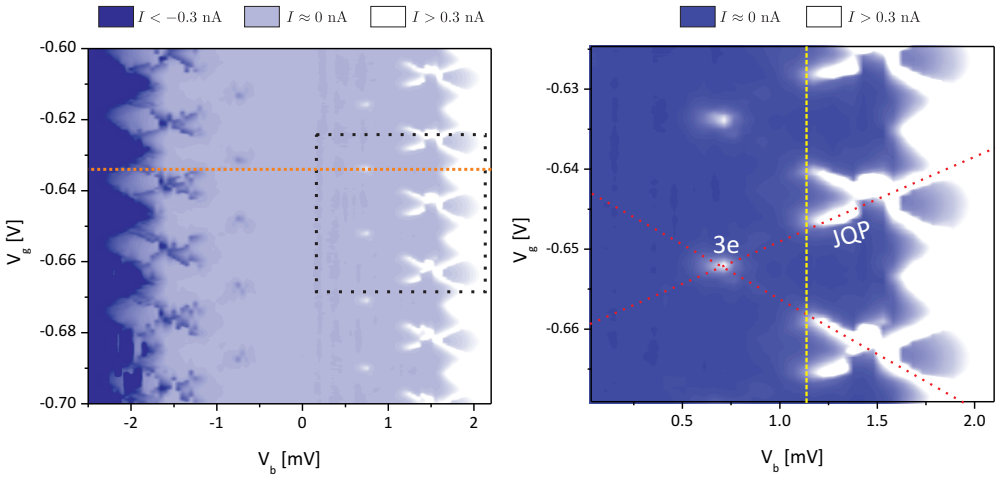

Figure 4.2: Left: Diamond graph of SET 2 in the superconducting state (T = 0.38 K) showing an intensity map of SET current as a function of bias voltage V_b and QD gate voltage V_g. The orange line in the left figure shows the position of the I-V slice shown in Figure 4.3. Right: A close up of the dotted square region from the left graph. The dotted red lines depict the diamond structure and intersect at the $3e$ peak. The dashed yellow line depicts the beginning of the JQP ridge.

A close up of the black dotted square region is shown in the right of Figure 4.2, chosen to emphasise the peaks and highlight the diamond structure formed by the JQP, with the 3e peak at the apex. The presence of these features indicates that the SET is operational and superconducting. Also, the filtering described in Section 3.4 successfully provides a low level of noise in the system, such that these features can be observed.

The I-V characterisic of the SET taken at a particular gate voltage is shown in Figure 4.3. The boundary at which the JQP ridge starts, gives the value $4\triangle$. From Figure 4.3 we find a value of $4\triangle = 1.152$ meV. In units of $k_B T_c$ this gives the superconducting gap for aluminium $\triangle = 2.783\ k_B T_c$, which is close to that measured by other groups $\triangle = 3.3\ k_B T_c$ [77].

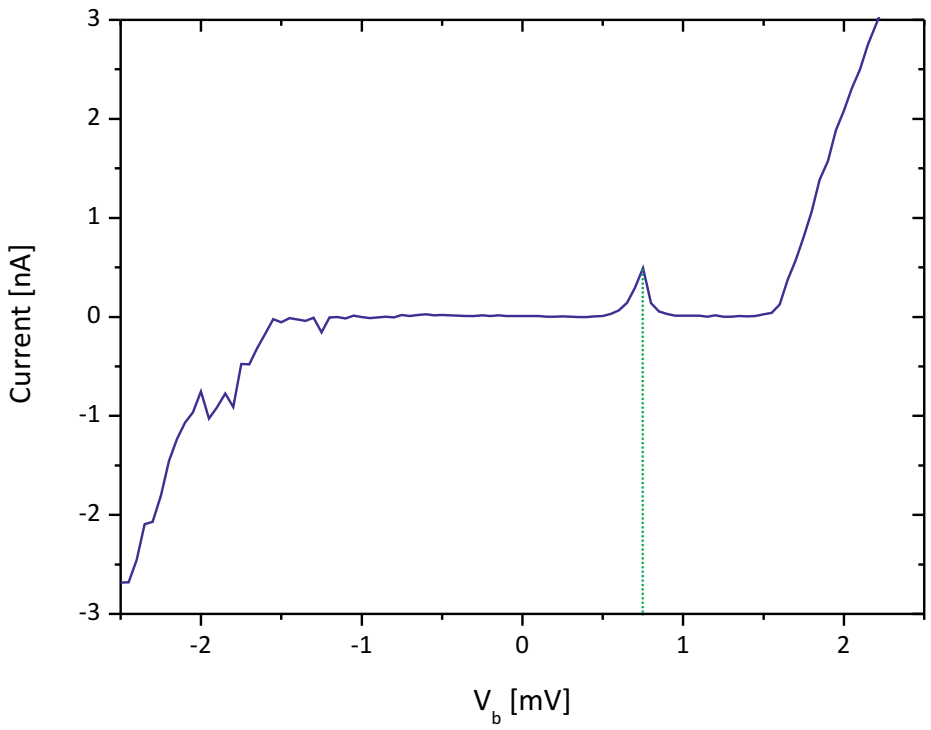

Figure 4.3: I-V characteristic of the SET taken at a QD gate voltage of -0.634 V as shown by the horizontal orange dotted line in Figure 4.2. The peak indicated by the green line is the 3e peak at a bias voltage of 0.749 mV.

The position of the 3e peak occurs close to $2E_c$. This gives a value for the charging energy of $E_c = 0.37$ meV.

We now turn to the measurement of the quantum dot. In order to observe the formation of the quantum dot, we measure the conductance of the SET as we vary the quantum dot gate voltage. The change in period of the CBOs shows the formation of the quantum dot and its isolation from the 2DEG.

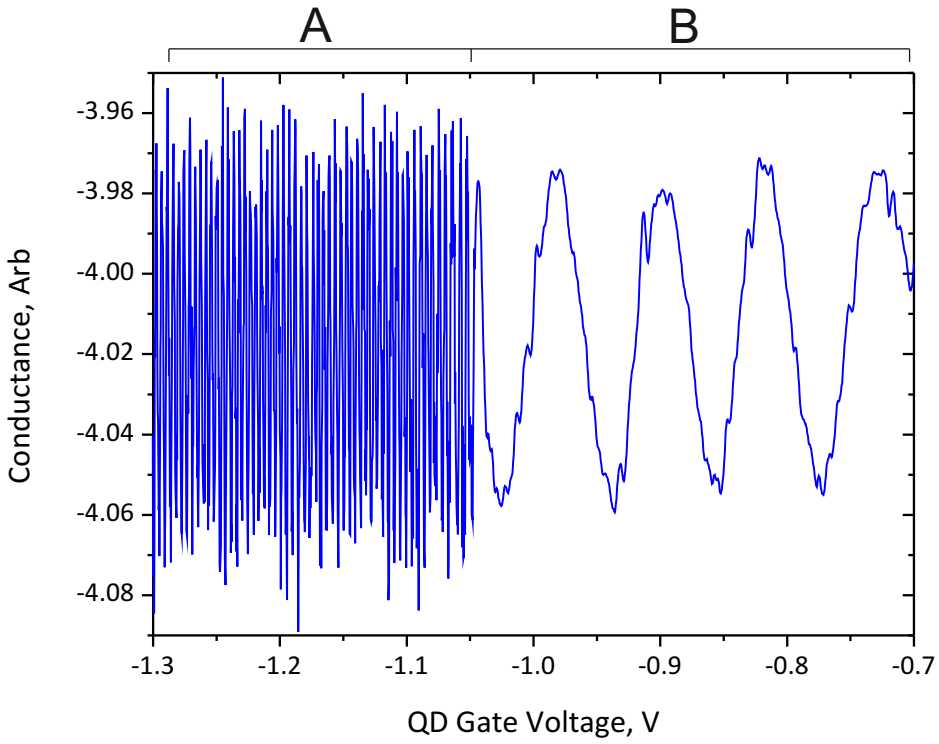

Figure 4.4: Coulomb blockade oscillations for SET 2. Section A: QD is decoupled from the 2DEG. Section B: QD is strongly coupled to the 2DEG.

Figure 4.4 shows the change in the period of the CBOs when the quantum dot is formed. Part B of Figure 4.4 with smaller amplitude and larger period oscillations represents the region where the dot is strongly coupled to the 2DEG. The CBO period of this region for this sample is measured to be 83.8 mV. As the negative bias on the quantum dot gate is decreased further, the dot forms and it becomes decoupled from the 2DEG, part A of Figure 4.4, with a period of 4.3 mV.

The period of CBOs is related to the capacitance of the SET to the gate by,

$$\Delta V_{gate} = \frac{e}{C_{gate}} \tag{4.1}$$

where $\triangle V_{gate}$ gate is the period and C_{gate} is the gate capacitance. Using the measured period for SET 2 we estimate the following capacitances in the two regimes,

$C_A = 3.70 \times 10^{-17}$ F

$C_B = 1.91 \times 10^{-18}$ F.

Referring to the top of Figure 2.2, we can understand this change in capacitance as follows. Before the dot is formed, when there is strong coupling between the QD and the 2DEG, the effective capacitance is equal to:

$$C_B = C_{QD}^{SET}. \tag{4.2}$$

When the dot forms and is isolated from the reservoirs the effective capacitance increases to:

$$C_{\mathrm{A}} = C_B + \frac{C_{QD}^{QD} C_{\Sigma}^{QD} C^{QD-SET}}{C_{QD}^{QD} C_{\Sigma}^{SET} + C^{QD-SET} C_{\Sigma}^{QD}} \tag{4.3}$$

when $C_{\Sigma}^{SET} \gg C^{QD-SET}$, $C_{\Sigma}^{QD} \gg C^{QD-SET}$ and $C_{\Sigma}^{QD} \gg C_{QD}^{QD}$. Thus, an increase in the SET capacitance, seen as an decrease in the period of CBOs signifies the formation of the QD.

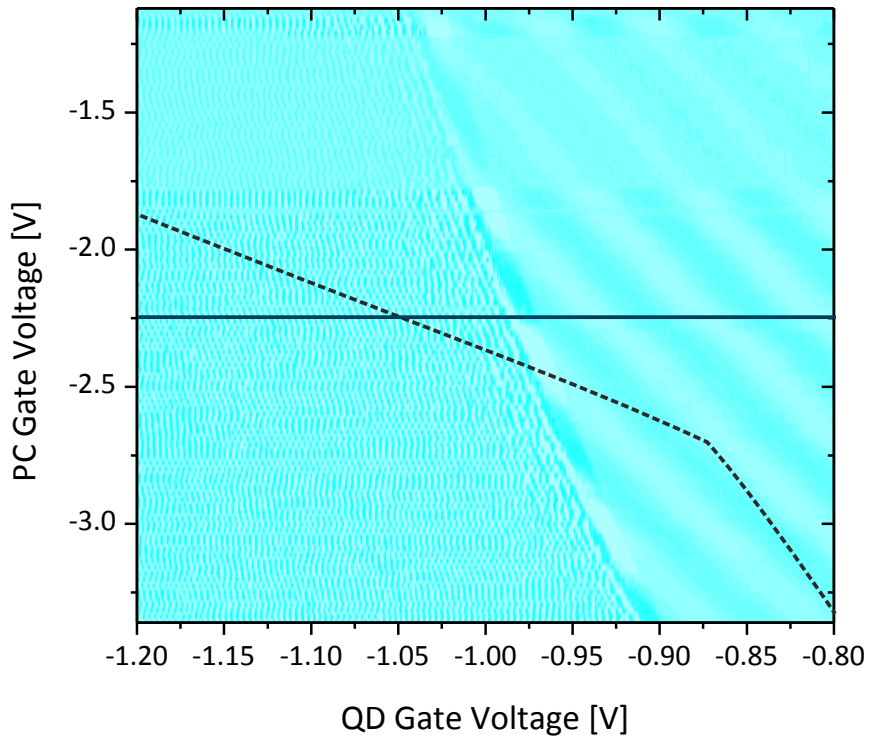

Figure 4.5: Conductance intensity map of an SET when both PC gate and QD gate bias voltages are varied. Dotted line indicates pinch-off of the mesa channel. This is a measurement of the current through the mesa as a function of the PC gate voltage and is taken from Figure 4.11.

The QD gate voltage at which there is a change in Coulomb blockade oscillations is believed to be the most sensitive region for photoresponse. This is the pinch-off boundary of the QD. Also for maximum sensitivity, the SET bias voltage is kept constant at the voltage where the I-V curve starts to develop a current ($V_b \sim 1.6$ mV in Figure 4.3). As can be seen from Figure 4.1, each QD-SET device also has a PC gate fabricated opposite to the QD gate. Due to its close proximity to the QD, this has the potential to affect the formation of the QD. This was investigated by measuring the SET current as a function of both the QD gate voltage and PC gate voltage. The resulting intensity map can be seen in Figure 4.5. As can be seen, the boundary between the region where the QD is formed and the region where the QD is coupled to the 2DEG, is not a vertical line, but has some slope. This shows the dependence of QD formation on the PC

gate voltage due to capacitive coupling. In practice, for terahertz detection the gate biases were set at or near the point where the two gradients - QD formation and mesa pinch-off (dotted line) overlap, as this is where the device is believed to be most sensitive.

4.1.3 Operation of a QD-SET sensor without Illumination

After characterisation and optimisation of the bias position, we perform measurements without terahertz radiation being incident on the sample, with the sample at 0.38 K. There is observable telegraph type switching of the SET current close to the pinch-off boundary. This signifies the escape of electrons from the QD followed by the tunnelling back of electrons. When the potential barriers of the QD are close to the electrochemical potential of the electrons within the 2DEG, these switching events occur as a result of thermal excitation of electrons. We refer to these as the 'dark count'. A time trace of the SET conductance shows the frequency of these dark switches, see Figure 4.6. This essentially forms the background noise when detecting terahertz radiation.

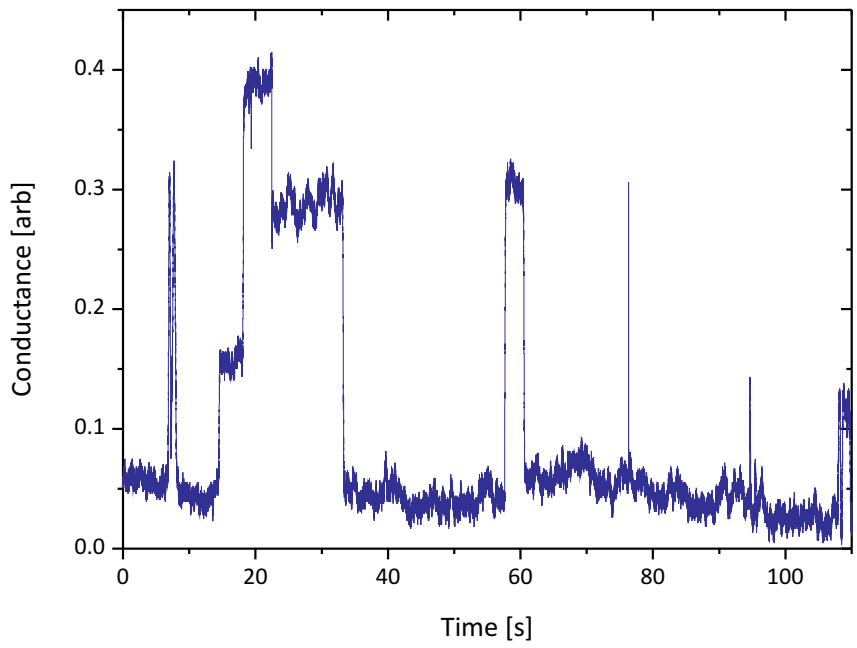

Figure 4.6: Time trace of SET conductance under no illumination showing tunnelling of thermally excited electrons. This is referred to as the dark count.

4.1.4 Operation of a QD-SET sensor under Illumination

When the height of the potential barrier of the QD is increased until it largely exceeds the electrochemical potential of electrons in the 2DEG, excitation of the thermal electrons is completely suppressed. However, these electrons can be excited out of the QD upon absorption of terahertz photons. The excitation of the electrons out of the QD is a two-step process: first localised plasma oscillations are excited in the vicinity of the QD; these plasma oscillations then decay with the energy handover to a single electron, which can subsequently overcome the QD barriers. If the time trace as in Figure 4.6 is repeated under terahertz illumination, one can see a clear increase in the switching rate as shown in Figure 4.7. The terahertz source used in this measurement was a blackbody resistor mounted in the fridge at $T = 1.5\,\mathrm{K}$, the temperature of the sample, with a bias voltage of $5\,\mathrm{V}$.

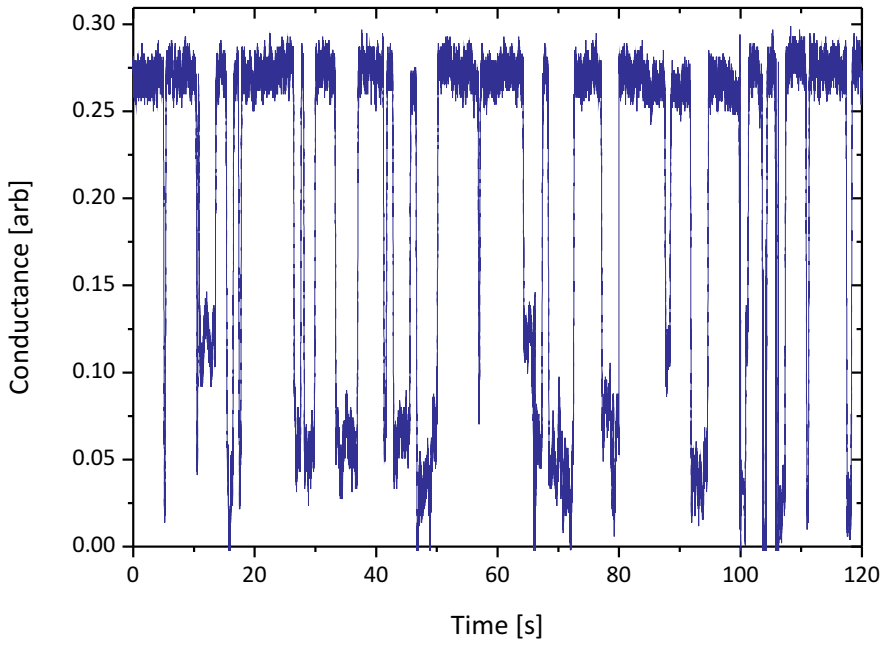

Figure 4.7: Time trace of SET conductance under terahertz illumination showing increased switching.

The switching rate is a clear indication of photoresponse. Measurements of

these switches were carried out for a variety of QD gate voltages. The traces were then analysed and the number of switching events for each 120 s trace was counted. The result of this is shown in Figure 4.8. It shows that there is a consistent increase in the number of switches between the dark count and the photo-induced count. We can also see that the maximum photoresponse is at the QD gate voltage corresponding to the bias voltage where the QD has just been formed and the mesa channel has just been pinched off (see Figure 4.5).

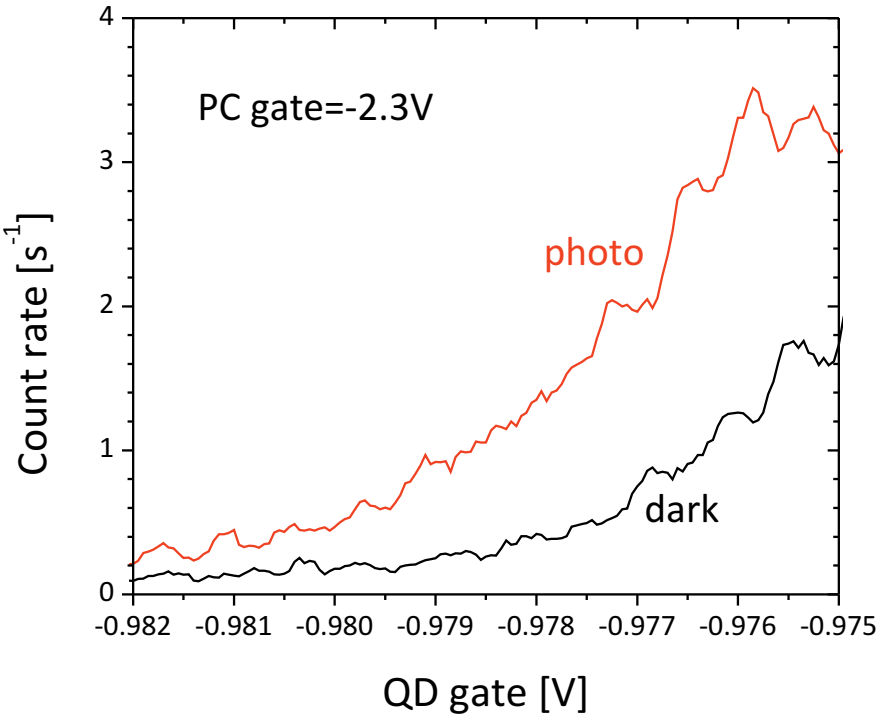

Figure 4.8: The rate of switching events (count rate) for various QD gate voltages measured when the sample is under terahertz illumination (photo) and under no illumination (dark).

When looking at the switching graphs in the transition between states, "on" to "off", the decay in conductance can be modelled as exponential, which goes as $\sim e^{-\frac{t}{\tau}}$ where τ is the characteristic decay time constant for a change in state to be measured. This gives an idea about the measurement bandwidth of the device. Figure 4.9 is an example fit of an exponential decay function to an “on” to “off” event taken from Figure 4.7.

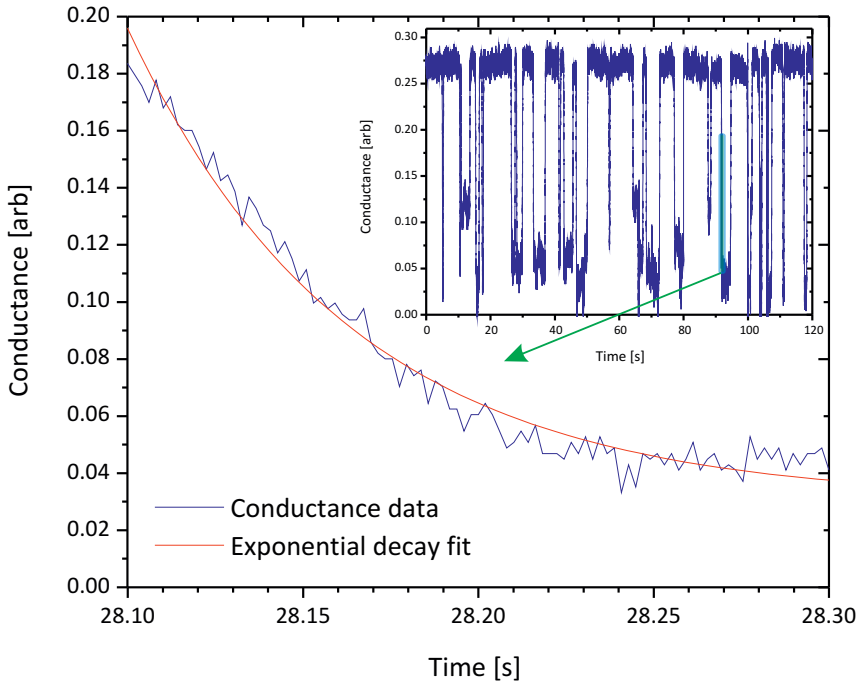

Figure 4.9: Close up of a decay from the "on" to the "off" state for a QD-SET sensor, showing an exponential-like decay. Data taken from Figure 4.7, shown in the inset.

An expected time resolution for the QD would be on the order of 1 ms. Similar work was carried out by T. Fuse et al. [78], in their work finding the time resolution of terahertz absorption in carbon nanotube single electron transistors, and Komiyama et al. [3] in their work on single photon detection. From measurements of sample T1, an average time constant, τ, of $\sim$ 62 ms was found. An estimate of the RC time constant of the experimental setup is made by calculating the total capacitance loading the SET. The loading capacitance is the capacitance of the thermocoax wires to the SET (Figure 3.14) and that of the filters in the system. This capacitance is calculated to be 40.35 nF. The resistance is the total of the SET resistance ($\sim$ 230 kΩ) and the 1 $M\Omega$ input impedance of the oscilloscope, giving 1.23 $M\Omega$. This results in an estimated time constant for the experimental setup of 50 ms. Thus, the difference in measured time constant to the expected is a result of the time constant of the experimental setup.

4.2 QD-PC: Measurements in the Dark

As a simpler alternative detection method to the QD-SET, QD-PCs were investigated. Unlike the SET, these devices lower the demands on fabrication and so have the potential to increase the yield of working THz detectors. We start with the characterisation of the QD-PC devices under no illumination from THz radiation.

4.2.1 Pinch-off

The conductance through the mesa, as described in section 2.3, can be restricted by the QD gate and the PC gate. The conductance drops off sharply as the channel is "pinched off" as shown in Figure 4.10. This is achieved by increasing the negative bias on the PC gate, such that the current is reduced through the PC and is pinched off.

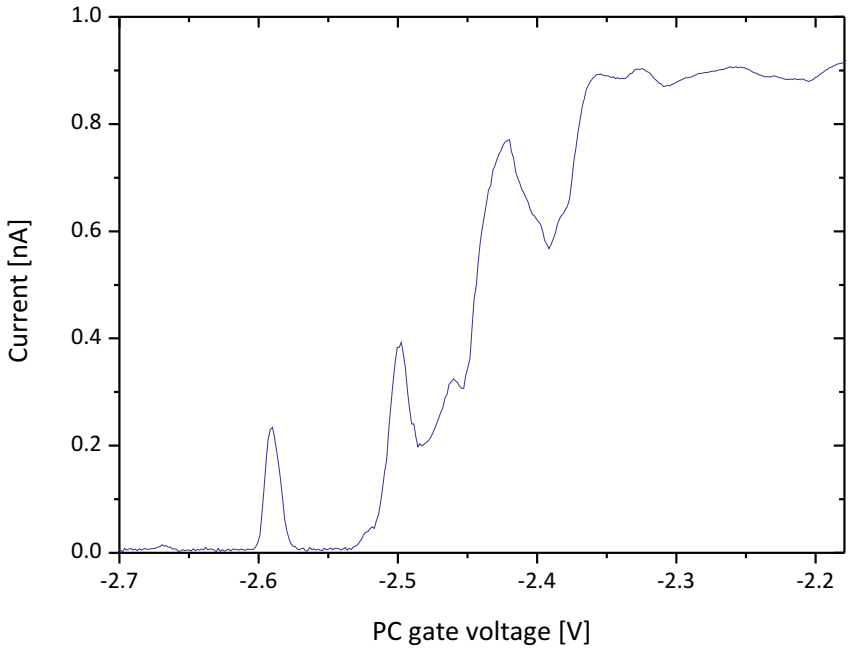

Figure 4.10: Graph showing the pinch-off of current through the point contact channel as the negative bias on the PC gate is increased.

An intensity conductance map of the PC was plotted by varying both PC and QD gate biases, in a similar manner as we did with the QD-SET device, see

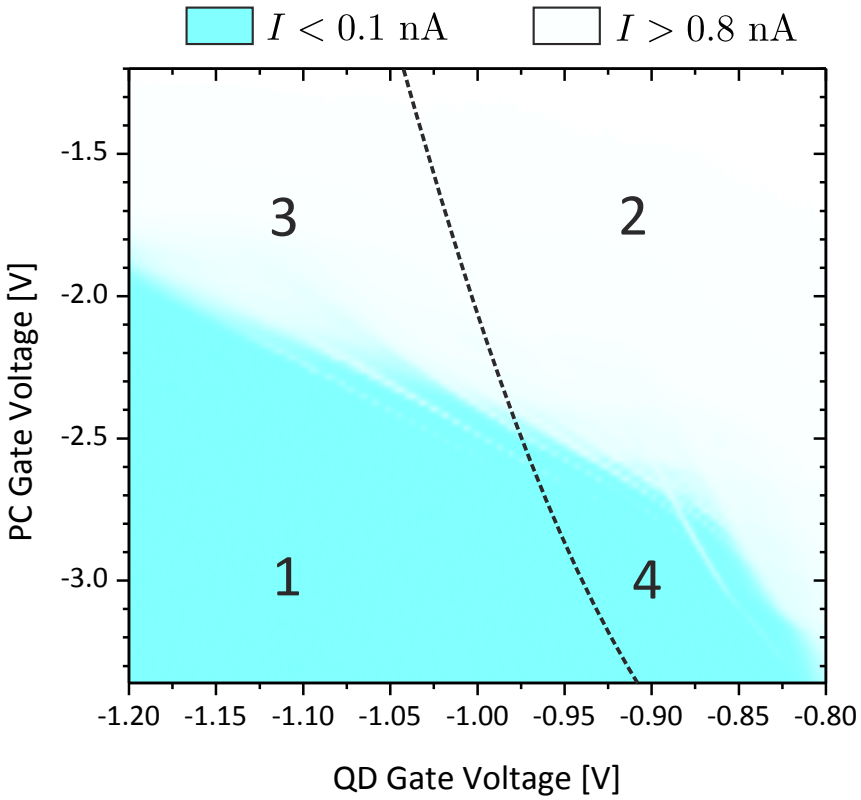

Figure 4.11: Conductance map of the PC current as a function of gate voltages. On the intensity scale, white corresponds to current 1 nA, and cyan to < 1 pA. The dashed line indicates pinch-off of the QD, taken from Figure 4.5. For the numbered regions, see text.

Figure 4.11. In this figure the white area corresponds to a high current through the PC channel while the cyan colour corresponds to zero current as the channel is pinched off. The dashed line within the figure indicates the pinch-off boundary of the QD taken from a map of the QD-SET readout of the same device (Figure 4.5). The region of the isolated QD and closed PC is marked as 1, the region of the open QD and open PC as 2, and the remaining two regions where the PC and the QD are open (closed) and closed (open) respectively are marked as 3 (4). Similar to the QD-SET device, the most sensitive region for biasing the QD-PC sensor is where the QD and PC channel are at the point of pinch-off, corresponding to the intersection between the two gradients found in Figures 4.5 and 4.11.

It would be expected that during pinch-off that the drop in current dI/dV would be a sharp, smooth transition but an oscillation in the current was observed, as seen in Figure 4.10. An investigation into these oscillations is reported in the following section.

4.2.2 Oscillations in the PC Channel

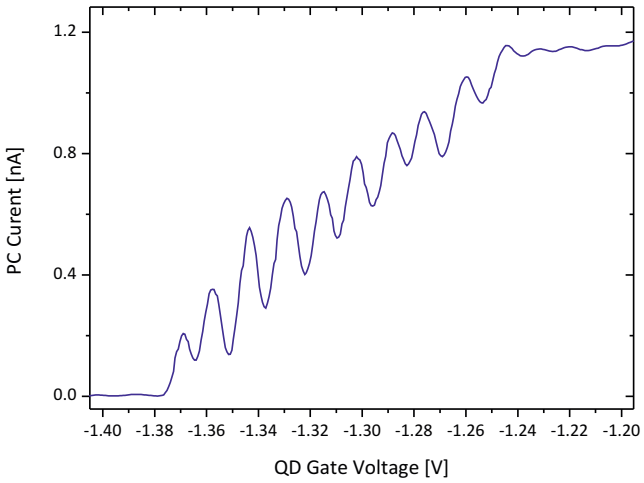

Figure 4.12: Oscillations in the PC current observed during pinch-off as the QD gate voltage was decreased.

During the QD-PC measurements it was noticed that there were observable oscillations in the PC channel. They are seen as the streaks in the intensity map of Figure 4.11. It was at first unclear what the cause of such oscillations could be. The contrast of the streaks decreases as the temperature rises, however they were still clearly visible at 1.5 K. Further measurements were taken at a higher voltage resolution to obtain a clearer picture. Figure 4.12 shows these oscillations more clearly. A conductance map was taken, again measuring conductance through the mesa as a compilation of sweeps of the PC gate, at different QD gate voltages. Diagonal streaking in the area between the conductive and pinched-off regions is seen. These streaks stem from the peaks and troughs of the oscillations, and are dependent on the gate voltages. The pattern is reproducible and stable as can be seen from the alignment of the streaks throughout the scan.

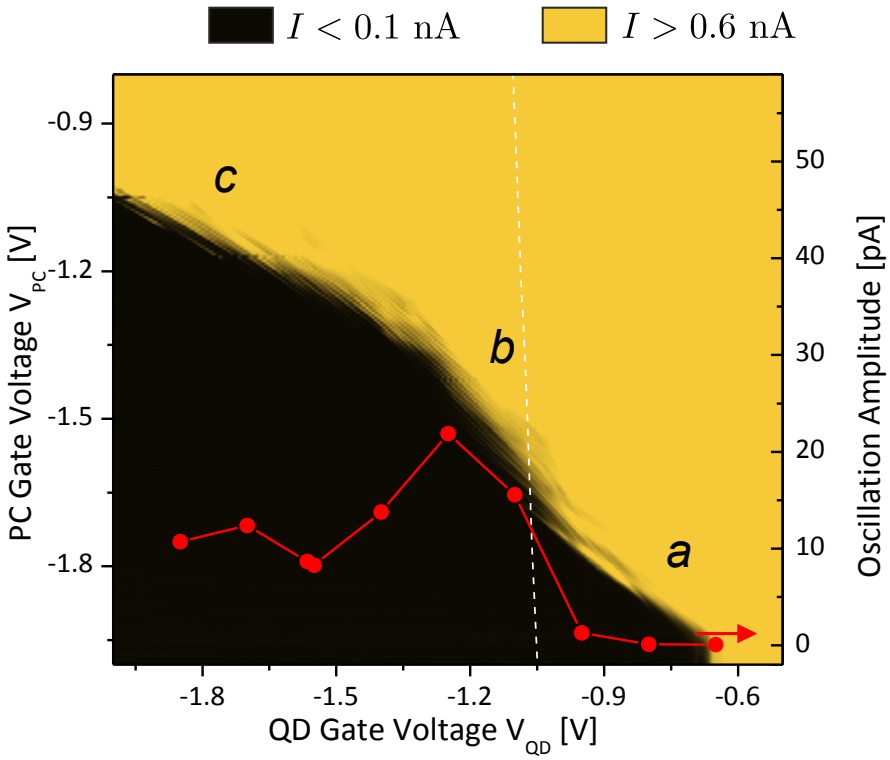

Figure 4.13: Conductance map of the source-drain current I_{SD} in coordinates of V_{PC} and V_{QD} close to pinch-off. Bright and dark colours correspond to 1 nA and < 1 pA, respectively. There are three distinct regions of PC operation marked by a, b and c. In regions a and c the pinch-off boundary is a straight line with identical slopes, in region b the slope is larger. The white dashed line in the plot indicates the boundary separating regions where the QD is isolated (left) and strongly coupled to reservoirs (right). This boundary is taken from analysis of the SET operation. Periodic oscillations of the current through the mesa are observed when crossing the pinch-off boundary. The red data points show the maximum amplitude of the oscillations, showing that the oscillations are strongest in region b and weaken in regions a and c.

Closer inspection of the conductance map (Figure 4.13) shows an asymmetry in the pinch-off boundary. This is a result of the geometric differences between the QD and PC gates. The boundary region of Figure 4.13 can be split up into three distinct regions: the slopes a and c have similar gradients, whilst in region b the gradient is larger indicating a higher sensitivity of the PC to the QD gate in this region. The change in slope can be attributed to a change in ratio of capacitances, C_{PC}^{PC}/C_{QD}^{PC}, where region b has a ratio of 0.78, and regions a and c have a ratio of 2.1. C_{QD}^{PC} and C_{PC}^{PC} are the capacitances of the PC to the QD gate

and to the PC gate respectively.

In region b the the gate voltages are such that the conductance channel is formed exactly between the PC and the QD gates. This is the region where the system can be used as a terahertz detector [79]. Here, as the negative bias of the QD gate is decreased further the QD becomes more isolated from the reservoirs, this increases the effective capacitance C_{QD}^{PC}, because of additional parallel capacitance between the QD gate and the PC through the isolated QD. The point at which the QD becomes isolated is marked on Figure 4.13 as a dotted white line, and is taken from the experiments with the SET as described in Section 4.1.2.

In region a the PC gate voltage is very negative. This causes the conductance channel to be shifted in the direction underneath the QD gate, so that the QD can only be formed simultaneously with a pinch-off of the conductivity. In region c the very negative QD gate voltage combined with a weak PC gate voltage causes the conductance channel to be pushed underneath the PC gate. The QD is already isolated from the reservoirs, because V_{QD} is beyond the dashed white line. An additional capacitance of the QD gate to the conductance channel because of the isolated QD is present but it is small due to the QD and conductance channel being spatially separated from each other. This explains why the slopes of the pinch-off boundary in regions a and c are almost identical, as the mechanism for pinch-off in the two regions are very similar.

Oscillations of the current through the mesa, and therefore the PC channel, are observed close to the pinch-off boundary in region b and weaken and disappear within regions a and c as shown in the red overlay graph in Figure 4.13. Large amplitude oscillations can be seen around $V_{PC} \sim -1.45$ V and $V_{QD} \sim -1.25$ V. The oscillations were observed in 50% of the samples studied, including samples made of the same wafer. Similar observations of oscillations within a narrow conductance channel have been observed in other experiments, both in 2DEGs

in GaAs/AlGaAs as well as Si quasi-1D systems [39, 80, 81]. In one of these examples [81] phosphorus atoms were embedded in the quasi-1D channel. This brought about the formation of a few electrons around the impurity, which resulted in Coulomb blockade peaks in the conductance. However the period appeared irregular, unlike the periodic oscillations we observed. Usually aperiodic oscillations are a result of two or more coupled dots forming in the conductance channel [82], thus the observation of periodic oscillations indicates the formation of a single dot in the conductance channel. In order to determine whether the origin of this effect is indeed a result of Coulomb blockade a stability diagram was taken (similar to that shown in Figure 4.2), see Figure 4.14.

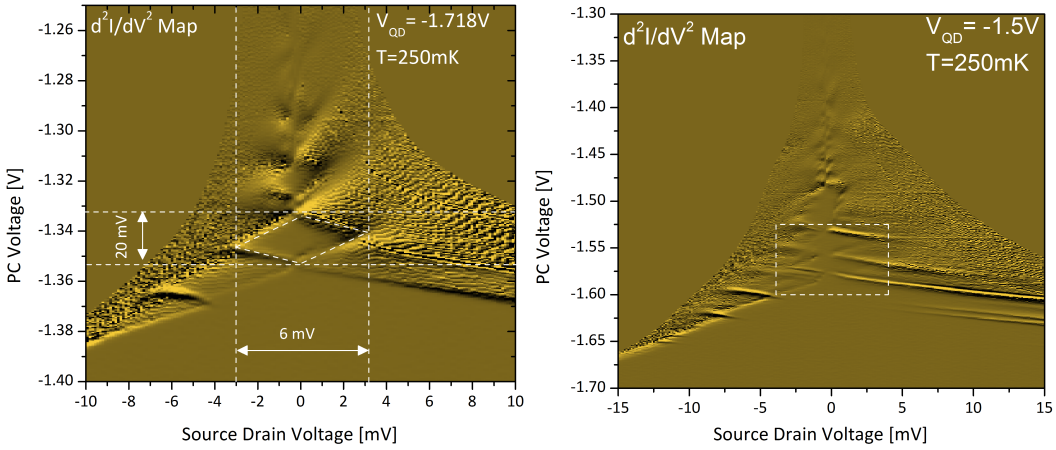

Figure 4.14: Stability diagrams taken at two different QD gate voltages. The dashed box in the right image is shown in Figure 4.15.

The map was taken by varying the PC gate voltage and source-drain voltage across the mesa and measuring the current through the mesa. The second derivative of the measured current with respect to the source-drain voltage, d^2I_{SD}/dV_{SD}^2, was plotted as the oscillatory component can be seen with greater clarity. As can be seen in Figure 4.14, the features are akin to the features seen in the SET diamond graphs and are typical for the Coulomb blockade effect. These maps were taken for a variety of different QD gate voltages (V_{QD}). A zoomed in view for $V_{QD} = -1.5\,V$ is shown in Figure 4.15.

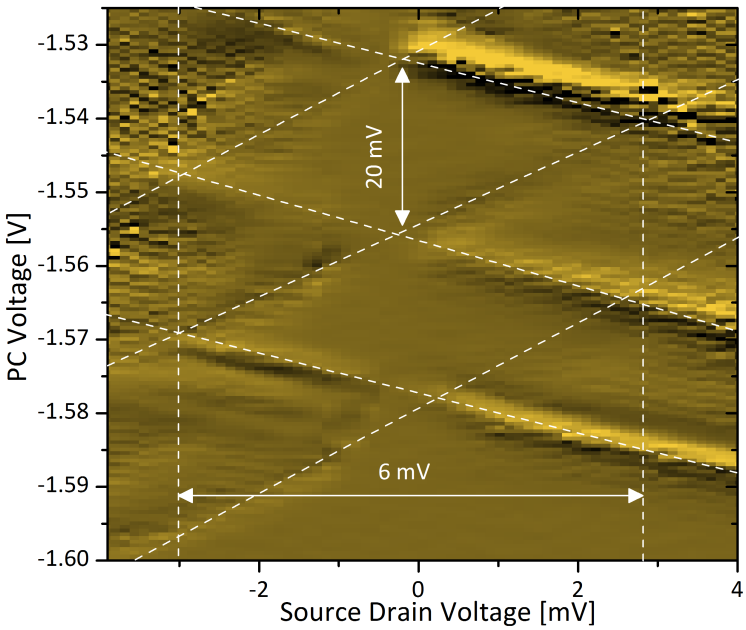

Figure 4.15: Intensity plot of $-d^2I_{SD}/dV_{SD}^2$ close to pinch-off. The white dashed lines are guides to the eye depicting the diamond-shape of the stability diagram.

It is from this we make the assumption that a small dot (SD) is present within the conductance channel. Estimates of the charging energy, of approximately $E_C \sim 3$ meV, can be taken from the horizontal width of the diamonds. Using the formula for the capacitance of a circular disc to the conductive plane:

$$d = e^2/[4\varepsilon_0(\varepsilon_r + 1)E_C] \tag{4.4}$$

we can estimate the diameter, d, of the small dot. We model the dot as a circular disc inside the conductance channel, to be ~ 100 nm, where ε_0 is the permittivity of free space, $\varepsilon_r = 13$ is the effective permittivity of GaAs, and e is the electric charge. This size of the dot is feasible as the channel between the QD and PC is approximately 200 nm, therefore such a dot would fit within the channel.

When the conductance oscillations over a wide range of V_{QD} were analysed, the period was found to be $\triangle V_{QD} \sim 14$ mV, corresponding to a capacitance of $C_{QD}^{SD} \sim 1 \times 10^{-17}$ F between the QD gate and the small dot. Using 3D FlexPDE [83] we were able to solve the Laplace equation for a QD gate SD system with

the aim to get $C_{QD}^{SD} = 1 \times 10^{-17}$ F. This resulted in a diameter of $\sim$ 35 nm for the small dot, which differs from the the value calculated from the charging energy by almost a factor of three. Corrections will need to be made to the simulated value by adjusing the coefficients. The small dot is formed between the QD and PC gate and considering the range of estimated diameters would consist of approximately between $\sim$ 3 and 30 electrons. The mechanisim by which the dot is formed is still unclear, but the clear periodicity seen in our samples unlike those seen by Graaf et al. [81], and relatively large size of the dot estimated from the charging energy, indicates a single dot, formed by a single impurity atom or a small cluster of impurity atoms, in the conductance channel.

4.3 QD-PC: Measurements under Illumination

4.3.1 Characterisation of the QD-PC sensor and Improvements to Setup

For each of the QD-PC samples a conductance map and photoresponse map were taken in the presence of terahertz radiation. The conductance maps are taken in the same manner as described for the QD-PC without illumination. The photoresponse maps are taken simultaneously and is a measurement taken from the lock-in of the difference in current through the mesa when the device is under illumination and in the dark. This is done by chopping the radiation at a reference frequency.

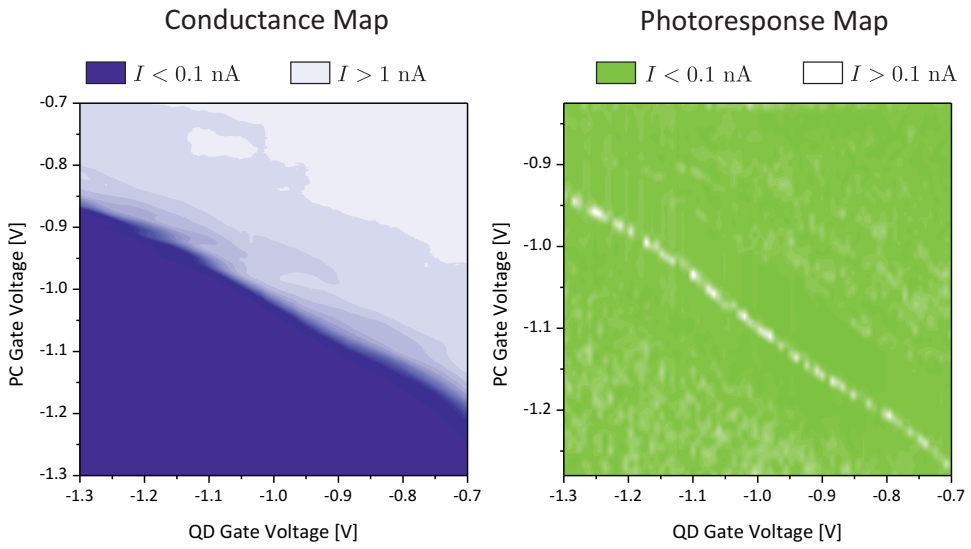

Figure 4.16: Conductance map and photoresponse of QD-PC sample using gates G2 and G6 on sample T40 (see Figure 4.1).

The THz source used for these responses was a blackbody resistor placed inside the fridge at 1.5 K and was electronically chopped by placing a pulsed signal upon it. It was mounted in a reflective metal cup and was suspended to decrease thermal contact to the walls of the cup. This resistor was initially lined up 2 cm away from the sample with a gap between the sample holder and the cup. The first scan taken is shown in Figure 4.16. On warming the system up, a closer inspection of the sample holder and source arrangement was taken. It is believed that during the cool down, thermal contractions caused misalignments of the source and the sample, such that the source was no longer optimally aligned to be incident on the sample. This would obviously result in a small photosignal.

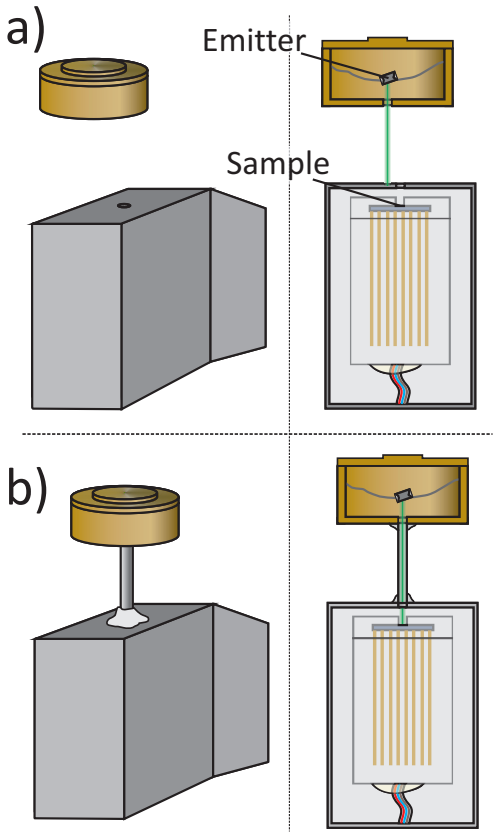

Figure 4.17: Schematic of the addition of a light pipe. Image a) depicts how the path of radiation often became misaligned. Image b) depicts how the addition of a fixed light pipe corrected this problem.

A stainless steel light pipe was thus installed to ensure line of sight between the source and sample, during the next cool down, as depicted in Figure 4.17. Figure 4.18 shows the photoresponse taken after the holder adjustment. A stronger photoresponse can be seen, as demonstrated in Figure 4.19, which shows a slice through the photoresponse map at fixed QD gate voltage. Although the exact position of the pinch-off boundary varied slightly upon each cool down, observations of the conductance map and photoresponse map show that the maximum photoresponse occurs at the pinch-off boundary. This was consistent across all samples measured. Also noticable are the streaks in conductance from the oscillations described in Section 4.2.2, which cause streaks in photoresponse as expected due to the repeated sharp dI/dV of the oscillations.

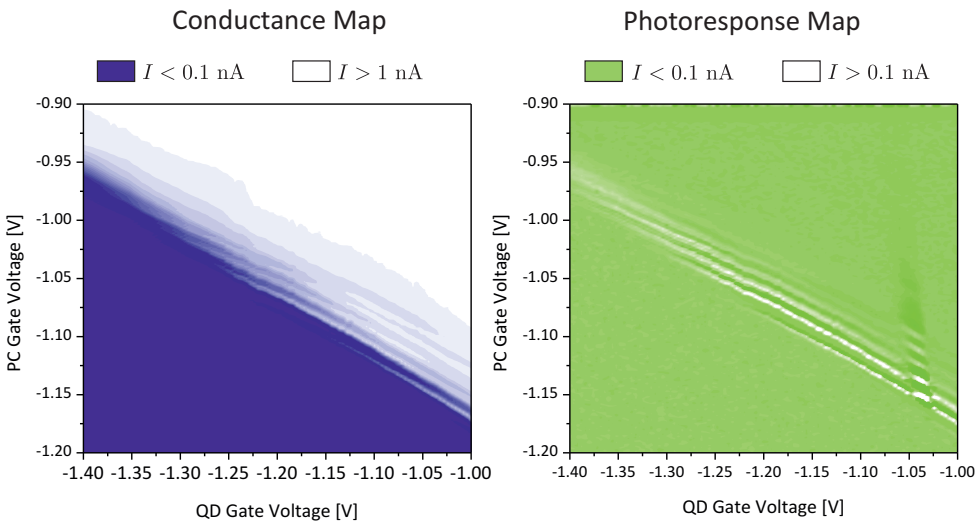

Figure 4.18: Conductance map and photoresponse of the QD-PC sensor using gates G2 and G6 on sample T40 with improved sample holder.

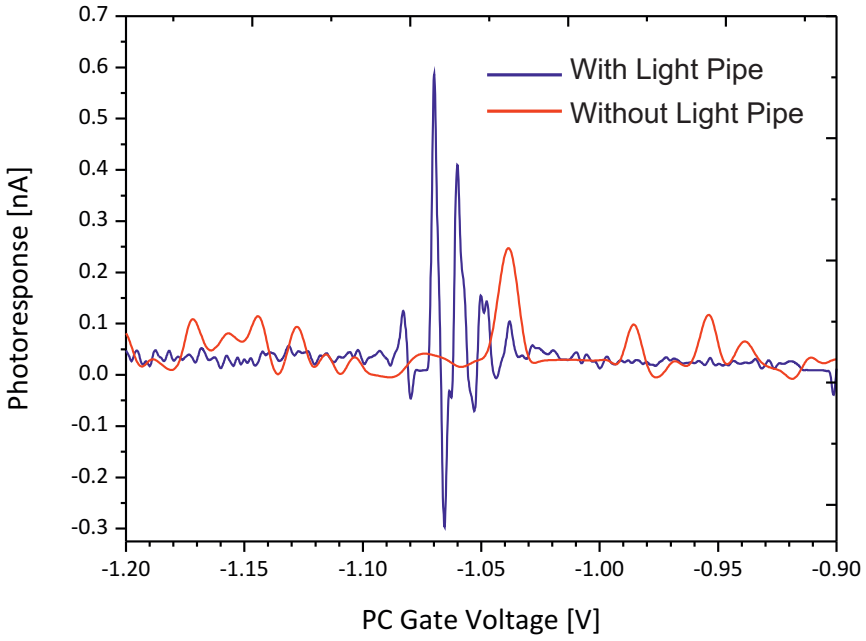

Figure 4.19: Comparison of photoresponse for sample T40 without light pipe installed and with light pipe installed. The data shows a slice through the photoresponse map at a fixed QD gate voltage.

4.3.2 Analysis of the Photoresponse

Figure 4.20 shows a cross section of a conductance map of a QD-PC sensor on sample T1 at a fixed QD gate voltage of -1.06 V. The current through the PC as a function of the PC gate voltage near pinch-off without illumination is shown as a grey line in Figure 4.20. As power was applied to the emitter, the position of the pinch-off boundary, as a whole, shifted (see red curve in Figure 4.20). We modulated the emitter power at 9 Hz, using the lock-in technique to demodulate the PC current at twice the reference frequency, in order to determine the photoresponse. The maximum photoresponse measured is noted to be comparable to the current of a completely open PC.

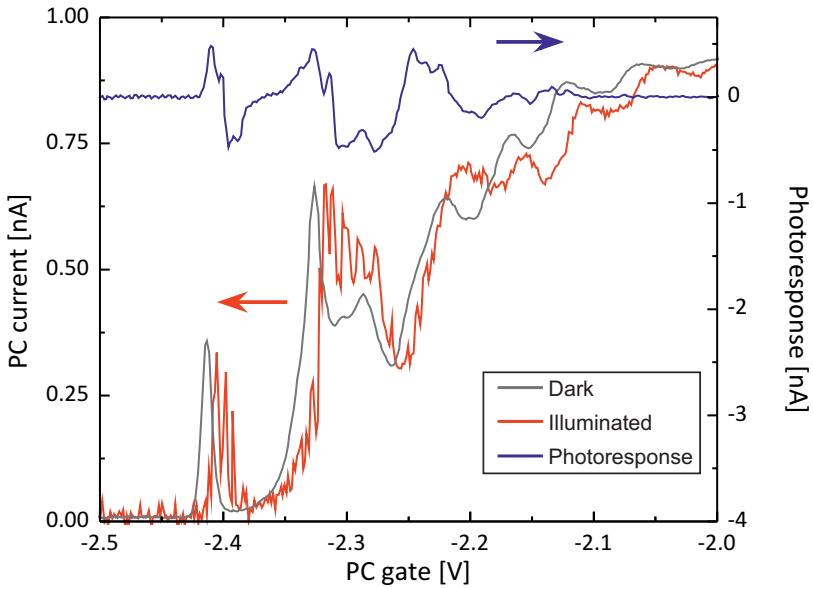

Figure 4.20: Current through the PC close to the pinch-off boundary in the dark (grey) and under illumination (red). $V_{QD} = -1.06$ V. Photoresponse measured with the lock-in technique (blue). The axes for each graph are indicated by the arrows.

There are a number of noticable features in Figure 4.20. One would be the oscillations in the pinch-off under illumination (red curve), these can most prominently be seen between -2.34 V and -2.27 V on the PC gate voltage. After a short investigation it was found to be artifitially induced by modulation of the applied

radiation due to the low reference frequency used to modulate the applied emitter. Another noticable part of the graph is the apparent lack of photoresponse for the region between -2.1 V and -2.0 V PC gate voltage, despite the clear difference in the two pinch-off graphs. This was found out to be a software error of the lock-in amplifier, which was later resolved.

Through a number of previous experiments and basic theory, it is thought that the greatest sensitivity of the device should be at the point of pinch-off for both the QD and the PC. This is due to the large gradient of current dI/dV in this region. This region is marked in Figure 4.11 as the point at which the dotted line crosses the pinch-off boundary for the PC. However, we also notice enhanced temporal fluctuations in the PC current in dark conditions close to pinch-off. With the gate potentials fixed, it is the charge state of the QD that determines the PC conductance. Near pinch-off, it was observed that the thermal excitations are sufficient to induce charge fluctuations on the QD. This is the cause of the large dark signal shown in Figure 4.21. The dark signal dies away at smaller negative biases, where the QD was strongly coupled to the 2DEG, and at a more negative bias when the QD had high barriers preventing thermally induced charge fluctuations.

In a QD-PC sensor, it should be noted that the PC and the QD are connected in parallel, and the PC bias voltage is also applied across the QD through the mesa. This voltage causes asymmetry of the QD barriers, hence the PC is probing a slightly different QD to the nearly symmetric one formed for operation with the SET. In Figure 4.21 the absolute value of the maximum photoresponse is shown for different biases at the QD gate. The sign and magnitude of the photoresponse at different QD and PC gate potentials near the pinch-off boundary follows the same pattern as that of the dark signal. When a small power of less than 3 mW was applied to the emitter the photoresponse was identical to the dark signal and was only visible in the region where the QD gate voltage was approximately

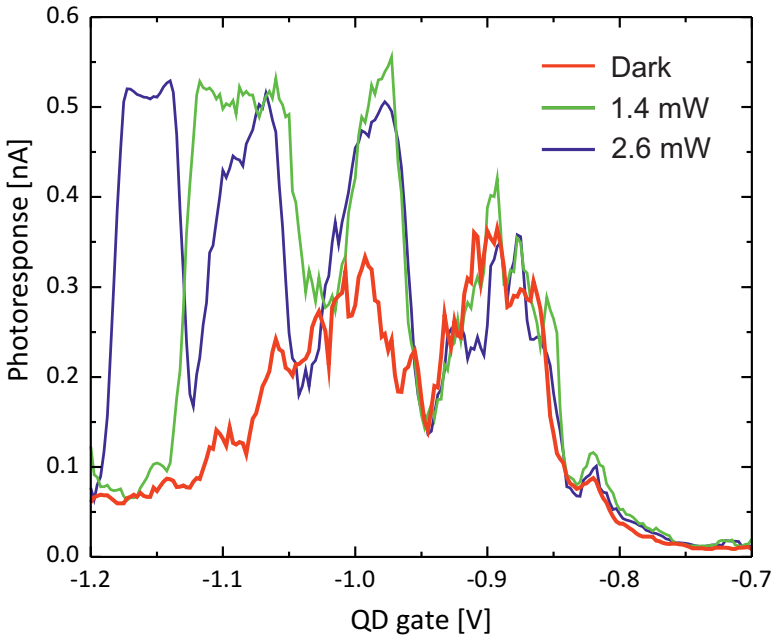

Figure 4.21: Photoresponse of the QD-PC sensor as a function of QD gate voltage for different powers dissipated on the emitter: no power (Red), 1.4 mW (Green), and 2.6 mW (Blue).

$-0.9\,\mathrm{V}$. On increasing the photon flux by increasing the power on the emitter, the photoresponse region extends to a QD gate voltage of around $-1.2\,\mathrm{V}$. Therefore, the signal-to-noise ratio appears to be improving towards a more negative QD gate voltage.

4.3.3 Dependence of Photoresponse on Emitter Power

The power dependence of the photoresponse was investigated and the maximum photoresponse was measured for varying powers on the emitter as shown in Figure 4.22. This was measured at two different temperatures of the fridge, 0.3 K and 1.5 K. At $T = 0.3\,\mathrm{K}$ there appears to be a peak at a power of approximately 2.6 mW whereas at $T = 1.5\,\mathrm{K}$ the peak is at approximately 3.1 mW. At higher emitter powers, both signals decrease, when it would be expected that increasing the power and therefore the photon flux should continue to increase the response. This is most likely due to heating of the sample from the emitter, which impairs the performance of the sensor.

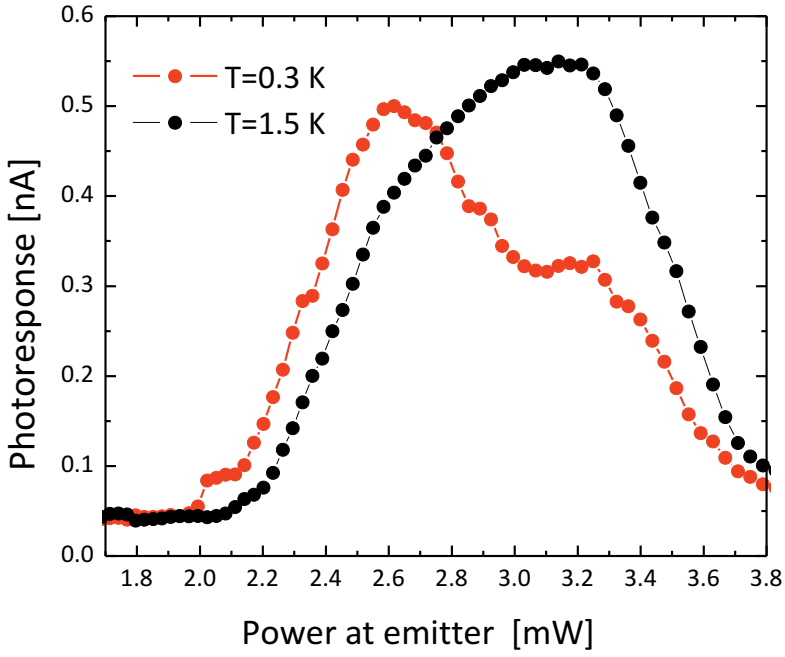

Figure 4.22: Dependence of photoresponse of a QD-PC sensor on the power of the terahertz emitter, measured at two different temperatures of the sensor (0.3 and 1.5 K), QD gate voltage = −1.01 V .

The use of an internal source (in this case the resistor) was to determine whether a photoresponse was present using a simplified system. The system was then set up to allow for external sources to enable imaging of samples exterior to the fridge, by removing the blackbody source and aligning the detector to the optical windows of the fridge; Figure 5.7 in Section 5.4 shows this. The first source tested was the Gunn diode. This had the ability of allowing the power to be adjusted via adjustment of an attenuator. Figure 4.23 shows a comparison of the maximum photoresponses as a function of the QD gate voltage for a variety of different powers. The results are as expected with the highest response being at the point of pinch-off, where the gradient dV/dI is sharpest and decreasing as the gate voltage is changed in either direction away from it. It can also be seen that there is a tendency that the photoresponse saturates at higher powers, much like the behaviour seen in Figure 4.21.

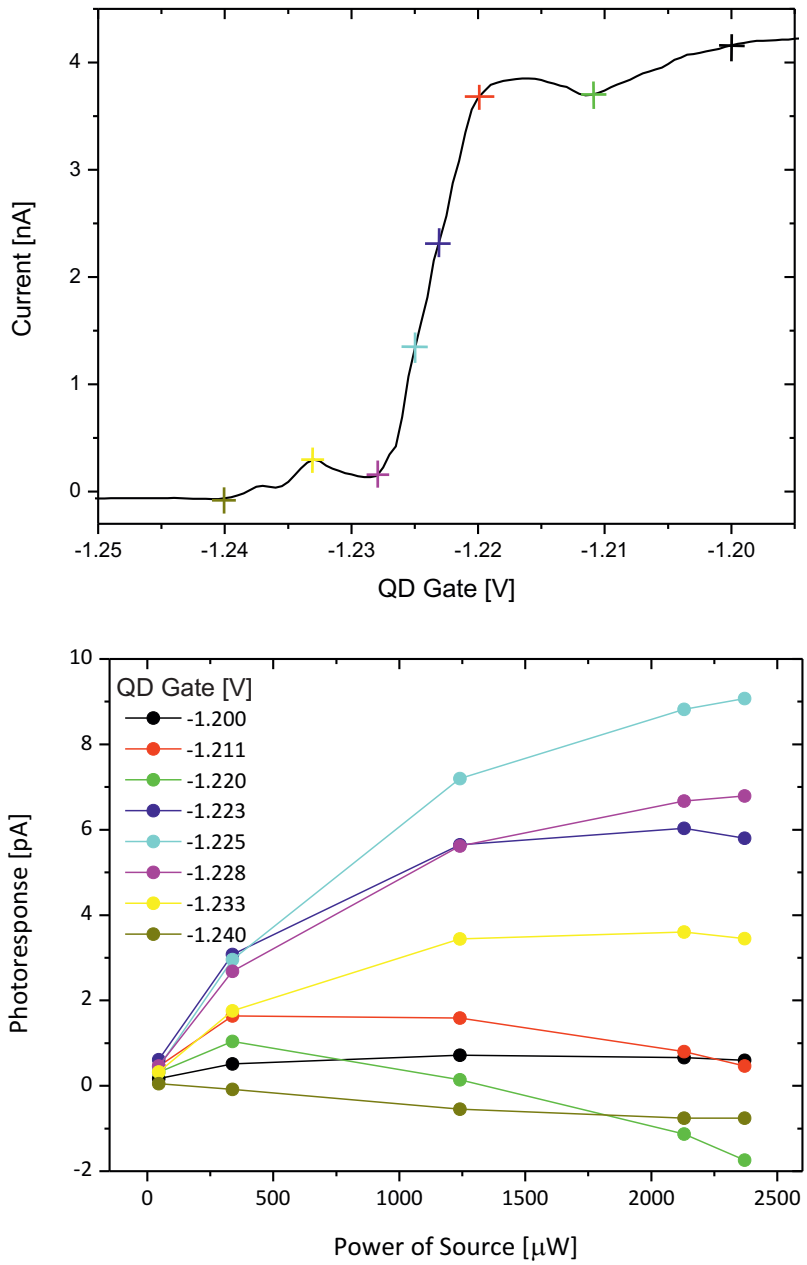

Figure 4.23: Top: Graph showing pinch-off of the PC as a function of QD gate voltage. Bottom: Maximum photoresponse as a function of emitter power (Gunn diode) with the QD-PC sensor biased at the QD gate voltages as marked in the top figure.

4.4 Comparison of QD sensors

The charge sensitivity of the SET and PC is determined by the transconductance, dG/dV_g, and the capacitive coupling between the PC and SET to the QD, V_g being

the voltage applied to the gate forming the PC or the SET gate. In our device we can combine two factors by introducing the sensitivity of the source-drain current to charge variation at the QD, dI/dQ. Once the charge current noise in the system, which within our system is $\delta I \sim 3$ pA with a bandwidth ~ 1 kHz, is known, the level of QD charge excitation is:

$$\delta Q = \delta I/(dI/dQ) \tag{4.5}$$

A moderate sensitivity of the PC to charge excitation was found in region b of Figure 4.13, $dI/dQ \sim 4 \times 10^6$ A/C. The PC is able to detect excitations of $\delta Q \sim 4e$ in or out of the QD in a bandwidth of 1 kHz. The Coulomb blockade oscillations observed in the PC bring improvements to the sensitivity where they are present. Typically the maxima of dI/dQ are higher by $\sim$ 15% in these regions. The drawback to these improvements is that the operation points are reduced to the maxima of these oscillations. These narrower operation points cause an increased difficulty in operation as operation points have been known to drift during long scans. The sensitivity of the SET readout is only slightly higher $dI/dQ \sim 10^7$ A/C. It is identical along the boundary where the QD is formed. Sensitivity has 25% variation depending on the operation point. The SET allows one to detect an excitation of $\delta Q \sim e$ in a bandwidth of 1 kHz. Our estimation is on the lower side, since excitations of individual electrons are clearly seen in the QD-SET device.

Although the QD-SET sensors are more sensitive than the QD-PC sensors, the QD-PC sensors have shown that a clear photoresponse is possible from the detection of charge excitations of a few electrons. It also has the benefit of a potentially much higher operating temperature of at least 1.5 K,which together with its robustness compared to the QD-SET sensors makes it more appealing in terms of usability. The following section is an account of the use of these QD-PC sensors in a spectroscopic configuration.

4.5 Array of QD-PC Sensors

The principle behind the array of QD-PC sensors was to provide a variety of different size dots, with different plasma frequency resonances, to be tested at once. The benefit of this would be for the possibility of spectroscopy measurements. There have been many key iterations in design for the QD-PC arrays. The first, Figure 4.24, contained 8 sensors which consisted of two lateral dots which act as the point contact.

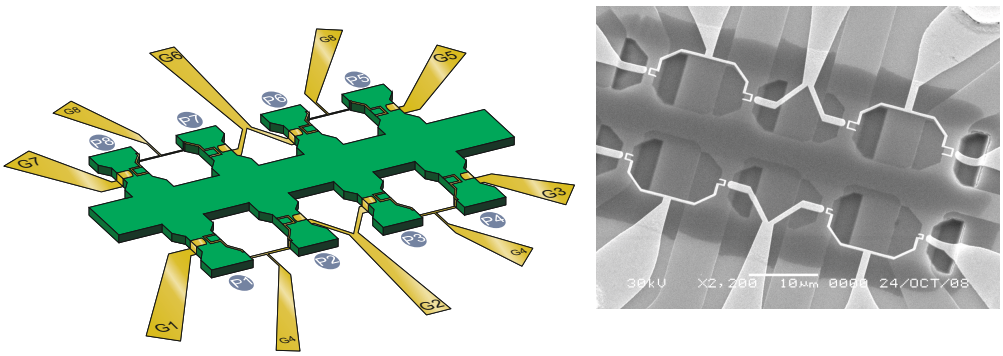

Figure 4.24: Schematic of array of first design, and SEM image of device.

The next design incorporated 14 sensors, in 2 rows of 7. It is of a similar design to the previous array but this time contained common gates, this can be seen in the left image of Figure 4.25. If one follows the gate connections it can be seen that there are only 4 gate connections - one for the left of the first row and one for the right, and the same for the second row. This should provide easier operation, removing the need to manually set a large number of gates. Each sensor consisted of different size QD gates, so that an array of different sized QDs could be formed. This is what makes the array a spectroscopic detector. Also shown in this picture are the antennas used to couple the radiation to the sample. They are bow-tie antennas named after their distinctive shape. They are simply large areas of metal, fabricated into this shape.

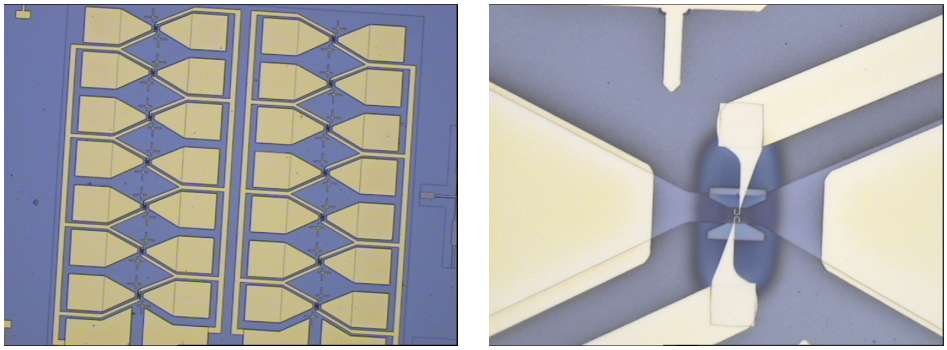

Figure 4.25: Left: SEM image of sensor showing gold contacts for all 14 sensors. Right: Zoomed in image of one of the sensors showing the quantum dot gates.

This design was extended to an array of 24 sensors, arranged in 3 rows of 8 sensors, which would provide an even greater resolution. These comprised 8 different sizes of QD gates. Once an array design is finalised and is sufficiently robust the goal is to use all sensors combined with a multiplexing system to provide a richer amount of data whilst imaging. A series of pinch-off graphs and photoresponses were measured at two temperatures of the fridge (Figure 4.26). The source used was the Gunn oscillator operating at 170 GHz, with a power of 1 mW. The sensors are labelled by the identifier of S followed by the row number then the numbered sample, for example the first one would be S11 whilst the last one would be S38.

Table 4.2 shows some basic information relating to the 3×8 sample. The first radius is taken from the schematic for the lithographic process and should be considered an accurate measurement of the radius of the QD gate, and therefore the QD. The frequency was calculated using Equation 2.9 in Section 2.5 to predict the resonant plasma frequency of the dot in relation to it radius. The resistance and pinch-off voltages are experimentally measured for each sample.

Sensor	**S11**	**S12**	**S13**	**S14**	**S15**	**S16**	**S17**	**S18**
Radius [μm]	0.575	0.775	0.975	1.175	1.375	1.575	1.775	1.975
Resistance [kΩ]	1.26	1.14					1.32	1.14
Pinch-off Voltage [V]	-0.424	-0.409					-0.558	-.0.265
Frequency [THz]	0.380	0.316	0.297	0.272	0.525	0.236	0.222	0.211
Sensor	**S21**	**S22**	**S23**	**S24**	**S25**	**S26**	**S27**	**S28**
Radius [μm]	0.575	0.775	0.975	1.175	1.375	1.575	1.775	1.975
Resistance [kΩ]	0.90	2.00	0.88	1.38				
Pinch-off Voltage [V]	Voltage was increased until -1.5V with no pinch-off							
Frequency [THz]	0.380	0.316	0.297	0.272	0.525	0.236	0.222	0.211
Sensor	**S31**	**S32**	**S33**	**S34**	**S35**	**S36**	**S37**	**S38**
Radius [μm]	0.575	0.775	0.975	1.175	1.375	1.575	1.775	1.975
Resistance [kΩ]			1.66	1.10				
Pinch-off Voltage [V]			-0.353	-0.399				
Frequency [THz]	0.380	0.316	0.297	0.272	0.525	0.236	0.222	0.211

Table 4.2: Basic measurement data for 3×8 array.

After testing the 3×8 array it was found that a number of sensors did not work including all in row 2 because of leaking of the inter-crossings of the leads to gates. Due to the complexity of having a large number of devices in an array there are a large number of connections required. 'Jumper' sections are required to allow to connect across current paths, which are difficult to fabricate. Figure 4.26 shows the results for the remaining working samples of the 3×8 array tested. The measurements shows clear photoresponse at the pinch-off of conductance. The photoresponse appears to have a dependance on temperature as a number of the responses were improved at 0.5 K as seen, for example in the increase in response for sensor S17. Not all sensors showed an increase in response; sensor S34 for example shows a dramatic reduction in reponse along with sensor S12. Both of these sensors have very similar pinch-off voltages, which could mean there is a similarity in their formation, which caused this. If the data in Table 4.2 is compared to the graphs in Figure 4.26, it can be seen that in general the bigger the radius of the dot, the less gate voltage needs to be applied to pinch off the channel. This is expected, as a larger QD gate spans more of the mesa channel.

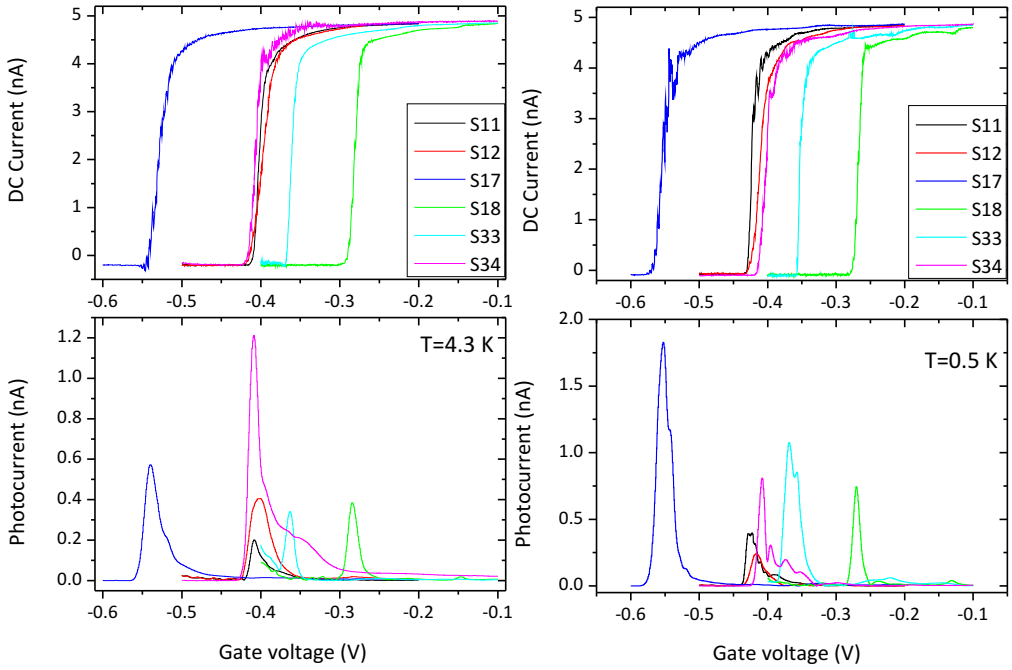

Figure 4.26: Pinch-off and photoresponse graphs of the 3×8 sample for a number of sensors at two temperatures 4.3 K and 0.5 K.

This was generally observed, apart from in sensor S17. This was the second largest dot and it uncharacteristically required the most negative gate voltage to pinch off the channel. This could be the result of a fabrication error resulting in poor coupling between the gate and the 2DEG.

Chapter 5

Terahertz Imaging

5.1 Principle

The imaging experiments carried out in this thesis uses an approach which is similar to that of a simplified charged coupled device (CCD), as found in digital cameras. In this arrangement one can regard a CCD as an array of sensors for which each sensor is an image pixel. CCDs in digital cameras work by picking up the light emitted passively from an object and stores the information as if each pixel was a bucket being filled up for the length of exposure. This draws comparison to exposures on film. Due to the nature of THz radiation, the passively emitted photons can be washed out by the surrounding radiation in this frequency. As well there is radiation emitted by the THz optical system itself. This would all result in the information of the image being lost within the noise, unless some factors were improved to help the signal to noise ratio. For this reason preliminary imaging was carried out in a different manner. The object is placed in the path of an incoming THz light source. Some of the radiation will be absorbed and a shadow-like image will be formed on the device (see Figure 5.1).

Our initial experiments were done by using a single QD-PC sensor, allowing the testing of the sensing technology without the need to be concerned over the

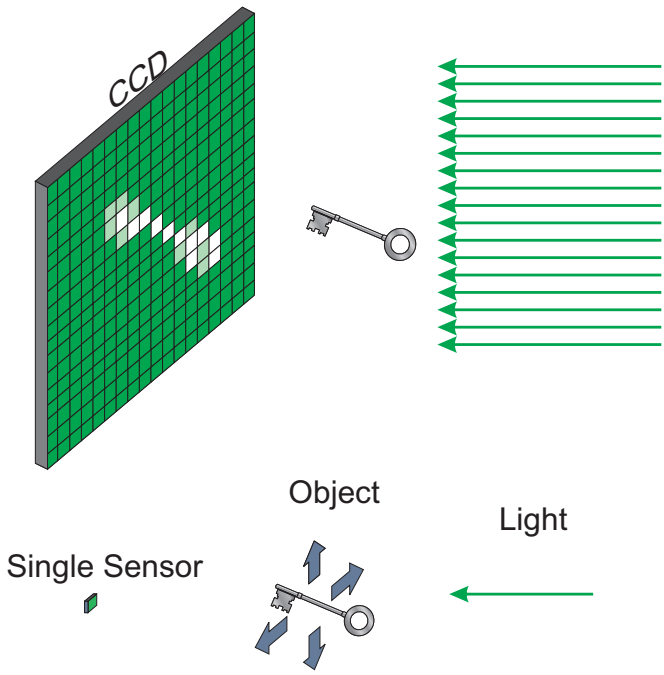

Figure 5.1: Imaging using a simplified CCD (top) and using a single sensor system (bottom).

array technology. For imaging, a single QD sensor and the image of only one pixel at a time would be formed using this standard technique. To capture a whole image we move the object with respect to a fixed QD sensor. This would then provide an image of the whole object. The pixel size of such an imager is dependent on the size of discrete steps the object can take during the scan. For the current arrangement which uses an X-Y stage controlled by a self-written LabVIEW program, the smallest step size is 2.5 μm. Because of the nature of light the resolution of the image is ultimately limited by the wavelength of the radiation. By taking our previous definition of the THz frequency range being between 300 GHz and 3 THz and using the relation between the frequency and wavelength:

$$\lambda = \frac{c}{f} \tag{5.1}$$

we obtain a wavelength range of between 0.1 mm - 1 mm.

5.2 Fridge Adaptation

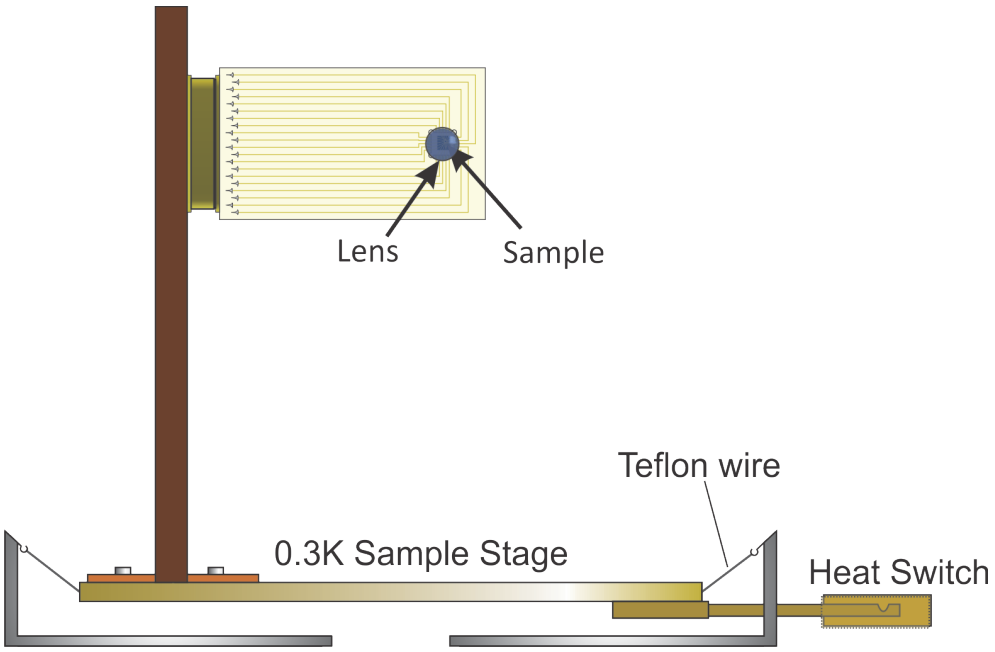

Figure 5.2: Schematic of improved sample holder for external sources, sample is bonded at the focal point of the silicon lens.

The sample holder used for imaging in our first experiment was shown in Figure 3.8. The radiation delivered by the optical system from the room temperature environment is reflected off a mirror onto the sample. Photoresponse was observed but it was difficult to focus the beam onto the sample accurately. We redesigned the holder in such a way that the sample is mounted on the flat side of a semi-spherical lens. The radiation is delivered to the sample from the back side of the wafer. This improves the coupling of the radiation to the sensor antennae (see Figure 5.2). The new design allowed for easier loading of the samples as it was bonded straight onto a PCB which can be plugged into a Cinch conector. This allowed faster swapping of samples and reduced the chance of accidental damage from electrostatic shock or mechanical damage.

5.3 Adjustment of Optical System

The adjustment of the optical system was first carried out using the pyrodetector. The optical system consists of movable X-Y stages and a set of lenses as shown in Figure 5.3. The first imaging was carried out on a pair of metal keys, as the THz radiation should be completely suppressed by the metal and the distinct shape of the object should allow an indication of the achieved resolution. The imaging area is defined by the maximum area the X-Y stage can cover, which was 7×7 cm. The standard resolution used was 300×300 points. This brought about a stepsize of 233 μm which is well below the resolution of the THz radiation, such that the image resolution is not limited by the X-Y stage.

The THz radiation source was provided by an IMPATT diode. The radiation passes through a mechanical chopper running at $\sim$ 30 Hz. The signal from the photo-diode of the chopper is used as the reference frequency for the lock-in amplifier. The light then travels to the first lens, which is used to create a parallel beam directed to the second lens, which is used to focus the beam on the image plane of the X-Y stage. The object being imaged is set at the focal point, giving the greatest resolution possible. After passing through the object, the beam is directed onto the third lens. This is used to recreate the parallel beam, which is then directed to the fourth lens which focusses the beam onto the detector. To calibrate the position of these lenses we used a pyrodetector, as it was a known broadband detector.

The scan was taken at each point by reading the photocurrent. The X-Y stage then moved to the next coordinate in the X plane. Readings were taken at each point until the end of the line was reached. The program then resets the X position and increments the Y position, at which the X plane is scanned again. This procedure is repeated until the whole Y range has been covered in this raster fashion. The drawback to this method compared with having an array of detectors is that the time taken per image can take up to 10 hours, which

is long considering that temperature fluctuations of not only the fridge but the imaged object can greatly affect THz measurements.

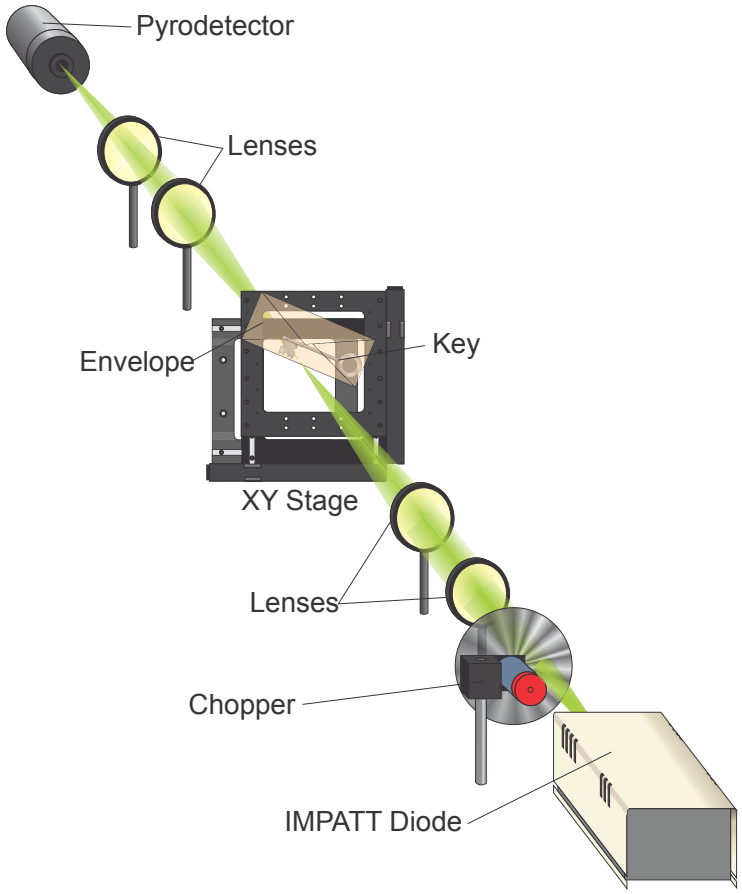

Figure 5.3: Schematic of optical layout of imaging system, all objects lie flat on an optical bench.

Figure 5.4 shows the resulting images, where the shape of keys can clearly be identified. There also appears to be slight interference patterns which are most likely a result of diffraction around the object. We used a 170 GHz IMPATT diode with a power of $\sim$ 300 pW as a THz source. The expected wavelength limited resolution would be 1.8 mm with this radiation frequency. A resolution of $\sim$ 2 mm is seen in the image.

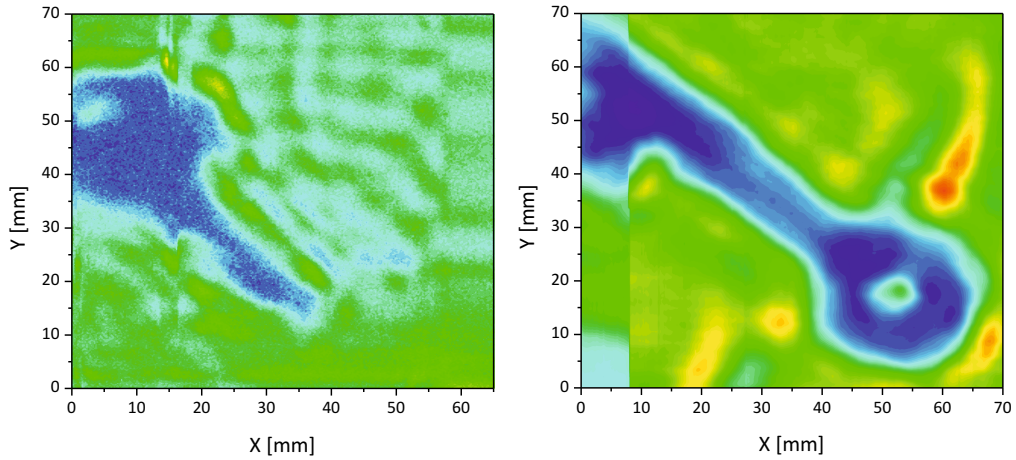

Figure 5.4: THz image of the metal keys taken with the pyrodetector. Left: Yale key; Right: Chubb key.

Once the system was confirmed to work with the pyrodetector the system was set up to operate with the QD-PC sensor. For calibration purposes two metallic gratings and two paperclips were imaged (Figure 5.5). The metallic gratings were 30 mm in diameter with two hole sizes: 3 mm and 1mm diameter. The same setup and procedure were used to obtain these images.

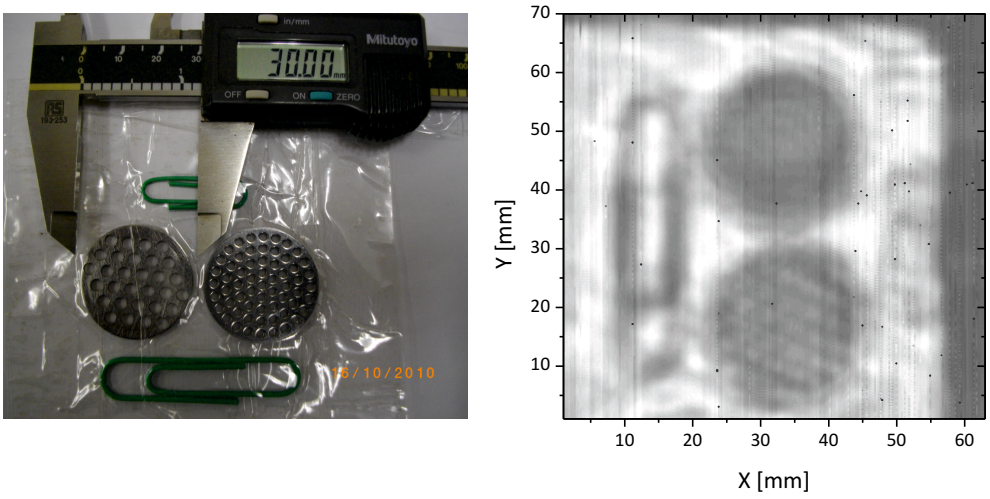

Figure 5.5: Photograph and resulting THz image of metallic objects. A QD-PC sensor was used.

As Figure 5.5 shows, the 3 mm holes were resolved whilst the 1 mm ones were not. This is as expected, being that the fundamental limit for resolution is

1.8 mm for this wavelength. A cross section taken at 40 mm along the X axis (Figure 5.6) shows a clear view of the holes being resolved in the region between 5 and 25 mm along the Y axis for the 3 mm holes. However, for the 1 mm holes (between 35 and 55 mm along the Y axis), an increase in THz radiation can be seen towards the centre of the disc but the position of the holes are not visible as clearly resolved peaks.

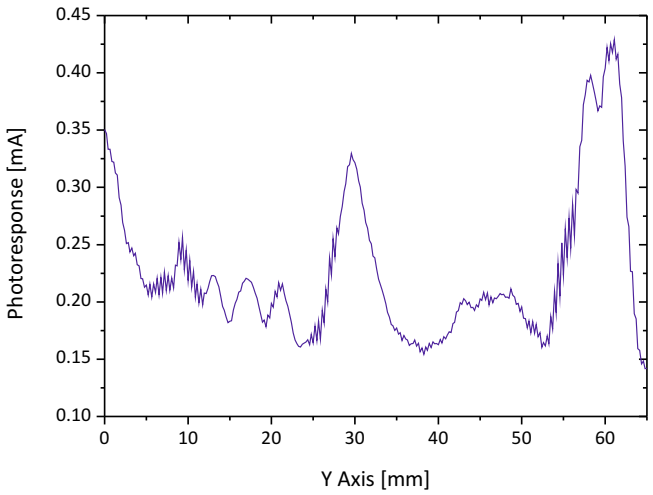

Figure 5.6: Cross section of image of gratings shown in Figure 5.5.

Also shown in Figure 5.5 are two paperclips. The larger one is clearly resolved while the smaller one, although visible, is unclear. The dark region around the far edge, greater than 55 mm, is the edge of the X-Y stage which is visible as a clean edge.

5.4 Imaging of Leaves

The aim of the experiments described in Chapter 3 was to characterise the QD-PC sensors and emitters in order to use them in a terahertz imaging setup, which has itself been tested on metallic objects. As a step towards real applications in terahertz scanners for passive imaging of people in airports, say, as detailed in Section 1.1, the choice was made to image leaves, being biological samples. In

this section, results are presented from various leaf samples and configurations that were imaged using this setup.

5.4.1 Imaging of an Ivy leaf taken through Paper

Once the optical setup was adjusted using the metallic samples as described in Section 5.3 they were replaced with a leaf sample in a configuration that is detailed in the subsequent sections. In this first experiment, an ivy leaf enclosed in an envelope was imaged. Figure 5.7 is a schematic diagram showing the imaging setup with the cryogen free fridge and the ivy leaf in an envelope measured. The source is also depicted, in this instance a BWO was used. The mesa of the sensor was connected to the external electronics via the pin matrix. In this way, 24 electrical lines into the fridge can be connected to different electronic equipment at room temperature, depending on the pin arrangement. The electronic instruments used were connected as in Figure 3.12.

To characterise the detector, a negative bias was applied to the gates in order to check that pinch-off occurred. The photocurrent was detected close to pinch-off using the lock-in technique. In order to find the optimum bias position, the negative bias on the gate was increased, until a maximum was found in the photoresponse. At this bias, fine adjustments to the alignment of the emitter and lenses are made to increase the signal on the lock-in amplifier.

The phase of the lock-in was adjusted so that all the signal was in the x channel and the X-Y stage was reset to the start position at the top right corner. This is the equivalent of the bottom left corner of the object being imaged first.

A LabVIEW program was written to both control the X-Y stage and take the voltage measurement from the lock-in amplifier via a Keithley multimeter. This program was started and the image is obtained in a raster fashion as described in Section 5.3.

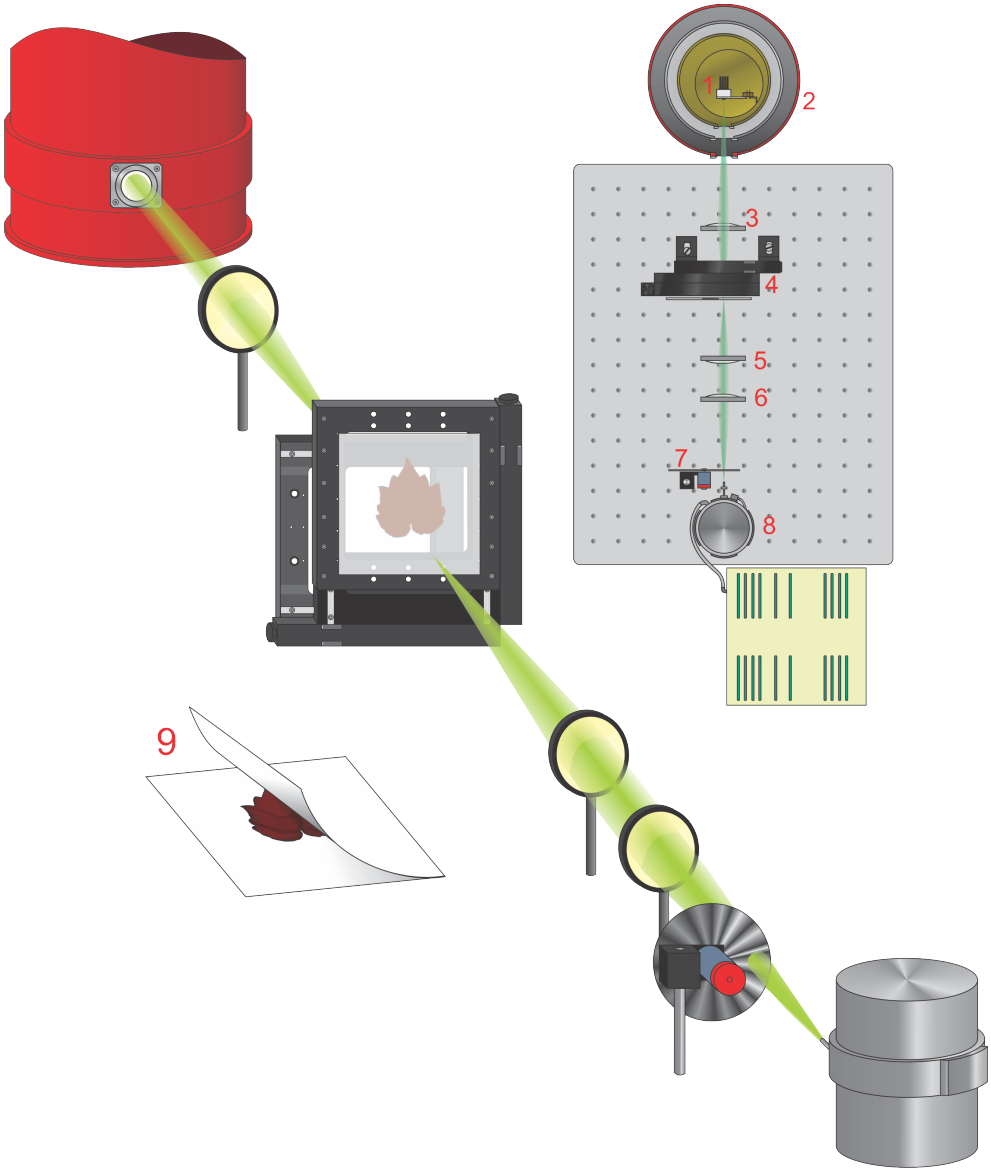

Figure 5.7: Schematic showing two perspectives of the imaging setup. The aerial view perspective shows labels of the individual components of the system: 1) Sensor mounted on the experimental stage. 2) The cryogen free fridge. 3) Lens used to focus beam onto the detector's lens. 4) X-Y stage used to translate object to be imaged through the focussed THz beam. As can be seen in the 3D perspective the leaf is mounted to this stage using paper, which encloses the whole leaf, shown by 9. 5) Lens used to focus beam on sample. 6) Lens used to make parallel beam from source. 7) Chopper whose frequency is linked to the lock-in as the reference frequency. 8) Source of radiation, in this instance a BWO, but this was exchanged for other sources such as the Gunn diode for subsequent experiments.

The image obtained is shown in Figure 5.8. The BWO was set to 568 GHz, which has an estimated power of 50 μW. The image of the leaf in this situation would be dependent on the water content, as the water absorbs THz radiation. The paper does not absorb THz radiation and so the leaf is visible in the image.

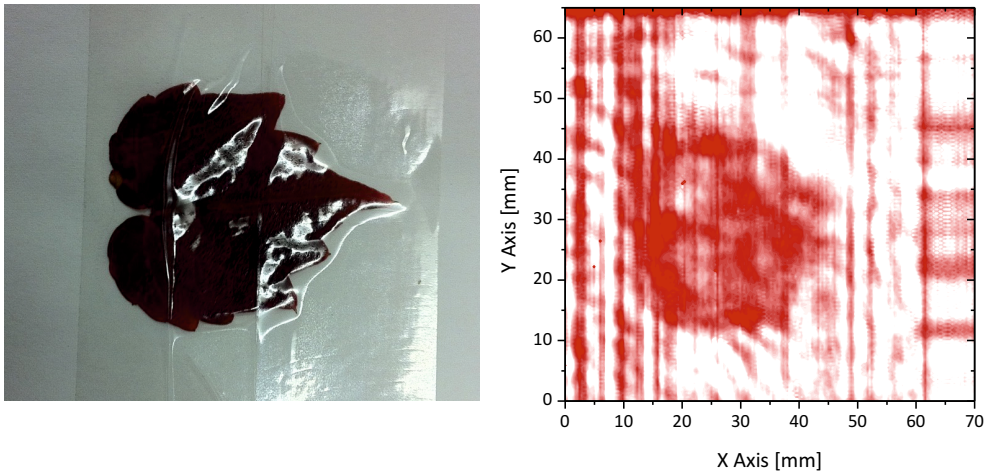

Figure 5.8: Image of leaf taken with BWO. The leaf was enclosed in paper blocking visible light, but transparent to THz radiation.

As can be seen in Figure 5.8, it is possible to image the water content of objects through barriers which are not visible in the optical range but are transparent to THz radiation. This shows potential as a possible technique for imaging in security applications to image substances which absorb THz radiation such as metal objects or water solutions, behind clothes and within bags, which would be transparent to THz.

5.4.2 Imaging of an Ivy Leaf taken through Plastic

We use a Gunn diode of 170 GHz frequency to image a similar leaf wrapped in Sellotape. This was done in order to keep the moisture content of the leaf constant as the scan was long in duration. In order to prevent the sample from receiving too much heat load from the emitter, adjustments to the attenuator were made

giving an output of the emitter of 1 mW. The sensor used was a simple quantum point contact (QPC09) which consisted of a mesa channel and a cross gate which is used to pinch-off the channel. When the device is subject to THz radiation with the cross gate biased just below the point of pinch-off, a 'photoinduced' voltage is measured across the channel. This photovoltage is plotted against the two axes of the scan (X, Y) and can be seen in Figure 5.9.

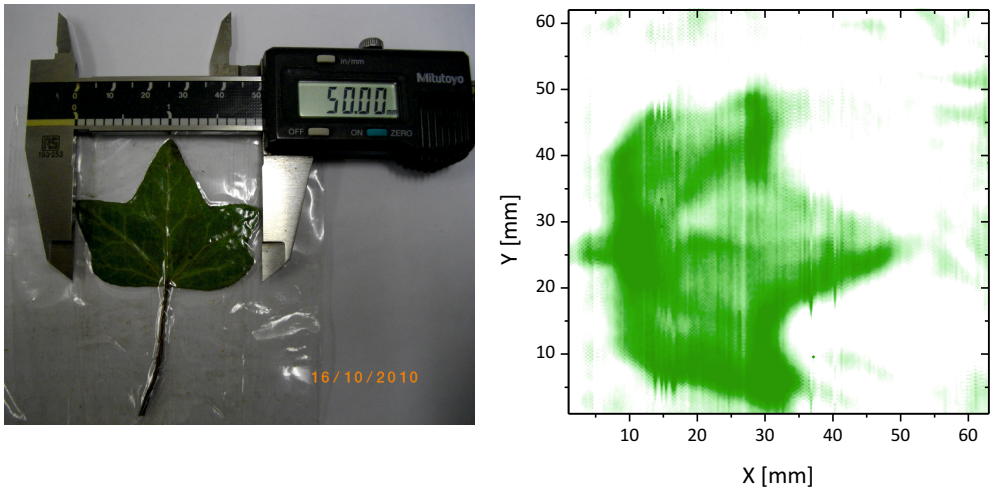

Figure 5.9: Left: Photograph of leaf showing the actual size. Right: Graph of leaf using a 170 GHz Gunn diode.

5.4.3 Imaging of an Ivy Leaf using a Quantum Dot Array Sensor

A Quantum Dot array sensor (QDA10) was added to the fridge. The sensor was an array of 2×7 sensors consisting of double quantum dot gates, allowing one of the dots to act as a PC. Under external THz radiation, it was observed just before pinch-off, that there was a 'photoinduced' change of current through the mesa, as seen in other samples. A freshly cut ivy leaf was placed in between two 1 cm thick slabs of polystyrene, as polystyrene is transparent to terahertz, allowing the filtering of other frequencies including any optical frequencies that

may be present. Two holes of 5 mm in diameter were punched into the leaf to give an idea of the lateral resolution, as shown in Figure 5.10.

Figure 5.10: Left: Photograph of a leaf mounted onto a polystyrene slab, showing the position of the hole-punches. Right: The leaf during a scan, where it was completely hidden with a second layer of polystyrene.

The leaf was scanned with the sensor at two different temperatures, firstly at 3.2K and then at 0.4K. It was expected that the scan with the sensor at the lower temperature should show the greatest response, but as seen in Figure 5.11 it is clear that this did not turn out to be the case for this scan. Figure 5.12 shows a cross section of the image for each scan, showing the difference in response more clearly. There are a few reasons why this may be the case. Firstly the operation point of the QD array sensor may have drifted over the many hours it took to capture the two images. This would mean the sensitivity of the sensor was lower than optimal. Secondly the alignment of the optical system may have been altered, as its is very sensitive and any slight movement of any part of it could result in a dramatic loss of signal strength. This would also affect the performance of the system by slightly defocussing the lenses. Lastly the temperature of the sensor could have been different. However, looking at Figure 5.12 we can see that the noise levels are higher in the 3.2 K scan compared to the 0.4 K scan, distinguishing the two sensor temperatures.

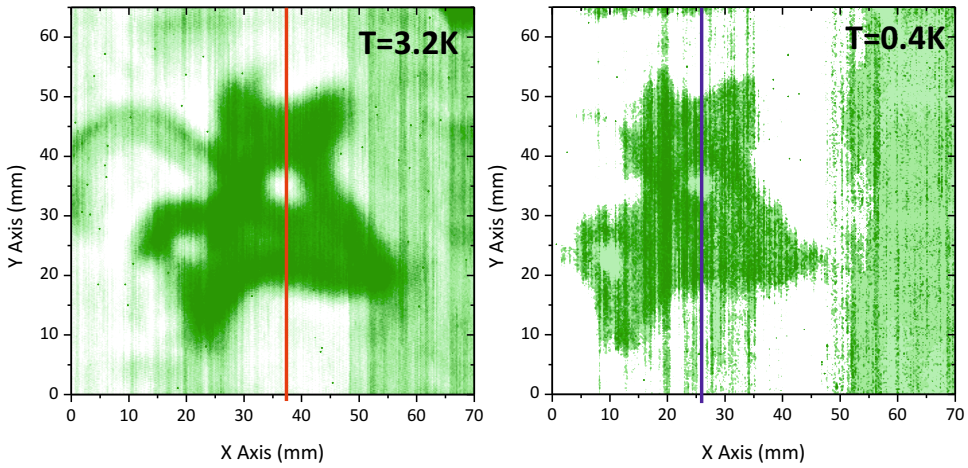

Figure 5.11: Two images of a leaf with two holes punched in, taken with Gunn diode. Leaves were encased in polystyrene blocks. One scan was taken with the detector at 3.2 K the other was at 0.4 K. The red and blue lines show where the cross sections are taken for Figure 5.12.

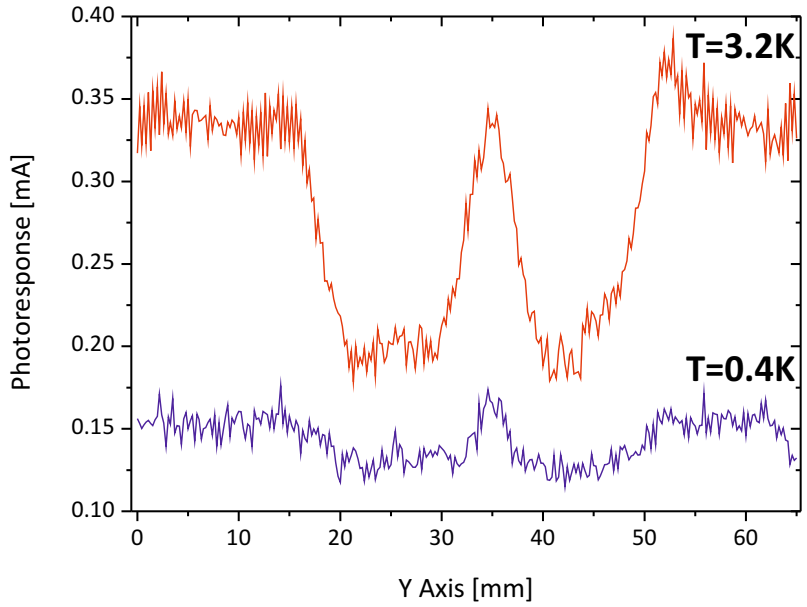

Figure 5.12: Cross section of photoresponse taken at two different temperatures.

An image of a leaf was also taken with a QD-PC sensor from a 3×8 array.

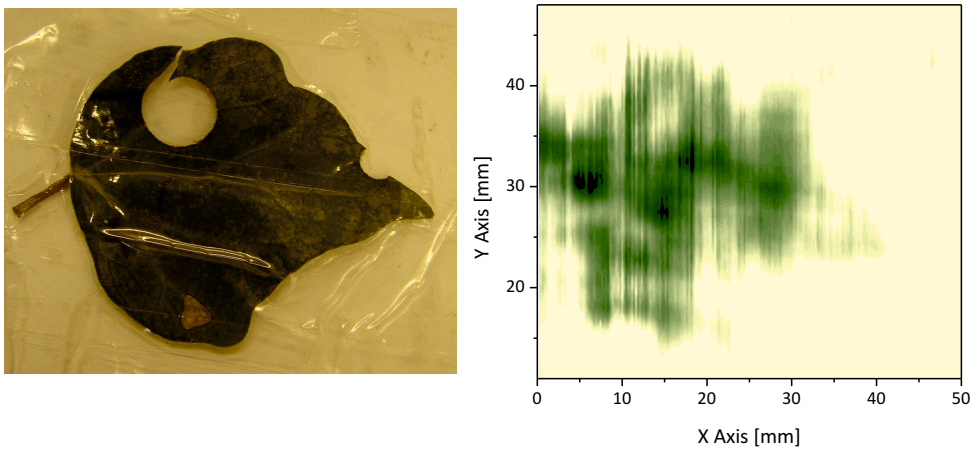

Figure 5.13: Image of leaf taken with Array

As Figure 5.13 shows, the image was achieved but the resolution was not as good as previous images taken by the 2×7 array. This implies that improvements in fabrication need to be implemented in this new array design.

Chapter 6

Conclusions and Future Work

The detection of terahertz radiation has a vast number of potential applications. Its non-ionising nature makes it appealing in the health screening sector and its penetration properties for different materials justify the development of THz detectors in security imaging. The project described in this thesis was to investigate the use of quantum dot based THz detectors held at cryogenic temperatures as a method for detecting THz radiation at room temperature, primarily for imaging applications with the future intention of spectroscopic measurements. A VeriCold cryogen free pulse tube refrigerator provided a conceivable platform to address maintenance, cost and safety issues when operating cryogenic detectors as a step towards real-world applications. Using the in-built control system, cooling from room temperature to the base temperature of the 4 K platform was possible in 24 hours, with further cooling down to 300 mK available using the ADR.

The experimental setup initially suffered from a high level of noise, which made the operation of the SETs difficult, due to their sensitive nature. This noise was attributed to high frequency electromagnetic noise in the electrical leads running into the fridge, prompting an investigation into the filtering of these lines. Copper powder filters were consequently made, which resulted in the desired reduction in noise - so much so that it enabled fine features in the I-V characteristic of the SET

to be seen. A range of THz sources were used in this work that were characterised using a home-built Fourier transmission spectroscopy system, providing a known source in the terahertz range.

Two main readout designs of the QD detector were investigated in this thesis, the QD-SET and QD-PC sensors. For the QD-SET sensors, the current through the SET probes the electrochemical charge state of the QD through capacitive coupling. The fragile nature of the SET part of the device was evident as the number that survived the cooldown process was often less than 50%. These were checked to be operational and characterised by plotting a conductance map of the SET as a function of bias and gate voltages. The formation of the quantum dot was indicated by an increase in both the frequency and amplitude of the Coulomb blockade oscillations through the SET as the QD gate voltage was decreased. The bias position where the QD is at the point of formation (pinch-off) was verified to be the most sensitive region for detecting a photoresponse, despite the accompanying increase in the dark count. However, the nature of SET detection of the QD state is inherently digital. This makes very sensitive single photon detection possible but for a large photon flux, it is limited by the time constant of switching events.

A more reliable and simpler alternative to SET readout is a QD-PC sensor. With this readout method, the point contact is used to limit the current through the mesa near the QD, close to the point of pinch-off. The electrochemical charge state of the QD then directly affects the conductance through the mesa through capacitive coupling to the PC. As this detector operates using robust gold gates, nanofabrication is significantly simpler, increasing the survival rate after cooldown. The PC was characterised by measuring the pinch-off of the channel as a function of PC and QD gate voltages. This enables the gate voltages of the sensor to be set for optimum sensitivity, just before the channel is pinched off and just after the formation of the QD. An asymmetry in the gradient of the pinch-off

boundary of the PC was observed and was explained by the relative positions and resulting capacitive coupling of the conductance channel to the QD and PC gates. Unexpected oscillations in the PC current during pinch-off reminiscent of CBOs were observed and investigated in some of the devices. Through the measurement and analysis of stability diagrams it was concluded that these oscillations originated from the presence of a small QD in the conductance channel of diameter $\sim 100\,\text{nm}$, possibly caused by a single impurity atom in the channel.

A clear photoresponse of the QD-PC sensor was measured using a lock-in technique, with the terahertz source chopped at a reference frequency. The photoresponse was measured as a function of QD gate voltage and was verified to be largest at the point of pinch-off of the PC. Furthermore, it was found that a larger photoresponse is observed with increasing terahertz flux but at large emitter powers the performance of the sensor is impaired due to increased heating, causing a decrease in photoresponse. The QD-PC sensor was shown to be operational up to at least 3.5 K. This is an improvement on the QD-SET sensors, where the SET operation temperature is limited by the charging energy to below 1 K. This is limited by current nanofabrication techniques. The QD-PC sensor has no such limitations, relaxing the need for refrigeration to lower temperatures.

Arrays of QD-PC sensors with 3 rows of 8 sensors with differing QD sizes were also tested, as the range of QD sizes enables spectroscopic THz detection. Quantum dots of dimensions $1.15\,\mu\text{m} - 3.95\,\mu\text{m}$ corresponding to detection frequencies of $0.38\,\text{THz} - 0.21\,\text{THz}$ were tested. After cooldown there was a 25% survival rate of the sensors, due to the complexity of the design. Photoresponse and pinch-off were observed with these sensors, but unfortunately a measurement of its precise spectroscopic performance was not completed.

Following the successful photoresponse measured using the single QD-PC sensors, the imaging of various metallic objects was successfully performed with a lateral resolution of approximately 2 mm. This is comparable to the wavelength

of the THz radiation used, which was 1.8 mm. An optical bench was used to align the THz source, lenses and a LabVIEW controlled X-Y stage which held the object to be imaged, with the QD-PC sensor in the fridge. The sample holder for the sensor was improved by adding a semi-spherical lens to improve the focus of the radiation source onto the sensor. THz images of leaves were obtained through materials that block visible light, namely plastic, paper and polystyrene, showing the potential for these QD sensors in security scanning applications. A sensor from a QD-PC array at 3.5 K was also used to successfully image an ivy leaf through two 1 cm thick slabs of polystyrene.

The QD-SET definitely has the potential for higher sensitivity, with the ability to detect charge exitations of the QD with an accuracy of less than one electron. The QD-PC has shown that a clear photoresponse is possible, despite only being able to detect charge excitations of a few electrons. But, with the added ability to exhibit this response at temperatures as high as 3.5 K as well as its considerably simpler fabrication, the QD-PC is a valid method for readout of plasmon based QD excitations.

6.1 Future Work

With the aim of a passive imaging system in mind, one has to consider the feasability of being able to detect an object external to the fridge, under its own illumination. Being in the THz frequency range the incident radiation at the fridge is awash with other backgound radiation from not only the background enviroment but the windows of the fridge itself. In order to improve the chances of better detection it was proposed that an 'active matrix' could be developed to amplify the image plane in the THz region. One way to do this is to use a heterostructure of a quantum cascade laser. This could provide an increase in flux due to the amplification of one particular frequency. However, this would reduce the number of applications for the system as wide band spectroscopy measurements would be lost.

A graphene detector has also been devised and tested in the current imaging setup. It is proposed as an alternative to the QD based detector but tests so far have shown the QD based sensors to have a much higher sensitivity.

Part I

Appendix

Appendix A

Fourier Transform Spectroscopy

Since its creation, most interferometer designs have incorporated some element of a basic Michelson interferometer, shown schematically in Figure A.1. Both beams have been transmitted once and reflected once as they are divided at the beamsplitter, then reflected at either the movable (M1) or fixed (M2) mirror, and finally recombined at the beam splitter to proceed to the sample area and the detector.

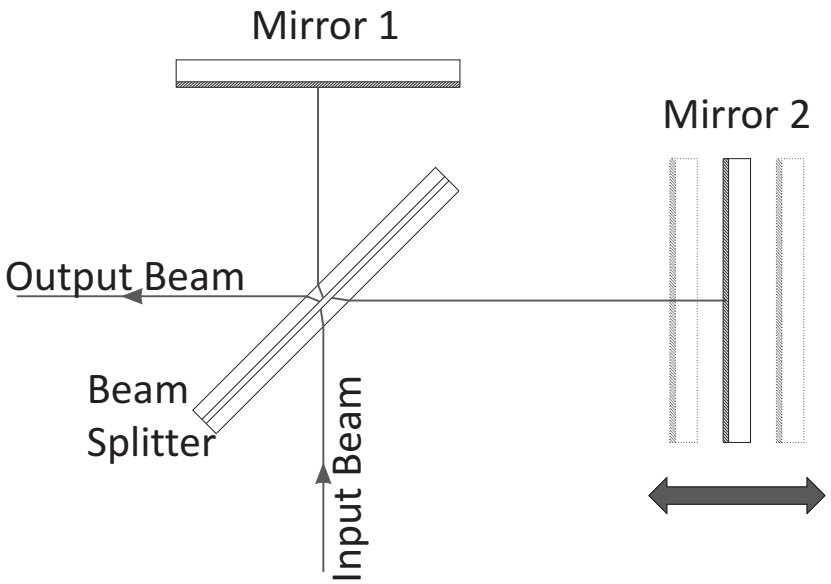

Figure A.1: Schematic of a Michelson interferometer.

Consider an incoming monochromatic plane wave with an average electric field

amplitude E_m, frequency ω and wave number $\bar{\nu}$ (which as units of cm^{-1}):

$$\bar{\nu} = \frac{1}{\lambda} = \frac{\omega}{2\pi c} \tag{A.1}$$

incident on the beam splitter, where c is the speed of light and the wavelength λ is in cm.

$$\overrightarrow{E} = \vec{E}_m cos(\omega t - 2\pi\bar{\nu}y) \tag{A.2}$$

The beam from the mirror M2 after leaving the beam splitter may be written as:

$$\vec{E_2} = rtc\vec{E}_m cos[\omega t - 2\pi\bar{\nu}y_1] \tag{A.3}$$

where r is the reflectance amplitude of the beam splitter, t is the transmittance, and c is a constant depending on the polarisation. Similarly from the other mirror M1, at the same point we have:

$$\vec{E_1} = rtc\vec{E}_m cos[\omega t - 2\pi\bar{\nu}(y_1 + x)] \tag{A.4}$$

where x is the path difference. By superposition, the resultant E is given by

$$\vec{E_R} = E_1 + E_2 = 2rtc\vec{E}_m cos[\omega t - 2\pi\bar{\nu}(y_1 - \frac{x}{2})] \tag{A.5}$$

The intensity (I) detected is the time average of E^2. More strictly $\vec{E} \times \vec{H}$ (the Poynting vector), but because $|\vec{E}| \propto |\vec{H}|$ this quantity can be described simply by just $|\vec{E}|$, neglecting some constant of proportionality (which is not important). The intensity may be written as:

$$I \propto 4r^2t^2c^2E_m^2 cos^2[\omega t - 2\pi\bar{\nu}(y_1 - \frac{x}{2})] \tag{A.6}$$

where the time average of the first cosine term is just 1/2. Thus

$$I \propto 2I(\bar{\nu})cos^2(\pi\bar{\nu}x) \tag{A.7}$$

where $I(\bar{\nu})$ is a constant that depends only upon $\bar{\nu}$. This expression may be simplified to

$$I(x) = I(\bar{\nu})[1 + cos(2\pi\bar{\nu}x)] \tag{A.8}$$

where $I(x)$ is the $interferogram$ from a monochromatic source. The interferogram for a monochromatic source is shown in Figure A.2.

$$I(x) = \int_0^{\bar{\nu}m} I(\bar{\nu})[1 + cos(2\pi\bar{\nu}x)]d\bar{\nu}$$

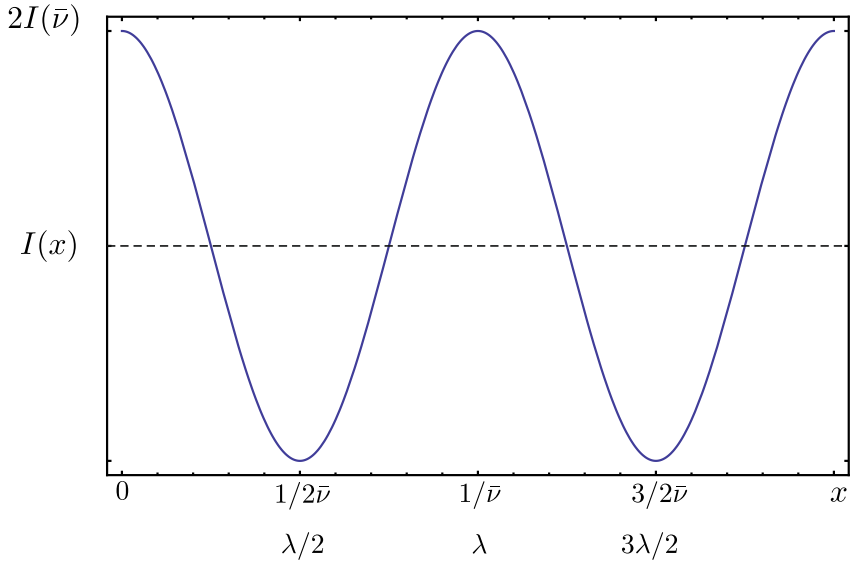

Figure A.2: The interference pattern for a monochromatic source (such as a laser) as a function of mirror displacement.

A.1 Polychromatic source

One of the advantages of the Fourier transform instrument is that many different frequencies may be looked at simultaneously — all the information is gathered at the same time, and it can be analysed later using a Fourier transform. This decreases the measurement time. An interferogram for a polychromatic source which consists of frequencies from $0 \rightarrow \bar{\nu_m}$ is thus:

$$= \int_0^{\bar{\nu}m} I(\bar{\nu})d\bar{\nu} + \int_0^{\bar{\nu}m} I(\bar{\nu})cos(2\pi\bar{\nu}x)d\bar{\nu} \tag{A.9}$$

When $x = 0$ then

$$I(0) = 2\int_0^{\bar{\nu}m} I(\bar{\nu})d\bar{\nu}$$

$$\Rightarrow I(x) = \frac{1}{2}I(0) + \int_0^{\bar{\nu}m} I(\bar{\nu})cos(2\pi\bar{\nu}x)d\bar{\nu} \tag{A.10}$$

With many different wavelengths present, the interferogram resembles the diagram in Figure A.3, which is symmetrical about $x = 0$ for an ideal interferogram.

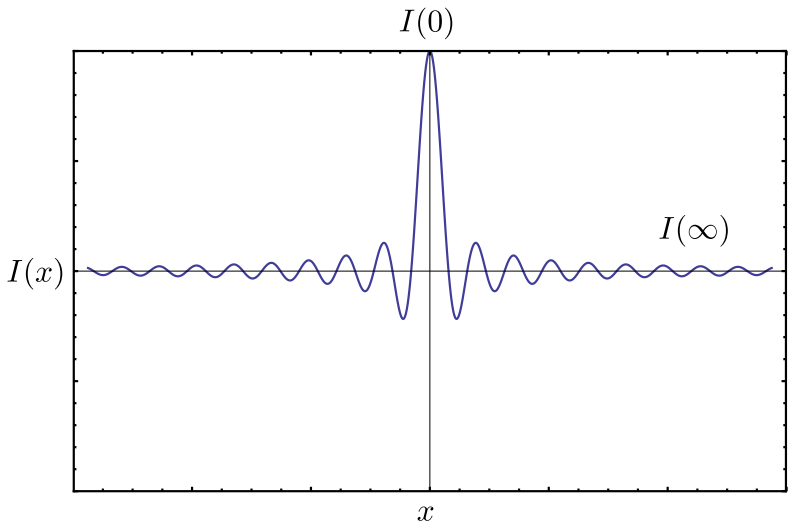

Figure A.3: The interference pattern for a polychromatic source about the zero path difference. This curve was generated simply by taking the normalised sum of a number of cosine functions with various frequencies.

When $x = 0$ the interference between all of the frequencies is constructive, resulting in a central maxima. However, for $x = \infty$ the frequencies add both constructive and destructively, so that the net contribution due to the integral in Equation A.10 is simply zero. Thus,

$$I(\infty) = \frac{1}{2} I(0) \tag{A.11}$$

or more simply, $I(0) = 2I(\infty)$. This relationship is an important check of the instrument alignment.

Percentage modulation

The percentage of modulation is defined as

$$\frac{[I(0) - I(\infty)]}{I(\infty)} \times 100 \tag{A.12}$$

In a well-aligned instrument, the modulation is $> 85\%$, and this value should be $> 95\%$ in the low frequency region.

A.2 Fourier transform

We have $I(x)$ and now want $I(\bar{\nu})$, i.e.:

$$I(x) - I(\infty) = \int_0^{\bar{\nu}m} I(\bar{\nu}) cos(2\pi\bar{\nu}x) d\bar{\nu} \tag{A.13}$$

letting $\bar{\nu}_m \to \infty$, we can write

$$I(\bar{\nu}) = \int_0^{\bar{\nu}m} [I(x) - I(\infty)] cos(2\pi\bar{\nu}x) dx \tag{A.14}$$

This procedure involves sampling each position, which can take a long time if the signal is small and the number of frequencies being sampled is large [70, 84**?** , 85].

Bibliography

[1] TeraView promotional material. TeraView Ltd, St John's Innovation Park, Cowley Road, Cambridge, CB4 0WS.

[2] The University of Texas. The University of Texas at Austin, 1 University Station, Austin, Texas 78712.

[3] Komiyama, S., Astafiev, O., Antonov, V., Kutsuwa, T. & Hirai, H. A single-photon detector in the far-infrared range. *Nature* **403** (2000).

[4] Ozyuzer, L. *et al.* Emission of coherent thz radiation from superconductors. *Science* **318**, 1291–1293 (2007).

[5] Leahy-Hoppa, M., Fitch, M., Hayden, L. & Osiander, R. Wideband terahertz spectroscopy of explosives. *Chemical Physics Letters* 227–230 (2007).

[6] Chen, J., Chen, Y., Hongwei, Z., Bastiaans, J. & Zhang, X. Absorption coefficients of selected explosives and related compounds in the range of 0.1-2.8 THz. *Optical Society of America* (2007).

[7] Ferguson, B. & Zhang, X. Materials for terahertz science and technology. *Nature Materials* **1** (2002).

[8] Zhang, X. & Pengyu, H. Time-domain spectroscopy targets the far-infrared. *Laser Focus World* **36** (2000).

[9] Jiang, Z. & Zhang, X.-C. Terahertz imaging via electrooptic effect. *Microwave Theory and Techniques, IEEE Transactions on* **47**, 2644 –2650 (1999).

[10] Wu, Q. & Zhang, X.-C. Design and characterization of traveling-wave electrooptic terahertz sensors. *Selected Topics in Quantum Electronics, IEEE Journal of* **2**, 693 –700 (1996).

[11] Liu, H.-B., Zhong, H., Karpowicz, N., Chen, Y. & Zhang, X.-C. Terahertz spectroscopy and imaging for defense and security applications. *Proceedings of the IEEE* **95**, 1514 –1527 (2007).

[12] Rensselaer Research Review Spring 2006 (2006).

[13] Nason, S. The Next Wave. *Rensselaer* (2003).

[14] The University of Adelade. North Terrace, Adelade, South Australia, 5005.

[15] Biography of Sir Charles Wheatstone, The Hebrew University of Jerusalem. Institute of Chemistry, The Hebrew University of Jerusalem, Jeruselam, 91904, Israel.

[16] NASA Earth Observatory. The Bolometer, Feature Articles, NASA Earth Observatory.

[17] http://www.hao.ucar.edu/education/bios/langley.html.

[18] The University of Aberdeen. The University of Aberdeen, King's College, Aberdeen, AB24 3FX.

[19] Jet Propulsion Laboratory. Infrared Astronomy Timeline, CoolCosmos, Jet Propulsion Laboratory, California Institute of Technology.

[20] High Altitude Obervatory. High Altitude Observatory, Boulder, CO 80301.

[21] Langley, S. *Annals of the Astrophysical Observatory of the Smithsonian Institution* (Smithsonian, 1900).

[22] Walcot, C. *Biographical Memoir of Samuel Pierpont Langley 1834-1906* (National Academy of Science, 1912).

[23] Sonoma state university. Www.phys-astro.sonoma.edu/brucemedalists/low/index.html, The Department of Physics and Astronomy, Sonoma State University, CA 94928.

[24] Morris, J. & Shen, Y. Far-infrared generation by picosecond pulses in electro-optical materials. *Optics Communications* 81 – 84 (1971).

[25] Mitra, S. & Nudeleman, S. *Far-infrared properties of solids* (Plenum, 1970).

[26] Gol'tsman, G. N., Okunev, O., Chulkova, G., Lipatov, A. & Semenov, A. Picosecond superconducting single-photon optical detector. *Applied Physics Letters* (2001).

[27] University of Heidelberg. Astronomisches Rechen-Institut, Moenchhofstr. 12-14, 69120 Heidelberg Germany.

[28] Anghel, D. & Kuzmin, L. Capacitively coupled hot-electron nanobolometer as far-infrared photon counter. *Applied Physics Letters* **82** (2009).

[29] Anghel, D. & Kuzmin, L. Capacitively coupled hot-electron nanobolometer as far-infrared photon counter. *Applied Physics Letters* **82** (2003).

[30] Nahum, M. & Martinis, J. Hot-electron microcalorimeters as high-resolution x-ray detectors. *Applied Physics Letters* **66** (1995).

[31] Stuivinga, M., Ham, C. L. G., Klapwijk, T. M. & Mooij, J. E. Phase-slip centers in superconducting aluminum strips. *Journal of Low Temperature Physics* **53**, 633–671 (1983).

[32] Semenov, A. D., Gol'tsman, G. N. & Korneev, A. A. . *Physica C* **351** (2001).

[33] I. Physikalisches Institut. I. Physikalisches Institut, Universitat zu Koln, Zulpicher Strasse 77, 50937 Koln.

[34] Benford, D. J. *et al.* A Planar Two-Dimensional Superconducting Bolometer Array for Millimeter Astronomy. *American Astronomical Society Meeting* **207** (2006).

[35] May, T., Zakosarenko, V., Boucher, R., Kreysa, E. & Meyer, H.-G. Superconducting bolometer array with SQUID readout for submillimetre wavelength detection. *Superconductor Science and Technology* **16** (2003).

[36] Wilms Floet, D., Miedema, E., Klapwijk, T. & Gao, J. Hotspot mixing: A framework for heterodyne mixing in superconducting hot-electron bolometers. *Applied Physics Letters* **74**, 433–435 (1999).

[37] Berkeley bolometers. Berkeley Bolometers, Berkeley University of California.

[38] The University of Chicago. Department of Astronomy and Astrophysics.

[39] Kouwenhoven, L., Hekking, F., Wees, B. V. & C. Transport through a Finite One Dimentional Crystal. *Physical review letters* (1990).

[40] Wasilewski, Z. R. *et al.* Composition of AlGaAs. *Journal of Applied Physics* **81**, 1683–1694 (1997).

[41] van Wees, B. J. *et al.* Quantum ballistic and adiabatic electron transport studied with quantum point contacts. *Phys. Rev. B* **43**, 12431–12453 (1991).

[42] Chen, L. H. *et al.* Charge-imaging field-effect transistor **79**, 1202–1204 (2001).

[43] Ko, K. K., Berg, E. W. & Pang, S. W. Effects of etch-induced damage on the electrical characteristics of in-plane gated quantum wire transistors. *Journal of Vacuum Science Technology B: Microelectronics and Nanometer Structures* **14**, 3663 –3667 (1996).

[44] Kurdak, C., Farina, L. & Lewis, K. M. Quantum point contact transistor with high gain and charge sensitivity **89**, 3453–3457 (2001).

[45] Li, Y. P., Tsui, D. C., Heremans, J. J., Simmons, J. A. & Weimann, G. W. Low frequency noise in transport through quantum point contacts **57**, 774–776 (1990).

[46] Sakamoto, T., Nakamura, Y. & Nakamura, K. Distributions of single carrier traps in gaas/$al_xga_{1-x}as$ heterostructures **67**, 2220–2222 (1995).

[47] Dekker, C. *et al.* Spontaneous resistance switching and low-frequency noise in quantum point contacts. *Phys. Rev. Lett.* **66** (1991).

[48] Kurdak, C. *et al.* Resistance fluctuations in gaas/$\mathrm{al}_x\mathrm{ga}_{1-x}$as quantum point contact and hall bar structures. *Phys. Rev. B* **56** (1997).

[49] Field, M. *et al.* Measurements of coulomb blockade with a noninvasive voltage probe. *Phys. Rev. Lett.* **70**, 1311–1314 (1993).

[50] Jacak, L., Hawrylak, P. & Wojs, A. *Quantum Dots* (Springer, 1998).

[51] Chakraborty, T. *Quantum dots: a survey of the properties of artificial atoms* (Elsevier, 1999).

[52] Fetter, A. L. Magnetoplasmons in a two-dimensional electron fluid: Disk geometry. *Phys. Rev. B* **33**, 5221–5227 (1986).

[53] Landau, L. & Liftshits, E. *Electrodynamics of Continuos Media 2nd edn* (Pergamon Press, Oxford, 1963).

[54] Bird, J. P. *Electron Transport in Quantum Dots* (Kluwer Academic Publishers, 2003).

[55] Kolesov, R., Grotz, B., Balasubramanian, G., Stohr, R. & Nicolet, A. Wave particle duality of single surface plasmon polaritons. *Nature* **470** (2009).

[56] Heinzel, T. *Mesoscopic electronics in solid state nanostructures* (Wiley, 2007).

[57] Colinge, J.-P. & Colinge, C. A. *Physics of semiconductor devices* (Birkhauser, 2006).

[58] Wasshuber, C. *Computational single-electronics* (Springer, 2001).

[59] Simkins, L. Ph.D. thesis.

[60] Hook, J. & Hall, H. *Solid State Physics* (Wiley, 2003).

[61] Fitzgerald, R., Pohlen, S. & Tinkham, M. Observation of Andreev reflection in all-superconducting single-electron transistor. *Physical Review B* **57** (1998).

[62] Pohlen, S., Fitzgerald, R. & Tinkham, M. The Josephson-quasiparticle (JQP) current cycle in the superconducting single-electron transistor. *Physica B* (2000).

[63] Leppakangas, J., Thuneberg, E., Lindell, R. & Hakonen, P. Tunneling of Cooper pairs across voltage-biased asymetric single-Cooper-pair transistors. *Physical Review B* **74** (2006).

[64] Ingold, G. & Grabert, H. Cooper-pair curent through ultrasmall Josephson junctions. *Physical Review B* **50** (1994).

[65] Kim, D. M. *Introductory Quantum Mechanics for Semiconductor Nanotechnology* (Wiley-VCH, 2010).

[66] The university of Warwick. Physics Department.

[67] Hashiba, H. *et al.* Isolated quantum dot in application to terahertz photon counting. *Phys Rev B* **73** (2006).

[68] Kleiner, R., Steinmeyer, F., Kunkel, G. & Müller, P. Intrinsic Josephson effects in $bi_2sr_2cacu_2o_8$ single crystals. *Phys. Rev. Lett.* **68**, 2394–2397 (1992).

[69] Operation manual, Radiometer Physics GmbH, Meckenheim, Germany.

[70] Introduction to FT-IR Spectroscopy. Newport Corporation, Global Headquarters, 1791 Deere Avenue, Irvine CA 92606.

[71] Introduction to Fourier transform infrared spectrometry. Thermo Nicolet Corporation, 2001; WI, USA.

[72] Experimental Physics III, Course notes, Prof. Ian Appelbaum. Department of Physics, University of Maryland.

[73] Hecht, E. *Optics* (Addison Wesley, 2001).

[74] Oxford instruments, Tubney Woods, Abingdon, Oxfordshire, OX13 5QX, UK.

[75] IMEP-LAHC, Grenoble.

[76] Lukashenko, A. & Ustinov, A. V. Improved powder filters for qubit measurements. *Review Of Scientific Instruments* **79**, 014701 (2008).

[77] Kittel, C. *Introduction to solid state physics* (Wiley, 1986).

[78] Fuse, T., Kawano, Y., Suzuki, M., Aoyagi, Y. & Ishibashi, K. Coulomb peak shifts under terahertz-wave irradiation in carbon nanotube single-electron transistors. *Applied Physics Letters* **90** (2007).

[79] Pelling, S. *et al.* Point contact readout for a quantum dot terahertz sensor. *Applied Physics Letters* **93**, 073501 (2008).

[80] Tabe, M. *et al.* Single-electron transport through single dopants in a dopant-rich environment. *Phys. Rev. Lett.* **105**, 016803 (2010).

[81] Graaf, C., Caro, J., Radelaar, S., Lauer, V. & Heyers, K. Coulomb-blockade oscillations in the conductance of a silicon metal-oxide-semiconductor field-effect-transistor point contact. *Physical Review B* **44** (1991).

[82] Danilov, A. V., Golubev, D. S. & Kubatkin, S. E. Tunneling through a multigrain system: Deducing sample topology from nonlinear conductance. *Phys. Rev. B* **65**, 125312 (2002).

[83] FlexPDE simulation package from PDE solutions Inc.

[84] Pedrotti, S. & Pedrotti, L. *Introduction to Optics* (Prentice Hall, 1992).

[85] Fourier Transform Infrared Spectroscopy, C.C Homes, Brookhaven National Laboratory, Upton, NY 11973.

[86] Dyakonov, M. & Shur, M. Shallow water analogy for a ballistic field effect transistor: New mechanism of plasma wave generation by dc current. *Phys. Rev. Lett.* (1993).

[87] El Fatimy, A. *et al.* Resonant and voltage-tunable terahertz detection in InGaAsInP nanometer transistors. *Applied Physics Letters* **89**, 131926 (2006).

[88] Hashiba, H., Antonov, V., Kulik, L., Komiyama, S. & Stanley, C. Highly sensitive detector for submillimeter wavelength range. *Applied Physics Letters* **85**, 6036 (2004).

[89] Hashiba, H., Antonov, V., Kulik, L., Tzalenchuk, A. & S. Sensing individual terahertz photons. *Physics* (2010).

[90] Ikushima, K., Yoshimura, Y., Hasegawa, T. & S. Photon-counting microscopy of terahertz radiation. *Applied Physics* **88**, 152110–1–152110–3 (2006).

[91] Kawano, Y., Fuse, T., Toyokawa, S., Uchida, T. & Ishibashi, K. Terahertz photon-assisted tunneling in carbon nanotube quantum dots. *Journal of Applied Physics* **103**, 034307 (2008).

[92] Knap, W. *et al.* Nonresonant detection of terahertz radiation in field effect transistors. *Journal of Applied Physics* **91**, 9346 (2002).

[93] Lu, J.-Q. & Shur, M. S. Terahertz detection by high-electron-mobility transistor: Enhancement by drain bias. *Applied Physics Letters* **78**, 2587 (2001).

[94] Wang, Z., Komiyama, S., Ueda, T. & Nagai, N. A modified scheme of charge sensitive infrared phototransistor. *Applied Physics Letters* **95**, 022112 (2009).

[95] Fulton, T. A., Gammel, P. L., Bishop, D. J. & Dunkleberger, L. N. Observation of combined Josephson and charging effects in small tunnel junction circuits. *Physical review letters* **63**, 1307–1310 (1989).

[96] Kastner, M. The single electron transistor and artificial atoms. *Annalen der Physik* **9**, 885–894 (2000).

[97] Nakamura, Y., Chen, C. D. & Tsai, J. S. Quantitative analysis of Josephson-quasiparticle current in superconducting single-electron transistors. *Phys. Rev. B* **53**, 8234–8237 (1996).

[98] Dayton, J., Heinen, V., Stankiewicz, N. & Wallett, T. Submillimeter Bckward Wave Oscillators. *International Journal of Infrared and Millimeter Waves* (1987).

[99] Prevost, P. Memoire sur l'equilibre du feu. *Journal de Physique* (1791).

[100] Karasik, A., B.S. Sergeev. THz hot-electron photon counter. *Applied Superconductivity* **15** (2005).

[101] Olaya, D. *et al.* An ultrasensitive hot-electron bolometer for low-background smm applications. *SPIE* (2006).

[102] Averin, D. & Likharev, K. *In Mesoscopic Phenomena in Solids* (Elsevier, Amsterdam, 1991).

[103] IMPATT and Gunn Diodes. Www.radio-electronics.com/info/data/semicond/.

[104] Haviland, D., Harada, Y., Delsing, P., Chan, C. & Claeson, T. Observation of the Resonant Tunneling of Cooper Pairs. *Physical Review Letters* **73** (1994).

[105] Cassidy, M. C. *et al.* Single shot charge detection using a radio-frequency quantum point contact **91**, 222104 (2007).